University of Nottingham
UK | CHINA | MALAYSIA

Magnetic Induction Tomography using Vector Spherical Harmonic Magnetic Fields and Quantum Sensing

Thesis submitted to the University of Nottingham for the degree of **Doctor of Philosophy, September 2024.**

Nandhakishore Perarulalan

20200587

Supervised by

Dr. Mark Fromhold

Signature _____

Date _____ / _____ / _____

Abstract

The work explores the use of spherical harmonic magnetic vector fields in magnetic induction tomography, an eddy current based non-ionising imaging technique. It uses the spherical harmonic magnetic fields as primary excitor fields, creating orthogonal sensitivity matrices ensuring efficient and accurate image reconstruction using two different algorithms. The thesis further explores the phase of the eddy current induced secondary magnetic fields and seeks to use phase in image reconstruction. Lastly, the thesis seeks to measure the eddy current induced secondary magnetic fields from low conductivity materials using quantum sensors known as optically pumped magnetometers.

Contents

List of Figures

Magnetic Induction Tomography using Vector Spherical Harmonic Magnetic Fields and Quantum Sensing

Chapter 1

Magnetic Induction Tomography - History, Development, Current State, Applications and Future

1.1 Overview

This chapter presents an introduction to the thesis, and provides a brief description of what each chapter consists of, the research problem that it seeks to tackle and the goals of the chapter.

It explains the concepts of Magnetic Induction Tomography, its historical development, various methodologies by which it is accomplished, the current state of research in Magnetic Induction Tomography and its potential applications.

It also provides a brief introduction into spherical harmonic functions, their theoretical applications, the idea of orthogonality and how they can play a crucial role in inversion problems in general and Magnetic Induction Tomography in particular. It also talks about the idea of sensitivity matrices, how they can be derived from different mechanisms and how they are necessary in achieving the final required imaging results. Inversion theory, how inversion problems are formulated, multiple different algorithms that are used to solve it, form the basis of the next part of the chapter.

Finally, the chapter presents the concept of quantum sensing, how it was conceived, executed and implemented, the state of development in quantum sensing and how it becomes relevant to magnetometry and Magnetic Induction Tomography. The multiple methods by which quantum sensing is implemented are discussed, with a particular focus on optically pumped magnetometry.

The chapter concludes by presenting the current state of research and development present in all these fields, and how they can be integrated together, and how advances in quantum sensing and inversion theory can benefit Magnetic Induction Tomography.

1.2 Introduction

This thesis is set out in five different chapters. The first chapter presents the current state of the method of Magnetic Induction Tomography, how it was conceived and developed, various

physical implementations of Magnetic Induction Tomography, use of different physical components like excitors and sensors, the use of sensitivity matrices and how the final image is obtained through reconstruction. It further expands into the literature and theory on spherical harmonic functions, orthogonality and its various applications and how it pertains to Magnetic Induction Tomography and inversion problems. Various algorithms and methodologies for solving inverse problems are also presented. The first chapter further elaborates the theory and development behind quantum sensors and optically pumped magnetometers, their use in measuring low magnetic fields and their application in Magnetic Induction Tomography.

The second chapter further develops the idea of orthogonality, how orthogonal matrices can be constructed using orthogonal polynomials and how the concept of orthogonality becomes crucial in solving inversion problems. It elaborates the idea of spherical harmonic functions, how they can be physically realized using magnetic fields and how they can prove to be a good choice for excitor based primary magnetic fields. The experimental implementation of spherical harmonic magnetic fields is described in detail. The chapter further elaborates how the experimentally obtained data using spherical harmonic magnetic fields are used in image reconstruction and mapping the distribution of electrical conductivity. It discusses the use of two different algorithms in order to arrive at the final reconstructed images.

The third chapter entails the computational simulations and calculations made in order to derive the magnitude and the phase of the secondary magnetic fields generated by eddy currents. It explains in detail the procedures followed to implement numerical simulations, the idea of material properties, meshing, boundary conditions utilized and how the results are finally arrived at. Chapter 3 further draws a comparison between computational and experimental results of phase of secondary magnetic fields. The last part of the chapter deals with the use of phase in image reconstruction using the idea of Radon transforms.

The fourth chapter deals with the use of quantum sensors and how optically pumped magnetometers are used in the low conductivity range ($0 - 1$ Sm^{-1}) to measure ultra low secondary magnetic fields that are generated from insulators. The chapter delves into how low conductivity saline solution samples are created as phantoms for insulators, how the experiment is set up within a magnetic shield, the design and implementation of excitor based primary magnetic fields and cancelling fields, and the use of optically pumped magnetometers to measure the secondary fields. It presents the relationship between the electrical conductivity of low conductivity magnetic insulators and eddy current based secondary magnetic fields, and talks about how quantum sensing could be further exploited to sense other lower conductivity materials.

The final chapter concludes by presenting the developments and observations reported here extend upon the previous literature and the state of the field. It also suggests how future enhancements are possible to improve the techniques and results used within this work. This thesis uses SI units as its unit system for its equations and calculations.

1.3 Magnetic Induction Tomography

Figure 1.1 depicts a fundamental model of Magnetic Induction Tomography (MIT). Magnetic Induction Tomography is accomplished by generating eddy currents within the region of interest that is sought to be imaged. The key components within a Magnetic Induction Tomography system include excitor or transmitter based magnetic field sources, the object or the region to be imaged or examined and the receiver or the magnetometer that records the induced or

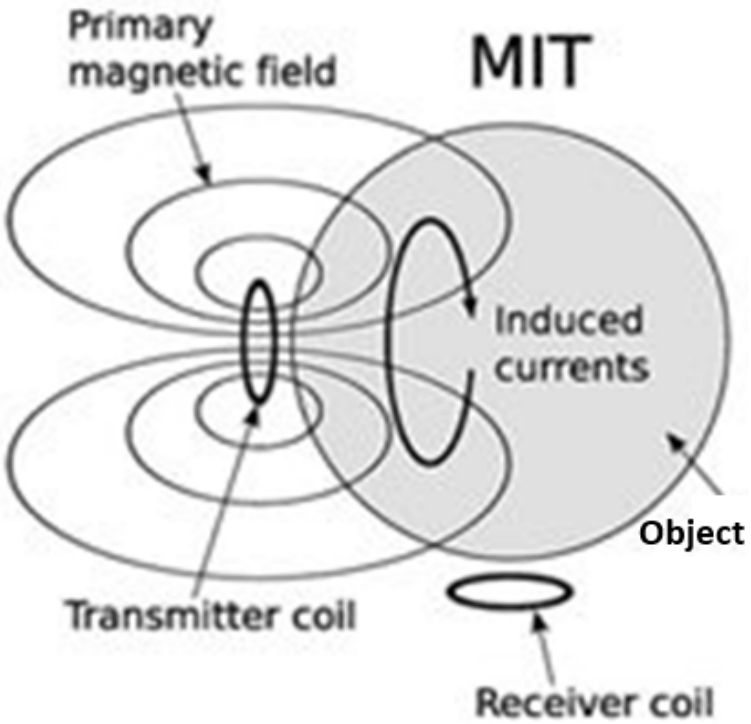

Figure 1.1: Basic Model of Magnetic Induction Tomography

secondary magnetic fields. A primary magnetic field is generated by using a magnetic field source, depicted by transmitter coils within the figure. The primary magnetic field in turn induces eddy currents within the region. The induced eddy currents generate a secondary magnetic field which is measured as an output signal by the receivers. The measured signals are indicative of the electromagnetic properties of the system being imaged or measured.

Theory

Magnetic Induction Tomography, also known as Eddy Current Tomography and Electromagnetic Induction Tomography, is an eddy current based imaging method based on Faraday's law of electromagnetic induction. Faraday's law states that there is an induced electric field and an electric current whenever there is a change in the magnetic field in a conductor. The induced electromotive force (emf), ϵ, is directly proportional to the rate of change of magnetic flux, ϕ passing through the conductor.

$$\epsilon = -N(\frac{d\Phi}{dt}) \tag{1.1}$$

where N is the number of loops in the conducting circuit. The induced electric current in turn generates a magnetic field that opposes the magnetic field that causes it.

$$\nabla \times \vec{E} = -(\frac{\partial \vec{B}}{\partial t}) \tag{1.2}$$

The induced current within the conductor swirls in loops or eddies upon the surface and is hence known as an eddy current. Equations (1.1) and (1.2) use SI units.

Tomography is the imaging method by which a section or a slice of the region of interest under examination is imaged by using a penetrating waveform like electromagnetic waves like

X- Rays. Magnetic Induction Tomography seeks to utilize this phenomenon of electromagnetic induction defined by Faraday's law to image and characterize the materials present within the region of interest to be imaged.

Forward Problem

Magnetic Induction Tomography is generally accomplished in two phases - i) Forward Problem and ii) Inverse Problem. The forward problem involves generating primary magnetic fields, calculating the strength of the eddy currents and the secondary magnetic fields caused by them. The secondary magnetic fields are then used to obtain magnetic vector potentials and formulate the sensitivity matrix required to calculate the physical and electromagnetic parameters of the region of interest to be imaged.

Inverse Problem

Inverse theory is a broader mathematical area with multiple applications, one part of which is used in Magnetic Induction Tomography and other forms of tomographic reconstruction. The goal of inverse theory is that from partially known resultant observations or variables, the inverse formulation seeks to obtain the causative agents. Generally, when a function f operates upon a variable x, the output y is given by

$$y = f(x) \tag{1.3}$$

The idea of inverse theory or inversion problems is to calculate x considering y is known or observed.

$$x = f^{-1}(y) \tag{1.4}$$

Within the context of Magnetic Induction Tomography, inverse theory is used to reconstruct images from observed secondary magnetic fields generated from eddy currents. The reconstructed images could correspond to the electromagnetic properties of the system and the region of interest, like electrical conductivity (σ), relative permeability (μ_r) or dielectric constant (ϵ_r). These properties help to image the system and characterize it, and the image reconstruction could happen through the same algorithms that are used to solve inverse problems elsewhere.

Features of Magnetic Induction Tomography

Magnetic Induction Tomography is a non-invasive imaging method without the use of electromagnetic radiation waves like X- Rays. Hence, it has the potential to penetrate through materials like lead, which normally cannot be imaged using X Rays, or CT (Computerized Tomography) scans. It is also a room temperature based technique that doesn't require a complicated cryogenic cooling setup similar to MRI (Magnetic Resonance Imaging) and NMR spectroscopy. It is an economic method with no risk of radiation exposure, hence it has no dangers associated with biosafety.

The Specific Absorption Rate (SAR), that is a measure of the amount of energy absorbed by biological material like human tissue, is dependent on multiple factors like the strength of the electromagnetic field that it is exposed to, the frequency of the RF (radiofrequency) wave that is incident upon it and its inherent electromagnetic properties. In Magnetic Induction Tomography (MIT), the excitor magnetic fields used are not as high as the B_0 field used in MRI (Magnetic Resonance Imaging), which are usually on the order of 1.5 T. It is possible

to perform MIT at a low frequency of 0 - 100 kHz, as opposed to MRI which uses RF waves in the MHz range. Thus the Specific Absorption Rate (SAR) measures of Magnetic Induction Tomography (MIT) remain very manageable, in comparison with MRI Imaging.

Two components of the secondary magnetic field are primarily considered - i) the magnitude and ii) the phase of the magnetic field. Both of these components directly correspond to the physical parameters of the system and, hence, both of them can be used in reconstruction of images within the region of interest. Depending upon the component being observed and acquired for data, Magnetic Induction Tomography has been used in multiple and varying different applications.

Both two dimensional and three dimensional image based reconstructions are possible depending upon the way experimental data is gathered and the sensitivity matrices are formulated and constructed. Efficient reconstructions are able to reconstruct a larger area with a better quality using less observed data.

1.3.1 Conception, History and Development

Eary History

While eddy currents had been a well established theoretical phenomenon, one of the earliest theoretical formulations of Magnetic Induction Tomography and the idea of using it in imaging was established by Griffiths [1]. The idea of electromagnetic imaging has been outlined by a few other works including A- Zeibak et al. [2]. Griffiths outlines the idea of using eddy current based imaging and how it has potential applications in biomedical tissue imaging and industrial tomography in his work. It also outlines how the permittivity and the conductivity of the sample get encoded within the magnitude and phase responses of eddy current based secondary magnetic fields.

An early experimental realization of Magnetic Induction Tomography comes from Korjenevsky et al. [3], where inductor coils are used as both primary field excitors and detectors. The region of interest is set up as a circle using 16 different electromagnetic coils, all of which act as excitor primary coils and receiver based secondary coils.The system is operated at a frequency of 20 MHz. The voltage from the secondary coils is directly proportional to the secondary eddy current fields and the phase in this MIT system is determined by the frequency of operation.

Another experimental realization of phase based Magnetic Induction Tomography and a way to measure phases was implemented in Gough [4]. It was a single channel, coil based, Magnetic Induction Tomography system with a special provision and electronics to accurately measure the phase changes in secondary magnetic fields.

Sensor and Hardware Development

There are multiple types of coils with potential usage in Magnetic Induction Tomography - i) air core sensors and ii) ferrite core sensors to measure the secondary magnetic field [5]. Multiple design methodologies are possible when it comes to pickup coil design, like Rogowski coils, gradiometer sensors, planar coil sensors and spherical, mutually perpendicular sensors that are designed to do multiaxial measurements. Zero flow coil sensors are also used in Magnetic Induction Tomography. Primary coils are often designed in a way to ensure their magnetic fields

don't interfere with the operation of pickup coils and their field strength doesn't get picked up by the receiver. Differential pickup coils that are used to determine just the difference in the field have also been increasingly used in Magnetic Induction Tomography.

Multifrequency Systems

Single frequency based Magnetic Induction Tomography systems have now led to multi frequency systems, where the excitation frequencies with which the eddy currents are generated spans a larger range. Multi frequency measurements are utilized by Scharfetter et al. [6] , in Magnetic Induction Tomography using planar gradiometers. Measurements are made from a range of frequencies from 50 kHz to 1 MHz.The idea of multi frequency based Magnetic Induction Tomography slowly morphs into Magnetic Induction Spectroscopy [7] with the frequencies ranging from 10^2 kHz to 10^4 kHz. Soleimani [8] uses a frequency range of 10 kHz to 100 kHz to characterize materials.

1.3.2 Current State

Sensor Development

The present state of Magnetic Induction Tomography is that the sensors have moved from pickup coils to Hall effect sensors [9] and fluxmeters and fluxgate magnetometers. This helps in increasing the sensitivity and reducing the lowest measurable magnetic field from the range of $0.1-1\ mT$ to $0.1-1\ \mu T$. Receiver array designs try to optimize the signal to noise ratio of the receiver coils that include planar array designs [10] and a continuous optimization of receiver designs [11].

Mathematical Modelling

The mathematical way in which Magnetic Induction Tomography is being modelled has changed over the years. Griffiths modelled the excitor coil simply as a magnetic dipole and used magnetic vector potential Taylor series approximations as a way towards calculating the phase difference between the primary and secondary magnetic fields. With changing geometric structures and complex transmitter and receiver patterns, Finite Element Method [12] and other numerical algorithms [13] are used as a way to model the system. A lumped parameter model [14] is also developed by Jeon et al. Quasistatic and magneto-quasi-stationary approximations of eddy current modelling are used to arrive at eddy current distributions within the region of interest. The monotonicity principle [15] has been used to model the inverse problem within Magnetic Induction Tomography in some approaches.

Phase Based Modelling

Phase [16] as a physical parameter to measure the electromagnetic properties like permittivity and conductivity has also been established with MIT theory. Multi phase systems with multiple transceiver coils are used as a way to distinguish between two different electrical conductivities. Phase based reconstruction is also possible in imaging biomedical systems like tissues. Some other electromagnetic properties that are also looked into include permeability imaging [7].

Forward and Inverse Modelling

There are multiple ways of undertaking the forward modelling and inverse modelling within Magnetic Induction Tomography. Historical approaches have included trying to solve inverse problems with algorithms, but more recent approaches follow the pattern of breaking down the

larger non-linear, inverse problems into multiple subroutines [17] that are solved using linear algorithms. Forward problem modelling done using the Finite Element Method paved the way for sensitivity matrices to be formulated along Edge and Volume Finite Element Methods [18] [19] [20] [21].

Exploration of Quantum Sensing in Magnetic Induction Tomography

The most recent developments and advances in Magnetic Induction Tomography have been the exploration and use of quantum sensing in order to measure extremely low secondary magnetic fields. Magnetic Induction Tomography using a rubidium based optically pumped magnetometer was first accomplished by Wickenbrock et al. [22]. Electromagnetic Induction Imaging using atomic magnetometers was accomplished by Deans et al. [23], in which they accomplished a phase based imaging of copper, aluminium and vanadium samples with potential applications in non-destructive evaluation.

Jensen et al. presented a Magnetic Induction Tomography image of an animal heart using an optically pumped magnetometer [24]. Bevington developed an experimental method to detect material and structural defects in non-destructive testing using atomic magnetometers [25]. Deans et al. developed a way to use Radio Frequency (RF) atomic magnetometers to do through barrier imaging where a metallic barrier conceals the objects and the region of interest to be imaged [26].

Unshielded atomic magnetometer operation is required to ensure that atomic magnetometers or optically pumped magnetometers can be functional in multiple use cases within Magnetic Induction Tomography. Rushton et al. devised a mechanism with which optically pumped magnetometers can be used in a magnetically unshielded environment within Magnetic Induction Tomography [27]. Quantum entanglement enabled Magnetic Induction Tomography has been accomplished by Zheng et al. [28].

1.3.3 Applications

Magnetic Induction Tomography has an immense number of potential applications in biomedical imaging, non-destructive testing and evaluation, geophysical measurements, fluid flow testing, food quality testing and potential eddy current measurements.

Biomedical Applications

One of the primary applications of Magnetic Induction Tomography is in biomedical imaging. Given its non-invasive, non-ionising nature, it remains an efficient choice for imaging physiological and medical applications for diagnosis. It has been used as a supplementary method for brain imaging, cardiography and lung imaging. It has been used along with magnetoacousto tomography (MAT-MI) for breast tumour detection and imaging by Zhou et al. [29].

A multifrequency system has been used for intracranial hemorrhage detection by Xiao et al. [30]. Internal hemorrhagic stroke has also been imaged using Magnetic Induction Tomography by Chen et al. [31]. The imaging modality is used for imaging cerebral stroke in a method developed by Zolgharni [32]. An algorithm is proposed by Zhang et al. [33] to continuously monitor brain injury based on Magnetic Induction Tomography. Imaging of the heart using optically pumped magnetometer based Magnetic Induction Tomography has been achieved by Jensen et al. [24]. Optical Magnetic Induction Tomography was achieved by Marmugi and

Renzoni [34] to detect atrial fibrillation. The feasibility of lung based imaging was studied by Scharfetter et al. [35]. Imaging of lung structure is also acieved by Wang et al. using holographic Magnetic Induction Tomography [36].

Biomedical tissue imaging is also made possible through three dimensional Magnetic Induction Tomography, trying to image human thorax and lung density of tissues. Multiple channel systems have been developed by Scharfetter to sense and image biological tissues.

Industrial Applications

Non-destructive testing and evaluation and imaging of structural and material defects is yet another significant application of Magnetic Induction Tomography. Whenever there is a crack or a defect within a test piece, induced eddy currents vary in magnitude along the surface of the test piece. That, in turn, changes the phase of the secondary eddy current based magnetic fields, which, in turn, could be used as a method to characterize the defects.

Industrial process tomography, is illustrated by Ma and Scharfetter, for an example, as a potential industrial application of Magnetic Induction Tomography [37]. Soleimani [7] uses the idea of magnetic induction spectroscopy to characterize structural and functional defects in metallic materials. He also develops an industrial process tomography based system for the purposes of industrial imaging. Monitoring structural defect formations and displacements in steel manufacturing is yet another application of Magnetic Induction Tomography developed by Soleimani et al. [38] [39]. Magnetic Induction Tomography also find potential applications in security scanning.

Bevington et al. devised a way to detect structural defects using alkali-metal spin masers to detect low magnetic fields. They also developed an imaging or spectroscopy method to detect concealed defects using atomic magnetometers. Dorn et al. apply the idea of Magnetic Induction Tomography to scanning 3D cargo containers and boxes [40].

Geophysics Applications

Magnetic Induction Tomography also has geomagnetism based applications with potential uses in mining where mapping electrical conductivity becomes crucial and potential monitoring of oil and gas. Geoarcheological mapping using electromagnetic induction tomography has been accomplished by Christiansen et al. [41]. A multifrequency Magnetic Induction Tomography was developed by Tang et al., in order to measure the electrical conductivity and magnetic susceptibility of two different heritage sites with varying earth surfaces and conditions.

Fluid Flow Based Applications

Magnetic Induction Tomography is also used to monitor fluid flow based applications where two immiscible fluids need to be separated out. Since the two fluids have different electromagnetic properties like conductivity, it becomes possible to use Magnetic Induction Tomography for this application. As a part of fluid flow monitoring, within industrial applications of Magnetic Industrial Tomography, Ma et al. [42] designed a system with a conductivity contrast of 0.06 Sm^{-1} with 16 coils. They also combined MIT with electromagnetic velocity tomography to map and characterize continuous multiphase flows of water. Sieger et al. [43] applied Magnetic Induction Tomography over the liquid metal alloy $GaInSn$.

Food Processing Based Applications

Apart from conventional applications like medical diagnosis and non-destructive evaluation, Magnetic Induction Tomography could also be potentially used in food quality monitoring or space waste disposal. It is possible to inspect the quality of food materials like meat and agricultural produce based on electrical conductivity, as the presence or absence of moisture changes the electrical conductivity accordingly and also affects the quality of the material.

O'Toole et al. presented a theoretical framework for conductivity measurements of food samples [44]. Tang et al. had measured the electrical conductivity of potato and pork loin before and after freezing, using it as a frozen-thaw sample [45]. Barai et al. used the idea of bioimpedance spectroscopy to measure the electrical conductivity of a range of agricultural produce like potatoes, tomatoes, bananas and cucumbers [46].

Space Based Applications

Magnetic Induction Tomography has a potential to be used in space based applications, where eddy currents are proposed as a way to remove space based debris from the orbital path of launch satellites and payloads. Since eddy currents could be used a positioning mechanism, it is likely that Magnetic Induction Tomography could be used to detect and characterize debris so that it could be averted and repositioned.

Gomez et al. designed a method by which eddy currents could be applied for de-tumbling of space debris [47]. Sharma et al. [48] also present a mechanism by which eddy currents could be used to remove space debris of size $1 - 10\ cm$.

1.4 Spherical Harmonics

1.4.1 Theory

Spherical harmonics are functions that are solutions to the Laplace's equation.

$$\nabla^2 \psi = 0 \tag{1.5}$$

They are defined on the surface of a sphere and can be used as an orthogonal basis set to define and expand mathematical functions upon the surface of a sphere.

The spherical harmonic functions are defined by

$$Y_l^m(\theta, \phi) = e^{im\phi} P_l^m(\cos(\theta)) \tag{1.6}$$

where θ and ϕ are co-ordinate angles (radial and axial) on a spherical co-ordinate system, m and l are radial and axial indices and P_l^m are the corresponding associated Legendre polynomials.

Any function upon the surface of a sphere can be expanded in terms of individual spherical harmonic functions, by finding out the corresponding Fourier coefficient which can be calculated as follows. If the function is given by $f(\theta, \phi)$, then corresponding Fourier coefficient for the spherical harmonic is calculated by

$$\hat{f_l^m} = \int_0^{\pi} \int_0^{2\pi} f(\theta, \phi) Y_l^m(\theta, \phi) d\theta d\phi \tag{1.7}$$

Once the Fourier coefficients are calculated, the function $f(\theta, \phi)$ can be expanded out as follows

$$f(\theta, \phi) = \sum_{l=0}^{\infty} \sum_{m=-l}^{l} \hat{f_l^m} Y_l^m \tag{1.8}$$

The general formulation of spherical harmonics has been used. Spherical harmonics could either be scalar spherical harmonics or vector spherical harmonics.

1.4.2 Mathematical Properties of Spherical Harmonics

Spherical harmonics form a part of Lie group $SO(3)$, where every element of the subset forms part of the special orthogonal set. If e_i and e_j are considered two elements amongst spherical harmonics, then the idea of orthogonality is given by

$$\langle e_i, e_j \rangle = \begin{cases} 1, & i = j \\ 0, & i \neq j \end{cases} \tag{1.9}$$

This idea of orthogonality is crucial when it comes to their application in solving inverse problems.

Uniqueness

Uniqueness, from the perspective of inversion problems, is a very significant property. It ensures that the solutions obtained as part of the problem remain unique and are able to draw out different solutions for the provided inversion problem. An inversion problem is typically ill-posed, and it needs to be solved using unique solutions in order to arrive at multiple different solutions. Baratchart et al. [49] identify a way to use spherical harmonics to obtain unique solutions in ill-posed inverse problems in geomagnetism by restricting the subspace of piecewise constant vector fields. Clerc et al. [50] use spherical harmonics to solve an inverse problem within electroencephalography (EEG) using spherical harmonics. Kono [51] uses spherical harmonics to address uniqueness problems in analysis of geomagnetic field direction data.

Orthogonality

Orthogonality is yet another key property of spherical harmonics that is vital when it comes to solving inverse problems. In Magnetic Induction Tomography, inversion problems play a crucial role in obtaining the final reconstruction. Every spherical harmonic function could be used to construct an orthogonal matrix that could efficiently make ill-posed problems well posed and improve upon the condition numbers of the sensitivity matrices. The spherical harmonics could be spread out over two or three dimensions in order to develop orthogonal matrices. An orthogonal matrix is a matrix whose inverse equals its transpose. If S is a matrix, then

$$S^{-1} = S^T \tag{1.10}$$

Such matrices can be generated using the spherical harmonic functions and can be physically implemented to solve inversion problems. Orthogonality and linear independence become important properties when it comes to solving matrix inversion based systems. The use of orthogonal spherical harmonics not only helps makes inversion easy, but also reduces cross talk and interference caused in observations within inverse problems.

Mcleod expands on the idea of orthogonality of spherical harmonic coefficients [52]. Lowes et al. have applied the idea of orthogonality of harmonic vector fields to expand geodesic fields [53]. It can be seen through such literature that orthogonality would be a key property in applying the idea of spherical harmonics into inversion problems.

1.4.3 Applications

Spherical harmonics are used in many branches of applied mathematics like electrostatics, geophysics and geomagnetism, surface parameterization, computer graphics, image compression and cosmology and atomic structures.

Electromagnetic Applications

Spherical harmonics are used by Dlugosz et al. [54]. to study the electrostatic properties of biomolecules. They are also used in the multipole field expansion in antenna and wave theory. Antennae radiation patterns are modelled using scalar spherical harmonics by Rahola et al. [55].

Geophysics and Geomagnetic Applications

Whaler performed a spherical harmonic based expansion of the geomagnetic field, as a linear inverse problem [56]. Muir develops a method of spherical harmonic analysis in the geosciences via hierarchical Bayesian inference [57]. In geophysics, multiple vector fields are statistically analyzed by Tang et al., using spherical harmonic expansion.

Imaging and Microscopy Applications

Spherical harmonic magnetic fields and corresponding coil structures are designed by Romeo and Hoult for use in Magnetic Resonance Imaging (MRI) [58]. Iivanainen et al. used a vector spherical harmonic based magnetic field calculation to position optically pumped magnetometers within a magnetic field to ensure magnetic fields are minimal [59]. Just like how Zernike polynomials are used in phase contrast microscopy, spherical harmonics are used in segmentation in confocal light microscopy by Eck et al. [60]. They are also used modelling three dimensional morphological structures in evolutionary biology by Shen et al. [61], and used in biological texture extraction for biological objects by Schaeben et al. [62].

Computer Graphics

Nortje et al. uses spherical harmonics for surface parameterization and mesh refinement within computer graphics [63]. The Gibbs phenomenon in signal processing is resolved and expanded using spherical harmonics by Gelb [64]. Spherical harmonic gradients are used for mid range illumination in computer graphics by Annen et al. [65]. In other forms of graphic visualization, a model to represent skylight better in terms of spherical harmonic expansion is presented by Habel et al. [66]. An interactive refraction on complex manifold like geometries using ray tracing is also developed using spherical harmonic functions by Genevaux et al. [67]. A spherical harmonic expansion of Bidirectional Reflectance Distributive Function (BRDF) in low frequency lighting is presented by Kautz et al. [68].

Astronomy and Cosmology Applications

A spherical harmonic based analysis is done by Drake et al. using the HEALPix (Hierarchical Equal Area isoLatitude Pixelation) scheme used in Cosmic Microwave Background (CMB)

radiation [69]. Rambaux et al. use spherical harmonic decomposition for analysing geometric shapes of Saturnian inner moons [70].

Atomic and Electronic Structure

One of the most well known applications of spherical harmonic functions is that they are solutions of Schrodinger's equations providing the electron configuration of the hydrogen atom. Morris et al. use spherical harmonic coefficients for protein binding and ligand comparisons [71]. Pinchon et al. use real spherical harmonics as a way to model rotations of atomic orbitals [72].

Thus, spherical harmonic functions are used in terms of expansion, decomposition and modelling within multiple fields of applied mathematics.

Within Magnetic Induction Tomography, excitor magnetic fields could be potentially modelled using spherical harmonic functions, which are capable of providing unique solutions as part of their inversion problem and orthogonal and linearly independent sensitive matrices with low condition numbers.

1.5 Sensitivity Matrices

1.5.1 Theory

A sensitivity matrix is used to determine the state of the system. In many cases, it is given by the Jacobian of the system. If a function $u(x_1, x_2, x_3)$ is dependent on variables like x_1, x_2, x_3, then the Jacobian of the system is given by

$$\mathbf{J_F} = \begin{bmatrix} \frac{\partial u_1}{\partial x_1} & \frac{\partial u_1}{\partial x_2} & \frac{\partial u_1}{\partial x_3} \\ \frac{\partial u_2}{\partial x_1} & \frac{\partial u_2}{\partial x_2} & \frac{\partial u_2}{\partial x_3} \\ \frac{\partial u_3}{\partial x_1} & \frac{\partial u_3}{\partial x_2} & \frac{\partial u_3}{\partial x_3} \end{bmatrix} \tag{1.11}$$

Within Magnetic Induction Tomography theory, the electromagnetic properties like electrical conductivity σ, relative permeability μ_r and dielectric constant ϵ_r are determined by solving an inverse problem. The sensitivity matrix is the one that needs to be inverted in order to arrive at the final reconstructed image. If S is the sensitivity matrix and B_e is the observed magnetic fields acquired as data, then the final reconstructed image is given by

$$\sigma = S^{-1} \cdot \vec{B_e} \tag{1.12}$$

1.5.2 Sensitivity Formulations

Sensitivity of a system can be formulated and calculated in many ways. It could be done potentially using electric fields, magnetic vector potentials, magnetic fields found in primary and secondary parts of Magnetic Induction Tomography. It is calculated either directly analytically within a continuous domain or numerically within a discretized domain using computational methods like the Finite Element Method (FEM) or the Finite Difference Method (FDM).

An early formulation of sensitivity in Magnetic Induction Tomography was done by Griffiths et al., where it is defined as a change in magnetic field orthogonal to the secondary receiver to the original magnetic field. Rosell et al. [73] defines sensitivity as a function of the detected voltage change in the secondary receiver circuit and the primary injected current. It is further defined as based on the products of the electric fields in the primary excitor and the secondary sensors. If $\vec{E_1}$ is the primary electric field, $\vec{E_2}$ is the secondary electric field, ν is the frequency of the system, I_1 is the primary excitor current and I_2 is the secondary receiver current, then the sensitivity S is given by

$$S = \frac{\nu}{I_1 I_2} \vec{E_1} \cdot \vec{E_2} \tag{1.13}$$

Ma. et al. [7] define sensitivity based on the terms of permeability of the region of interest. The formulation also differs based upon the fact that it is done based upon the magnetic field, unlike the electric field.

$$S = \frac{\partial V_{12}}{\partial \mu} = -\frac{i\omega}{I_1 I_2} \int \vec{H_1} \cdot \vec{H_2} d\Omega \tag{1.14}$$

where S is the sensitivity, V_{12} is the surface voltage on the region of interest, H_1 is the primary magnetic field, H_2 is the secondary magnetic field, I_1 is the primary excitor current and I_2 is the secondary receiver current.

The sensitivity can also be defined based upon the dot product of magnetic fields with the help of a constant that is used to describe the geometry of the system. If S is the sensitivity, then k is the geometric constant, $\vec{B_1}$ is the primary magnetic field and $\vec{B_2}$ is the secondary magnetic field [74] [75].

$$S = k\vec{B_1} \cdot \vec{B_2} \tag{1.15}$$

The Finite Element Method is used to calculate the sensitivity matrix of Magnetic Induction Tomography in some cases. Wei et al. use magnetic vector potentials to determine the sensitivity matrix of the system. The sensitivity of the system, as formulated by them, is given by

$$S = \frac{\partial V_{12}}{\partial \sigma} = -\frac{\omega^2}{I_1 I_2} \int \vec{A_1} \vec{A_2} d\Omega \tag{1.16}$$

where $\vec{A_1}$ is the primary magnetic vector potential, $\vec{A_2}$ is the secondary magnetic vector potential, I_1 is the primary excitor current, I_2 is the secondary receiver current and ω is the frequency of the system.

Sensitivity Formulation based on Magnetic Vector Potential from Maxwell's Equations

A magnetic vector potential based approach has been used in this thesis to formulate the sensitivity matrix of the Magnetic Induction Tomography based system. Maxwell's equations are used to model the eddy currents within the system and the sensitivity of the system. The fourth Maxwell's equation given by Ampere's law states that

$$\nabla \times \vec{H} = \vec{J} + \frac{\partial \vec{D}}{\partial t} \tag{1.17}$$

where H is the magnetic field, J is the total electric current density present within the system and D is the electric displacement field. According to Faraday's law, from Equation 1.2

$$\nabla \times \vec{E} = -(\frac{\partial \vec{B}}{\partial t})$$

where E is the magnetic field and B is the magnetic flux density. It can be said that

$$\vec{B} = \nabla \times \vec{A} \tag{1.18}$$

and

$$\vec{B} = \mu \vec{H}$$
$$\vec{D} = \epsilon \vec{E}$$

where $\vec{A}$ is the magnetic vector potential, μ is the permeability within the system and ϵ is the permittivity of the system. The electric field $\vec{E}$ is given by

$$\vec{E} = -j\omega \vec{A} \tag{1.19}$$

Now, the total current in the system is given by the sum of the primary current density used to generate excitor fields $\vec{J_0}$ and the generated eddy current density $\vec{J_e}$. The eddy current density J_e is given by [76]

$$\vec{J_e} = \sigma \vec{E} \tag{1.20}$$

where σ is the electrical conductivity of the material within the region of interest. Rearranging Equation 1.17, it is found that

$$\nabla \times \vec{H} = \vec{J_0} + \vec{J_e} + j\omega \vec{D} \tag{1.21}$$

Substituting 1.20 in 1.21,

$$\nabla \times \vec{H} = \vec{J_0} + \sigma \vec{E} + j\omega\epsilon \vec{E} \tag{1.22}$$

$$\nabla \times \vec{H} = \vec{J_0} + (\sigma + j\omega\epsilon)\vec{E} \tag{1.23}$$

Substituting 1.19 in 1.23

$$\nabla \times \vec{H} = \vec{J_0} + (\sigma + j\omega\epsilon)(-j\omega\vec{A})$$
$$\nabla \times \vec{H} = \vec{J_0} - j\omega\sigma\vec{A} + \omega^2\epsilon\vec{A}$$

The ϵ term can be ignored in the quasistatic approximation of eddy currents. Further evaluating, it can be seen that

$$\nabla \times \vec{H} + j\omega\sigma\vec{A} = \vec{J_0} \tag{1.24}$$

By substituting 1.18 in 1.24, the operational equation of the eddy current based Magnetic Induction Tomography system is derived as [7]

$$\nabla \times \frac{\nabla}{\mu} \times \vec{A} + j\omega\sigma\vec{A} = \vec{J_0} \tag{1.25}$$

The Finite Element Method can be used to split the domain and the region of interest where Magnetic Induction Tomography can be performed into multiple nodes. The magnetic vector potential at each node, within the elements of the domain, is given by [77]

$$\vec{A}(x, y, z) = N(x, y, z).\vec{A_e} \tag{1.26}$$

where $N(x, y, z)$ is the edge shape function used to discretize the domain at the point (x, y, z) and $\vec{A_e}$ is the magnetic vector potential solved from 1.26 at that specific point.

Now, the induced voltage in the sensing element is calculated using Maxwell's first law.

$$V = \int \vec{E}.dv \tag{1.27}$$

where dv is the element present within the domain. Substituting 1.19 in 1.27, the voltage measured in the sensing element can be found to be [77]

$$V = -j\omega \frac{\int \vec{A}.\vec{J}dv}{I_0} \tag{1.28}$$

Now, the sensitivity is defined as the rate of change of voltage sensed by the sensing element to the electrical conductivity present within the domain, as defined by the Jacobian matrix of the system, from 1.16. Differentiating 1.2 and 1.17 with respect to electrical conductivity σ and using vector identities, it can be seen that [78]

$$\nabla \times \frac{\partial \vec{E}}{\partial \sigma} = -j\omega\mu \frac{\partial \vec{H}}{\partial \sigma}$$

$$\nabla \times \frac{\partial \vec{H}}{\partial \sigma} = (\sigma + j\omega\epsilon) \frac{\partial \vec{H}}{\partial \sigma}$$

From which, the sensitivity is derived as

$$\frac{\partial \vec{H}}{\partial \sigma} = \int \vec{E} \cdot \vec{E} dv \tag{1.29}$$

Thus, the sensitivity of the domain can be calculated in a similar manner using magnetic vector potential as the induced secondary magnetic fields from the eddy currents are sensed in the form of voltages by the Hall probe. The sensitivity of the system in a coil setup consisting of n coils is given by

$$\frac{\partial V_{ij}}{\partial \sigma} = -\omega^2 \frac{\int \vec{A}_i \cdot \vec{A}_j dv}{I_0} \tag{1.30}$$

where V_{ij} is the voltage between the i^{th} coil and j^{th} coil, $\vec{A}_i$ and $\vec{A}_j$ are the magnetic vector potentials when coils indexed i and j are excited using the current I_0.

The same formulation can be adapted to suit a Hall probe based or a dual coil based Magnetic Induction Tomography system, resulting in 1.16, with $\vec{A}_1$ and $\vec{A}_2$ as magnetic vector potentials in the exciting and sensing elements of the Finite Element Model and I_1 and I_2 as the currents present within the excitation and sensing elements [79].

$$S = \frac{\partial V_{12}}{\partial \sigma} = -\frac{\omega^2}{I_1 I_2} \int \vec{A}_1 \vec{A}_2 d\Omega$$

This derivation of the sensitivity of the Magnetic Induction Tomography is adapted into multiple different formulation, in order to suit the system, depending upon the number of primary or excitor and sensing coils used, the type of sensors used, the meshing performed and the shape of the domains involved and other factors.

1.5.3 Algorithms

Broadly, there are also other methods by which the sensitivity of electromagnetic quantities like electrical conductivity, relative permeability and dielectric constant are calculated whenever there is a change in sources or observed perturbations. In order to calculate the sensitivity, Dyck et al. [79] use a derivative method with potential applications in optimisation and inverse problems. Mcgillivray et al. [78] use a boundary value problem solving method (split as two boundary value problems with different source terms and boundary conditions) to calculate the sensitivity of various electromagnetic parameters.

Multiple algorithms are developed in order to calculate the sensitivity matrix using the finite element method. Hollaus et al. use the reciprocity theorem and tetrahedral finite edge elements in order to develop the Jacobian matrix to describe the conductivity distribution of the surface based on the voltage on the secondary receivers [80]. Chen et al. propose a computationally efficient method to calculate the sensitivity matrix based upon the finite element method [76]. Yin et al. use a finite difference method to calculate the velocity effects of eddy currents in Magnetic Induction Tomography and formulate the sensitivity matrix based upon that [81].

1.6 Inversion Problems

1.6.1 Theory

Inverse problems are problems where the goal is to calculate the causes based upon the effects observed. Within the context of Magnetic Induction Tomography, it becomes the preferred approach for image reconstruction. The key challenge in solving inversion problems is finding a way to efficiently and perfectly reverse the relations that the causes have had upon the effects and observations. Mathematically, it translates to obtaining the perfect inverse of a causal matrix.

Within Magnetic Induction Tomography, the electromagnetic properties like electrical conductivity, relative permeability and relative permittivity are the ones that cause a change in the eddy current induced secondary magnetic fields. Hence, the chief goal of an inverse problem within Magnetic Induction Tomography is to invert the effects of these electromagnetic parameters upon the experimentally observed secondary magnetic fields. If σ is the electrical conductivity within the region of interest, B_e is the observed magnetic field and if S is the sensitivity matrix that describes the system, then the relationship is given by [82]

$$\sigma = S^{-1}B_e \tag{1.31}$$

The inverse problem is now solved by finding a way to invert the sensitivity matrix S. As can be seen from Section 1.5.2, there are multiple ways in which the sensitivity matrix is formulated. Multiple algorithms and methods have been used to invert matrices and solve the inverse problem. They have their own merits and demerits.

Inverting of a sensitivity matrix comes with its own challenges. In some cases, depending upon the geometry, the matrix is square. In a few other cases, the matrix is not uniform and has a size of $m \times n$, where m and n are not equal. Some inverse problems are linear, while non-linear inverse problems are subdivided into multiple linear problems to be solved.

In general, the main problem that confronts inverting a sensitivity matrix is that sensitivity matrices turn out to be ill-conditoned. Ill-posed matrices are linearly dependent, making inversion difficult and the corresponding senstivity matrices ill-conditioned. In an ill-conditioned matrix, the rank of the matrix is less than the size or dimension of the matrix. Non-invertible matrices also can turn out to be singular, without an inverse.

A matrix's invertibility and resistance to change and perturbations is determined by its condition number. The condition number of a matrix is defined by the ratio of the matrix's largest singular value to its smallest non-singular value, considering Euclidean norm. If S is the matrix, then the condition number κ is given by

$$\kappa = ||S|| \cdot ||S^{-1}|| \tag{1.32}$$

An ill-posed matrix in general has a high condition number. An invertible matrix in general has a low condition number, with the condition number of the identity matrix being 1.

1.6.2 Algorithms

Multiple algorithms have been used to invert ill-posed matrices with inversion theory forming a separate branch of mathematics. Some of the most commonly used algorithms and techniques are presented below.

Ill posed problems are determined by Fredholm integrals of the first kind.

$$\int_0^1 k(s,t)x(t)dt = y(s) \tag{1.33}$$

where $k(s,t)$ is the kernel to be inverted, $x(t)$ is the solution to be found and $y(s)$ is the observation found in the inverse problem. In matrix form, it becomes

$$Kx = y \tag{1.34}$$

where K is the ill conditioned matrix, x is the variable to be determined and y is the observation obtained.

Backprojection

The simplest method of trying to solve the inverse problem is to backproject the ill- conditioned matrix on to the set of observations. In matrix form, this means the inverse of the matrix is directly replaced by the transpose of the matrix. The equation

$$Kx = y \tag{1.35}$$

is solved by

$$x = K^{-1}y \tag{1.36}$$

In linear backprojection, K^{-1} is replaced by K^T, and hence the final solution becomes

$$x = K^T y \tag{1.37}$$

Regularization

The idea of regularization is to convert the ill-posed Fredholm integral to a well-posed Fredholm equation. In matrix form, the idea of regularization is to replace an ill-conditioned matrix arising out of an ill-posed problem with an approximate well posed matrix. In matrix form, if the goal is to find K^{-1} which is difficult to compute, K is to be replaced with an approximate well conditioned matrix. If K^* is the adjoint of K, then it can be said that,

$$K^*Kx = K^*y \tag{1.38}$$

Regularization is the process by which another matrix R is added to ensure the matrix becomes well conditioned, and x_α is an approximate solution to the ill conditioned problem.

$$(K^*K + R)x_\alpha = K^*y \tag{1.39}$$

Regularization is considered Tikhonov Regularization when the matrix $R = \alpha I$, where α is the regularization parameter and I is the identity matrix of the same dimensions.

$$(K^*K + \alpha I)x_\alpha = K^*y \tag{1.40}$$

Within Tikhonov Regularization, the final approximate solution is given by

$$x_\alpha = (K^*K + \alpha I)^{-1}K^*y \tag{1.41}$$

The adjoint of the matrix K^* is replaced by its transpose K^T, presenting the final solution.

$$x_\alpha = (K^TK + \alpha I)^{-1}K^Ty \tag{1.42}$$

The task of determining the required regularization parameter α is done by an optimization method, and the final solution arrived at is a least squares solution. Tikhonov Regularization is considered a penalized least squares method, considering that the parameter seeks to minimize the error between the original solution and the approximate solution.

There are many varied regularization techniques apart from Tikhnov Regularization that vary in how the regularization matrices are replaced and regularized. Regularization matrices include Dirichlet and Neumann boundary condition based matrices, First and Second Derivative based Tikhonov matrices and Truncated Singular Value Decomposition based matrices.

Iterative Regularization

The idea behind iterative regularization is that the regularization matrices are changed in every step according to the optimization procedure followed, and the final reconstruction on the inversion problem changes accordingly. There are several ways in which iterative algorithms are implemented. Landweber's iteration is a very common way of implementing the idea of iterative regularization. It includes several methods like Algebraic Reconstruction Technique (ART), Simultaneous Algebraic Reconstruction Technique (SART) and Simultaneous Iterative Reconstruction Technique (SIRT).

The Landweber iteration scheme is given by

$$x_{n+1} = x_n + \lambda_n K^T(y - Kx_n) \tag{1.43}$$

where the final solution gets updated sequentially in every step. Here, x_{n+1} is the required guess at every step, x_n is the initial step, λ_n is the relaxation parameter, y is the set of observations and K is the matrix to be inverted.

The algorithm can be modified in order to suit a few more parameters to help speed up the reconstruction and to arrive at the final output.

$$x_{n+1} = x_n + \lambda_n \frac{K^T(y - Kx_n)}{||K^2|| + a_n} \tag{1.44}$$

where $||K^2||$ is the Euclidean norm of the matrix to be inverted and a_n is the damping parameter.

There are other possible iterative schemes and methods like the Conjugate Gradient Method [83] that work with on the same principle as the Landweber iterative methods, with optimisation parameters being modified and the iteration steps varying.

Other methods

There are several other methods that could be used to solve specific subsets of inverse problems. There are Krylov methods used specifically for regularization and inversion of low rank matrices, Truncated Singular Value Decomposition Methods and inversion methods to solve non-linear matrices. Algebraic reconstruction techniques like the Radon transform which seek to reconstruct the image through projection data that is available could also be potentially used for inversion problems to arrive at the final result.

Some of the most recent advances in inversion theory includes the use of machine learning and deep learning algorithms [84] [85]. Deep learning and convolutional neural networks have begun to be employed to solve inverse problems with efficient results.

1.6.3 Applications

Medical Imaging

Given that inverse theory is a branch of mathematics, it has wide and varying applications. It could potentially be used in medical imaging and reconstruction applications like Magnetic Resonance Imaging (MRI) [86], Nuclear Magnetic Resonance Relaxometry (NMR), Computerized Tomography (CT) and Positron Emission Tomography (PET).

Geophysics

Inverse problems also find application in geological and geophysics techniques [87] where physical data is obtained about sub surface materials and it is used to draw inferences about the causal agents present beneath the surface of earth. Their use in geophysics has a wealth of applications in oil and gas mining and landmine detection.

Image Noise Removal

Inverse modelling is also actively employed in image denoising and deconvolution. The use of inverse problems as a way for noise removal [88] is well studied and documented. Thus, it also finds its way to potential signal processing applications. It is used in image deblurring in astronomy based applications. It is also used in instrument signal deconvolution.

1.6.4 Spherical Harmonics in Inverse Problems

While there are some ideas like the Helmholtz-Hodge theorem [89] [90] that could be applied to make inversion efficient, there is a lot of potential in the use of spherical harmonic functions in inversion problems. Within Magnetic Induction Tomography, the use of spherical harmonic functions as excitor functions has the potential to make inversion quick and efficient. The orthogonality property of spherical harmonic functions could be exploited to solve inversion problems more efficiently in general and within Magnetic Induction Tomography in particular.

1.7 Quantum Sensors

Recently, technologies have been developed to exploit the quantum properties of atomic and electronic systems such as entanglement and superposition. They find their potential applications in multiple domains such as quantum computing, quantum cryptography and networking, quantum imaging and quantum sensing.

The idea of quantum sensing is of immense interest in Magnetic Induction Tomography given its potential to measure highly sensitive magnetic fields. Its potential could be utilized in measuring materials that typically do not induce strong eddy current based secondary magnetic fields, given their insulator like properties.

Quantum sensing, also known as quantum metrology, is the detection and sensing of a physical quantity through its interaction with a quantum system [91]. The physical quantity could potentially be time, frequency, electric fields, magnetic fields, gravitational acceleration, velocity, force, voltage or temperature. The quantum system could potentially be based upon electron spin, nuclear spin, atomic spin, atom Rydberg states, supercurrents or photons [91]. The interaction with the physical quantity modifies the quantum state of the system and it is detected and measured based upon the modifications within the quantized energy levels of the system.

Quantum sensors are physically and experimentally realized through various platforms. Some of the most well known platforms include superconducting quantum interference devices known as SQUIDs, superconducting flux qubits, trapped ions, optically pumped atomic magnetometers, nitrogen vacancy centers in diamonds, optomechanical systems and interferometers [91].

Quantum sensors have an immense number of applications. They can be used in biomedical applications for diagnosis like in Magnetoencephalography (MEG) [92] and neuroscience to measure brain signals. They can be used to study the structure of single neurons and brain synapses. They are used in gravitational sensing in order to map the ground in archaeological and construction sites. They are used in exploration of minerals and oil and gas [93]. They could be employed in the defense industry for potential detection of submarines and radars. They are also used in communication networks and clocks to measure timing accurately. They are capable of playing a crucial role in position, navigation and timing based applications in geolocation and geopositioning systems.

Each quantum sensing platform offers its own advantages and disadvantages, and based upon the requirements and demands of the potential application, a mechanism to realize quantum sensing can be chosen.

1.7.1 Optically Pumped Magnetometry

Optically Pumped Magnetometry is a form of quantum sensing which works on the basis of the Zeeman effect. The Zeeman effect occurs when a magnetic field is incident upon an atomic sample and the splitting of spectral lines occurs.

The idea of optical pumping is that the atoms present within a particular sample or atomic vapor are increased to a particular energy level through external transfer of energy from a laser or a polarized light source. The optical pumping transfers energy and transitions atoms to a hyperfine state splitting of spectral lines. Generally, alkali metals like rubidium and caesium are used in optically pumped magnetometry, so that the single electron present in the valence shell could easily be made to change state and pumped to a higher energy level.

When the magnetic field to be sensed is incident upon the optically pumped atom cloud, Zeeman splitting occurs and is used to detect and measure the magnetic field. The optically pumped magnetometer consists of a pump and a probe laser. The pump laser is used to excite

the atoms up to a higher energy state and the probe laser is used as a way to measure the strength of the magnetic field through its intensity. Optically Pumped Magnetometers are capable of measuring very low magnetic fields, with very high sensitivity. The fields could be as low as 15 fT/$\sqrt{\text{Hz}}$.

Optically Pumped Magnetometers in Magnetic Induction Tomography

Optically Pumped Magnetometers will prove to be a great platform for Magnetic Induction Tomography because of its multiple advantages. They don't require a cryogenic cooling system like superconductor based platforms such as Superconducting Quantum Interference Devices (SQUIDS) or superconducting qubits. They are capable of operating within room temperature and the measurements can be made using conventional RF (Radio Frequency) electronics and FPGA (Field Programmable Gate Array) based platforms. They are also realizable in chip scale and hence can be used as part of multichannel systems with ease. The optically pumped magnetometer could also be used in a gradiometer configuration to sense out the magnetic field difference.

The eddy current induced secondary magnetic fields from low conductivity materials can be calculated and it reveals that optically pumped magnetometers are able to measure those corresponding secondary magnetic fields as part of Magnetic Induction Tomography. The measurement, imaging and characterization of low conductivity materials through Magnetic Induction Tomography can have many potential applications in non-destructive testing and evaluation, polymers and additive manufacturing and non-ionising biomedical imaging.

1.8 Conclusion

The chapter gives a brief introduction to the mathematical and experimental ideas applied and utilized in the thesis, and their historical development. The chapter provides the required theoretical basis for the thesis and the problems that it seeks to explore. Applications of the technique are enunciated and how they can be potentially applied in order to enhance and improve Magnetic Induction Tomography is also detailed. The theory and experimental methods are also expanded further in subsequent chapters.

Chapter 2

Magnetic Induction Tomography Using Vector Spherical Harmonic Magnetic Fields

2.1 Overview

The initial part of the chapter introduces the idea of orthogonality in matrices, expands into the construction and use of orthogonal matrices in linear algebra and inversion problems, outlines the idea of orthogonal polynomials and spherical harmonics and further talks about how orthogonality becomes an important component in solving inverse problems like Magnetic Induction Tomography.

The chapter later delineates the generation of spherical harmonic based magnetic vector fields and their use in Magnetic Induction Tomography. It describes the experimental setup required to generate these magnetic fields and presents how it can be used to solve inverse problems of Magnetic Induction Tomography using various different algorithms. The chapter is concluded with a discussion on the use of these different algorithms and potential expansion of looking into forms of other spherical harmonics.

2.2 Orthogonality

An orthogonal matrix is a square matrix whose inverse is equal to its transpose. If we consider S to be a matrix, then the requirement for orthogonality is

$$S^{-1} = S^T \tag{2.1}$$

It can also be seen from above that,

$$S \cdot S^T = I \tag{2.2}$$

$$S^T \cdot S = I \tag{2.3}$$

The rows and columns of an orthogonal matrix are linearly independent, which proves to be a key property in ensuring a matrix is invertible.

The ideas of linear independence and orthogonality are crucial when it comes to polynomial expansions and curve fitting. Orthogonal polynomials are often formed by using a generating function that operates within a specific, closed limits, interval and forms the basis set that

could be used to expand a polynomial function in terms of its constituent polynomials from the basis set. Multiple sets of orthogonal functions have been used as a basis to represent functions within a limited closed interval.

Two functions $f(x)$ and $g(x)$ are considered to be orthogonal if

$$\int f(x) \cdot g(x) dx = 0 \tag{2.4}$$

within the required interval.

For a vector basis that is orthogonal, the condition for orthogonality is presented as

$$\langle \vec{f}, \vec{g} \rangle = 0 \tag{2.5}$$

Fourier series expansion of multiple signals is done using a basis set of trigonometric functions of the sinusoidal function and cosine function with multiple frequencies. These functions form an orthogonal basis that are linearly independent and help in expanding out the function $f(x)$.

$$f(x) = c_0 + \sum_{n=0}^{N} (a_n(\cos(2\pi n x)) + b_n(\sin(2\pi n x))) \tag{2.6}$$

2.2.1 Orthogonal Polynomials

Orthogonal polynomials are a set of polynomials where each member of the set is found to be orthogonal to and to have its inner product to be zero with every other member of the set. They are generated using specific generating functions that are defined between the same intervals where the polynomials are orthogonal. Some of the most widely used orthogonal polynomials are classical orthogonal polynomials like Chebyshev polynomials, Jacobi polynomials, Laguerre polynomials, Hermite polynomials, Zernike polynomials and Legendre polynomials [94].

The aforementioned classes of polynomials are considered classical polynomials. There are also classes of discrete orthogonal polynomials and other classes of orthogonal polynomials that are generalized from classical polynomials. Classical orthogonal polynomials are often found to be solutions to differential equations and hence can be used as a way to solve and approximate solutions to differential equations.

Some of the generating functions for classes of orthogonal polynomials are found as follows

Chebyshev Polynomials

The generating function for Chebyshev polynomials, $T_n(z)$, is given by the contour integral

$$T_n(z) = \frac{1}{4\pi i} \oint \frac{(1-t^2)t^{(-n-1)}}{(1-2tz+t^2)} dt \tag{2.7}$$

Chebyshev polynomials remain orthogonal within the closed range of $[-1, 1]$. The first kind of Chebyshev polynomials is defined using

$$T_n(\cos\theta) = \cos(n\theta) \tag{2.8}$$

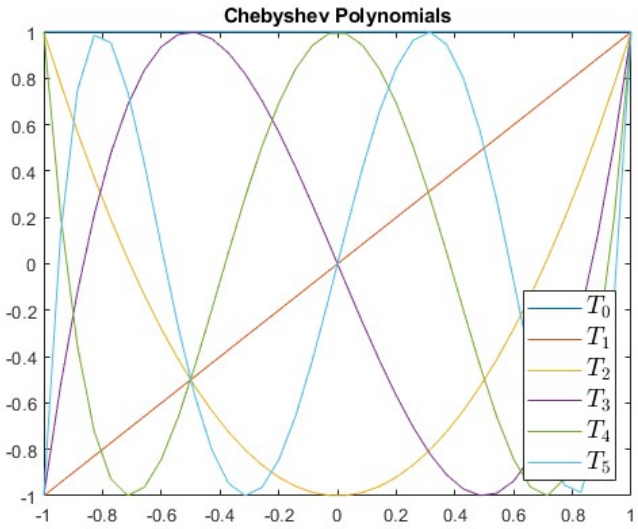

Figure 2.1: First six Chebyshev Polynomials

Legendre Polynomials

Legendre polynomials, $P_n(z)$, are defined by the contour integral

$$P_n(z) = \frac{1}{2\pi i} \oint (1 - 2tz + t^2) t^{(-1/2)} t^{(-n-1)} dt \tag{2.9}$$

Legendre polynomials also remain orthogonal within the same closed range of $[-1, 1]$ as Chebyshev polynomials. They are obtained by using the Gram-Schmidt orthogonalization procedure within the interval.

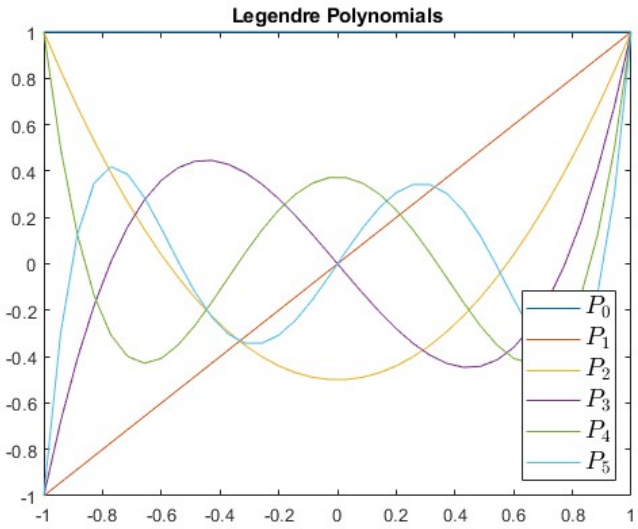

Figure 2.2: First six Legendre Polynomials

Laguerre Polynomials

Laguerre polynomials are given by the solutions to the second order differential equation

$$xy'' + (1 - x)y' + ny = 0 \tag{2.10}$$

The generalized polynomials remain orthogonal over the range of $(0, \infty)$.

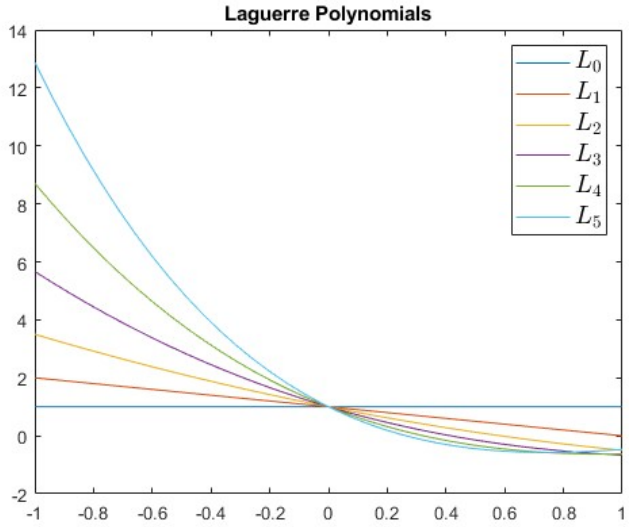

Figure 2.3: First six Laguerre Polynomials

Jacobi Polynomials

Jacobi polynomials are also called hypergeometric polynomials and are given by the solutions to the Jacobi differential equation.

$$(1-x^2)y'' + [\beta - \alpha - (\alpha+\beta+2)x]y' + n(n+\alpha+\beta+1)y = 0 \tag{2.11}$$

They remain orthogonal within the range of $[-1, 1]$.

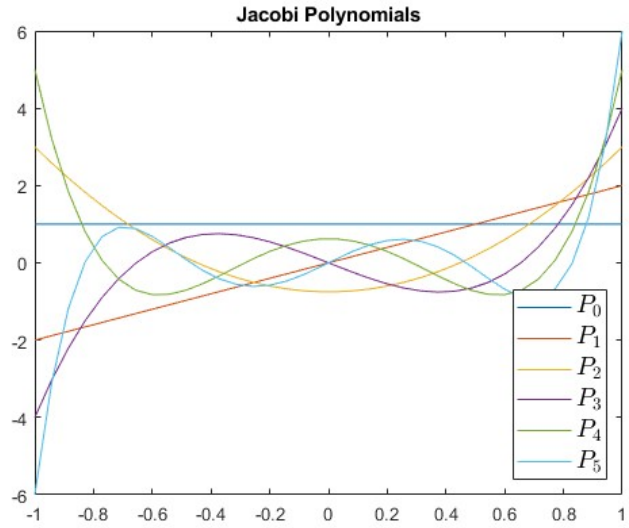

Figure 2.4: First six Jacobi Polynomials with $\alpha = 1$ and $\beta = 1$

Hermite Polynomials

Hermite polynomials, $H_n(x)$, are given by the function

$$H_n(x) = (-1)^n e^{x^2} \frac{d^n}{dx^n} e^{-x^2} \tag{2.12}$$

Hermite polynomials are orthogonal to each other within the range $(-\infty, \infty)$ with respect to a weighting function.

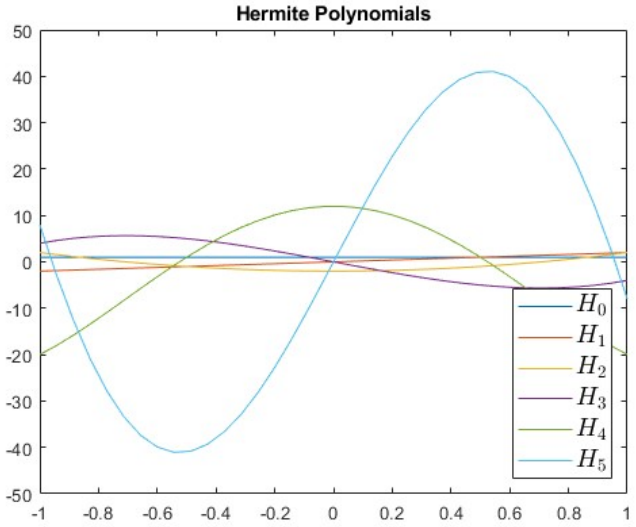

Figure 2.5: First six Hermite Polynomials

There are multiple ways of constructing an orthogonal matrix. Random orthogonal matrices can be generated using operations like Singular Value Decomposition, QR Decomposition and Gram-Schmidt Orthogonalization Procedure.

One of the most common ways to decompose a function is to use these classical orthogonal polynomials. These classical orthogonal polynomials can be used as a base to begin constructing orthogonal matrices with properties explained in Section 2.2. These matrices are constructed by using polynomials as their corresponding rows or columns, with each column in the matrix corresponding to the n^{th} order orthogonal polynomial. The sensitivity matrix S defined below obeys the idea of orthogonality, with its inverse equal to its transpose

$$S = [P_0|P_1|P_2|.....|P_{n-2}|P_{n-1}|P_n] \tag{2.13}$$

Such matrices of size 36×36 are formed using orthogonal polynomials and are displayed on Figure 2.6.

There are multiple methods for constructing orthogonal matrices. The construction of orthogonal matrices can also be achieved using transforms of matrices. Some of them include Householder transformation, Hartley transformation and the Discrete Cosine Transform. Such orthogonal matrices that have been constructed using transforms are displayed in Figure 2.7. The matrices that are being displayed include - *a*) and *b*) The real and complex part of a matrix based on 2D Fourier transformation, *c*) a standard Helmert matrix, *d*) a matrix based on Hartley transform and *e*) a matrix based on DCT (Discrete Cosine Transform).

2.2.2 Spherical Harmonics

Spherical Harmonics are solutions to the Laplace's equation in a spherical domain. They are special functions that are used to represent and expand functions defined on the surface of the sphere

$$\nabla^2\psi = 0. \tag{2.14}$$

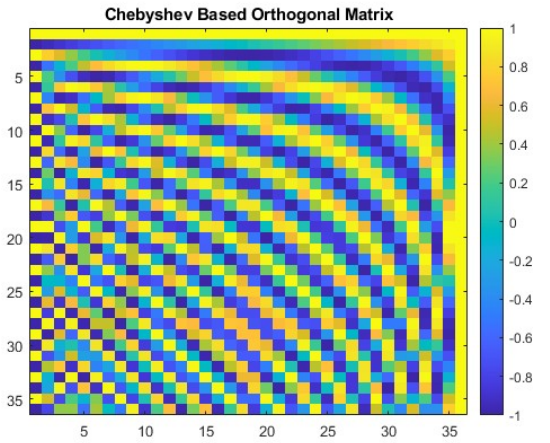

(a) Chebyshev based Orthogonal Matrix

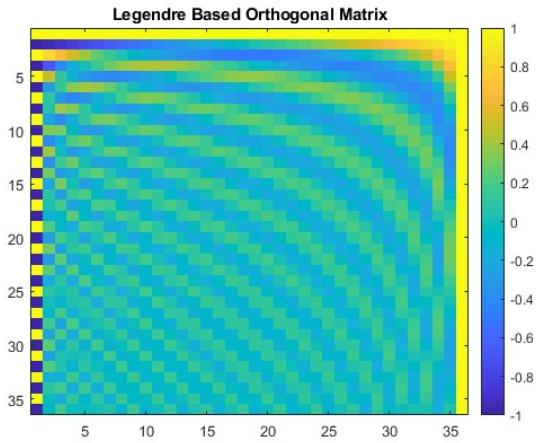

(b) Legendre based Orthogonal Matrix

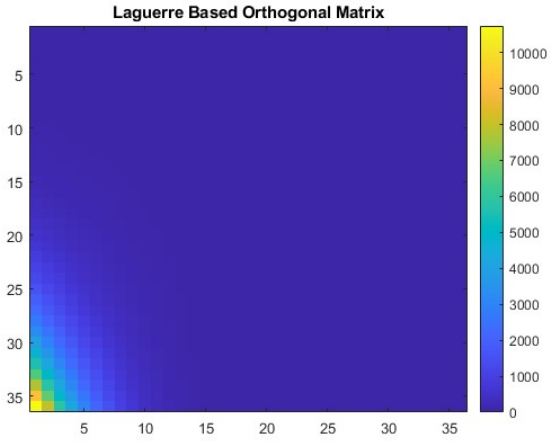

(c) Laguerre based Orthogonal Matrix

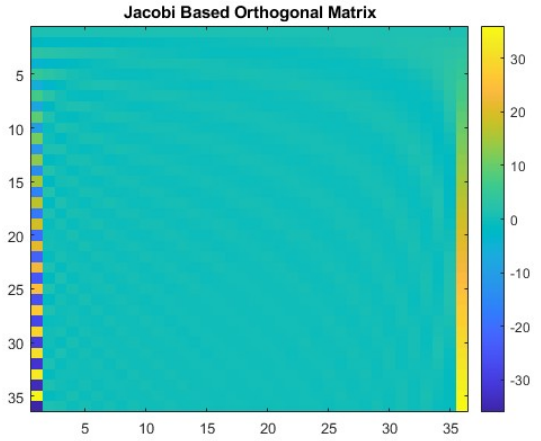

(d) Jacobi based Orthogonal Matrix

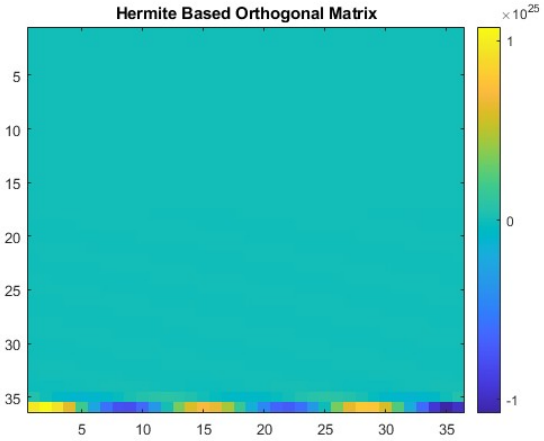

(e) Hermite based Orthogonal Matrix

Figure 2.6: Polynomial based orthogonal matrices

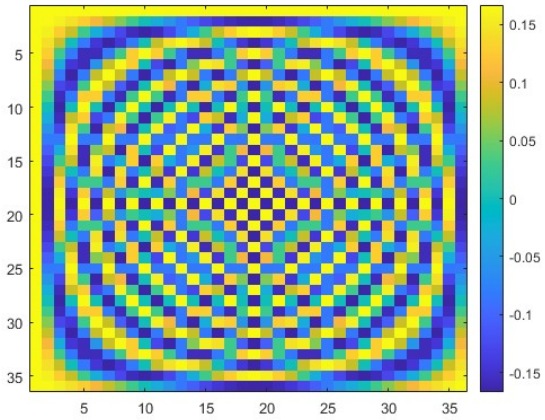

(a) Real part of a complex orthogonal matrix based on 2D Fourier Transforms

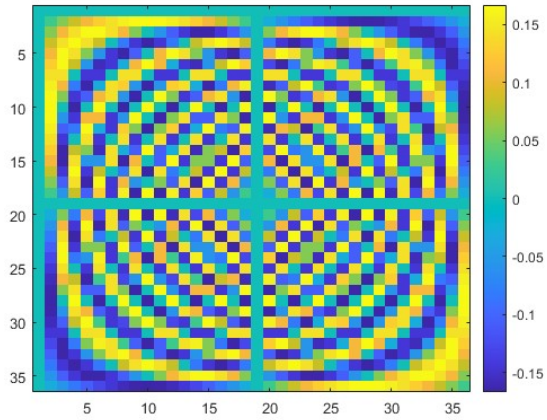

(b) Imaginary part of a complex orthogonal matrix based on 2D Fourier Transforms

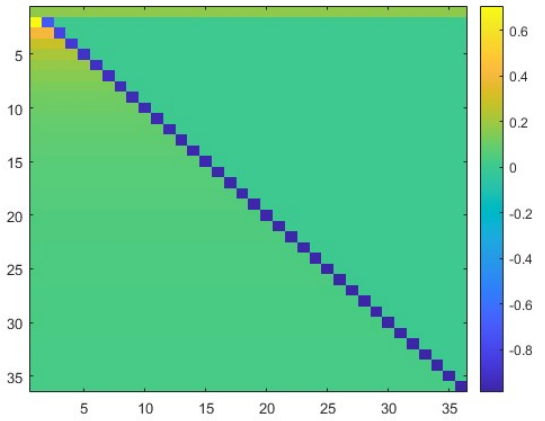

(c) Standard Helmert Matrix

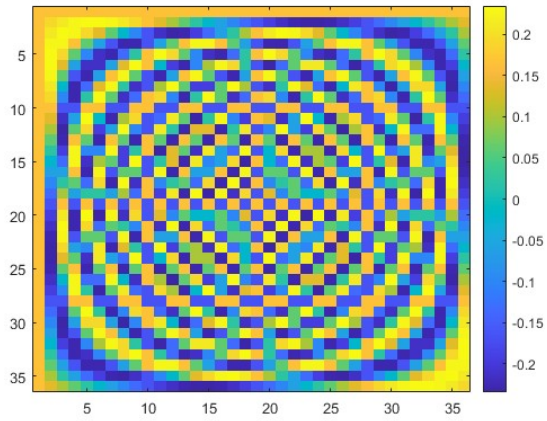

(d) Matrix based on Hartley transform

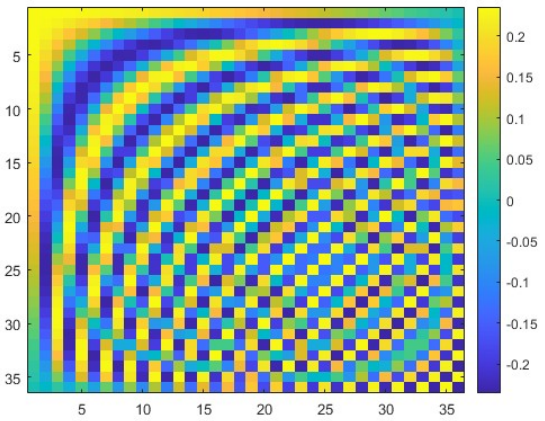

(e) Matrix based on Discrete Cosine Transform

Figure 2.7: Transform based orthogonal matrices

The Laplacian operator in spherical co-ordinates is given by

$$\nabla^2\psi = \frac{1}{r^2}\frac{\partial}{\partial r}(r^2\frac{\partial\psi}{\partial r}) + \frac{1}{r^2\sin(\theta)}\frac{\partial}{\partial\theta}(\sin\theta\frac{\partial\psi}{\partial\theta}) + \frac{1}{r^2\sin^2(\theta)}(\frac{\partial^2\psi}{\partial\phi^2}). \tag{2.15}$$

Solutions to the Laplace equations based on spherical co-ordinates form spherical harmonic polynomials. Spherical harmonics are used to expand out and model geomagnetic field over the surface of the earth, antennae radiation patterns, image compression and restoration, modelling of atomic structures and solving Schrodinger's equation.

Spherical harmonic solutions are orthogonal to each other and hence form a basis set that are used in expansions. Spherical harmonics can also be used to construct orthogonal matrices in multiple dimensions. They are also considered as a $SO(3)$ Lie group with rotational symmetry. Spherical harmonics can be real or imaginary, and they can be realized as vector spherical harmonics.

The spherical harmonic functions are given by

$$Y_n^m(\theta,\phi) = \sqrt{\frac{2n+1}{4\pi}\frac{(n-m)!}{(n+m)!}}e^{im\theta}P_n^m(\cos(\phi)) \tag{2.16}$$

$$n \geq 0, |m| \leq n$$

where n and m are indices along dimensions and P_n^m are corresponding Legendre polynomials.

Multiple works investigate the application of orthogonal decomposition in inverse problems in geomagnetic modelling, surface parameterization, climate change modeling, neuroimaging, convolutional neural networks and optical tweezers by using Helmholtz-Hodge decomposition, some of which were detailed in 1.4.3. Spherical harmonics are orthogonal, linearly independent polynomials that are solutions to the Laplace equation and they form a basis of an orthogonal set. The use of orthogonal fields is helpful in image reconstructions of the required solution of the inverse problem with uniqueness. Furthermore, orthogonality helps in making the ill-posed inversion problem well posed through reduction of the condition number of the sensitivity matrix. While orthogonal matrices can be constructed using multiple well known orthogonal polynomials like Legendre, Chebyshev, Hermite, Laguerre and Jacobi polynomials, as illustrated in Section 2.2.1, spherical harmonics offer a particular advantage in that they can be vectorized and hence easily realizable experimentally using magnetic field sources.

A table of spherical harmonics in Cartesian and polar coordinates is presented.

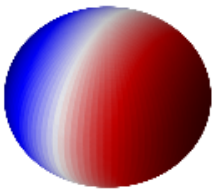

(a) Spherical Harmonic $n = 1, m = -1$, Polar: $\sqrt{\frac{3}{4\pi}}\sin\phi \ \sin\theta$, Cartesian: $\sqrt{\frac{3}{4\pi}}x$

(b) Spherical Harmonic $n = 1, m = 0$, Polar: $\sqrt{\frac{3}{4\pi}}\cos\theta$, Cartesian: $\sqrt{\frac{3}{4\pi}}z$

(c) Spherical Harmonic $n = 1, m = 1$, Polar: $\sqrt{\frac{3}{4\pi}}\cos\phi \ \sin\theta$, Cartesian: $\sqrt{\frac{3}{4\pi}}y$

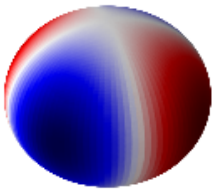

(d) Spherical Harmonic $n = 2, m = -2$, Polar: $\sqrt{\frac{15}{4\pi}}(\sin\phi \ \cos\phi \ \sin^2\theta)$, Cartesian: $\sqrt{\frac{15}{4\pi}}(xy)$

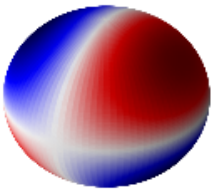

(e) Spherical Harmonic $n = 2, m = -1$, Polar: $\sqrt{\frac{15}{4\pi}}(\sin\phi \ \sin\theta \ \cos\theta)$, Cartesian: $\sqrt{\frac{15}{4\pi}}(yz)$

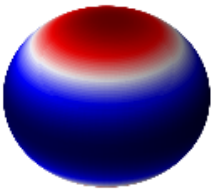

(f) Spherical Harmonic $n = 2, m = 0$, Polar: $\sqrt{\frac{5}{16\pi}}(3\cos^2\theta - 1)$, Cartesian: $\sqrt{\frac{5}{16\pi}}(3z^2 - x^2 - y^2)$

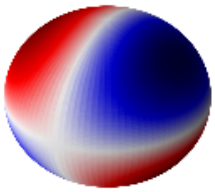

(g) Spherical Harmonic $n = 2, m = 1$, Polar: $\sqrt{\frac{15}{4\pi}}(\cos\phi \ \sin\theta \ \cos\theta)$, Cartesian: $\sqrt{\frac{15}{4\pi}}(xz)$

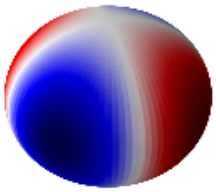

(h) Spherical Harmonic $n = 2, m = 2$, Polar: $\sqrt{\frac{15}{16\pi}}(\cos^2\phi - \sin^2\phi)\sin^2\theta$, Cartesian: $\sqrt{\frac{15}{32\pi}}(x^2 - y^2)$

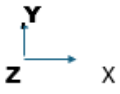

(i) Axes

Figure 2.8: Three dimensional spherical harmonics

Spherical Harmonic Representation		
Spherical Harmonic	Polar Coordinates (θ, ϕ)	Cartesian Coordinates (x, y)
SH 1,-1	$\sqrt{\frac{3}{4\pi}}\sin\phi\ \sin\theta$	$\sqrt{\frac{3}{4\pi}}x$
SH 1,0	$\sqrt{\frac{3}{4\pi}}\cos\theta$	$\sqrt{\frac{3}{4\pi}}z$
SH 1,1	$\sqrt{\frac{3}{4\pi}}\cos\phi\ \sin\theta$	$\sqrt{\frac{3}{4\pi}}y$
SH 2,-2	$\sqrt{\frac{15}{4\pi}}(\sin\phi\ \cos\phi\ \sin^2\theta)$	$\sqrt{\frac{15}{4\pi}}(xy)$
SH 2,-1	$\sqrt{\frac{15}{4\pi}}(\sin\phi\ \sin\theta\ \cos\theta)$	$\sqrt{\frac{15}{4\pi}}(yz)$
SH 2,0	$\sqrt{\frac{5}{16\pi}}(3\cos^2\theta - 1)$	$\sqrt{\frac{5}{16\pi}}(3z^2 - x^2 - y^2)$
SH 2,1	$\sqrt{\frac{15}{4\pi}}(\cos\phi\ \sin\theta\ \cos\theta)$	$\sqrt{\frac{15}{4\pi}}(xz)$
SH 2,2	$\sqrt{\frac{15}{16\pi}}(\cos^2\phi - \sin^2\phi)\sin^2\theta$	$\sqrt{\frac{15}{32\pi}}(x^2 - y^2)$

Three dimensional spherical harmonic polynomials are displayed in Figure 2.8.

2.2.3 Two Dimensional Spherical Harmonic Fields

The orthogonality of spherical harmonic polynomials can be a huge boost to solving inverse problems. Since inverse problems are solvable more efficiently using orthogonal matrices, constructing and implementing them as a physical system can enable enormous progress in tackling such problems.

Vector fields and vector potentials can be defined and constructed in such a way that the matrix representing the system is orthogonal and linearly independent. Two dimensional vector spherical harmonics can be used to construct linearly independent, well conditioned, orthogonal matrices that are implementable experimentally and which prove beneficial in solving inverse algorithms.

Inverse problems often work on the principle of having a calculated forward model and using error prone recorded data to arrive back at the input parameters that need to be found. Inversion of a matrix forms a vital part of solving such problems and the use of two dimensional vector spherical harmonics and the orthogonality that they provide can be helpful. A well conditioned matrix is easier to invert and spherical harmonic polynomial based matrices are well conditioned.

Two dimensional vector spherical harmonics also form a 2D Fourier basis in space. Figure 2.9 presents two dimensional vector based spherical harmonics that are required to form linearly independent and orthogonal matrices. It displays a series of quiver plots that can be emulated and used in the construction of orthogonal matrices, within a two dimensional square of dimensions 1×1 units.

2.3 Magnetic Induction Tomography

Magnetic Induction Tomography is an imaging method that operates on the principle of Faraday's law of electromagnetic induction. It images a region of interest by inducing eddy currents

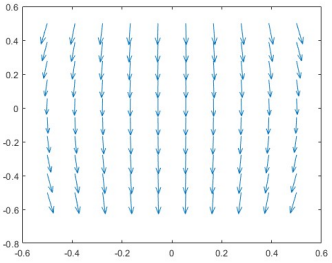

(a) Spherical Harmonic $n = 1, m = -1$, Cartesian: $\sqrt{\frac{3}{4\pi}}x$, $(\frac{\partial B_y}{\partial y})$

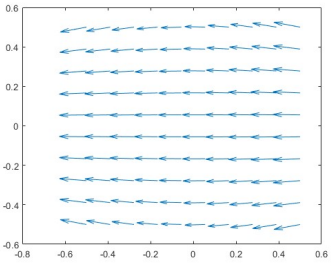

(c) Spherical Harmonic $n = 1, m = 1$, Cartesian: $\sqrt{\frac{3}{4\pi}}y$, $(\frac{\partial B_x}{\partial x})$

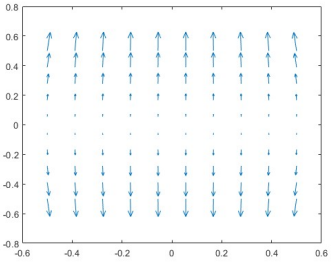

(e) Spherical Harmonic $n = 2, m = -1$, Cartesian: $\sqrt{\frac{15}{4\pi}}(yz)$

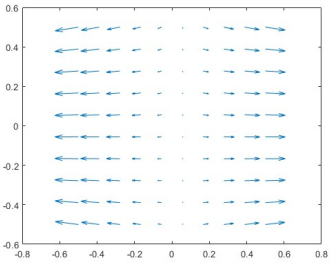

(g) Spherical Harmonic $n = 2, m = 1$, Cartesian: $\sqrt{\frac{15}{4\pi}}(xz)$

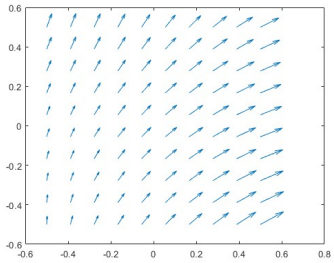

(b) Spherical Harmonic $n = 1, m = 0$, Cartesian: $\sqrt{\frac{3}{4\pi}}z$

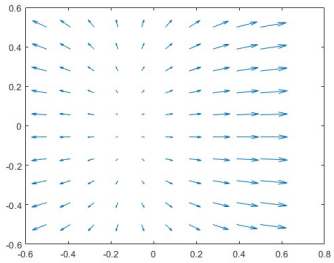

(d) Spherical Harmonic $n = 2, m = -2$, Cartesian: $\sqrt{\frac{15}{4\pi}}(xy)$

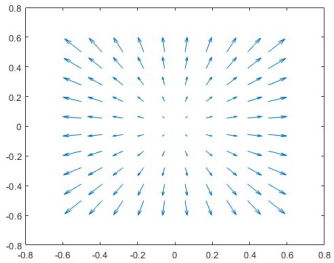

(f) Spherical Harmonic $n = 2, m = 0$, Cartesian: $\sqrt{\frac{5}{16\pi}}(3z^2 - x^2 - y^2)$, $(\frac{\partial^2 B_x}{\partial x^2} + \frac{\partial^2 B_y}{\partial y^2})$

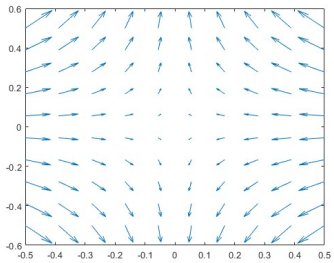

(h) Spherical Harmonic $n = 2, m = 2$, Cartesian: $\sqrt{\frac{15}{32\pi}}(x^2 - y^2)$, $(\frac{\partial^2 B_x}{\partial x^2} - \frac{\partial^2 B_y}{\partial y^2})$

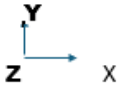

(i) Axes

Figure 2.9: Two dimensional vector spherical harmonics visualized using quiver plots

within the region. Due to its non-invasive, non-ionising nature, it has been extensively studied and employed in applications like biomedical imaging and diagnosis, geomagnetic surveying, non-destructive testing and evaluation, security and food processing.

Magnetic Induction Tomography consists of two primary parts - the forward problem and the inverse problem. In the forward problem, a primary, oscillating magnetic field is created within the region of interest of imaging, which induces eddy currents and, in turn, creates secondary magnetic fields, that are then detected using a magnetic field sensor [95]. A sensitivity matrix is built from the components of the forward model. The detected magnetic fields are used in an inverse problem to image the region.

One of the defining challenges that Magnetic Induction Tomography based imaging encounters is the inverse problem and the reconstruction of the conductivity distribution within the region of interest. By building orthogonal sensitivity matrices through spherical harmonic magnetic fields, we are able to improve the efficiency of inversion algorithms used in the final reconstruction by reducing the ill-posed nature of the inverse problem. Orthogonal sensitivity matrices also help to avoid interference and cross-talk, use the excitor magnetic fields to provide unique solutions and cover the required region of interest completely.

An experimental setup is built where spherical harmonic magnetic fields are used to induce eddy currents within the region of interest of imaging. A Hall effect magnetic field sensor is used to sense and detect the eddy current induced magnetic fields. COMSOL is used to calculate the field strength of secondary magnetic fields. The detected secondary magnetic fields are used in the inverse formulation of the problem to arrive at the final distribution of conductivity corresponding to the final image of the region of interest. Two different algorithms are presented to solve the inverse problem - Linear Back Projection and Tikhonov Regularization, and a comparison between the two of them is drawn.

The chapter consists of the following three parts within its workflow.

- Creation of spherical harmonic magnetic vector fields by solving the Laplace equation and implementing them experimentally to act as the primary magnetic fields by varying currents in coils [95]. In a region without an eddy current source, both the divergence and the curl of the magnetic vector field is 0. By applying Coulomb's gauge ($\nabla \cdot A = 0$) and since the curl of the magnetic field is zero, the following equations are obtained to solve for spherical harmonics.

$$\nabla^2 \psi = 0 \tag{2.17}$$

$$\nabla^2 \vec{A} = 0 \tag{2.18}$$

  Equation 2.18 is further explained in Section 2.4. It can be seen that, in the absence of electrical conductivity within the region of interest, the eddy current generated within the region is 0 A. The magnetic vector potential is calculated only using the source current provided to generate the primary excitor magnetic fields.

- Calculation of the field strength of the eddy current induced secondary magnetic fields using COMSOL and building the sensitivity matrix within the region of interest [96] [97].

$$\nabla^2 \vec{B_e} + k^2 \vec{B_e} = -k^2 \vec{B_i} \tag{2.19}$$

$$\frac{\nabla^2 \vec{A}}{\mu} = -\vec{J_e} \tag{2.20}$$

- Solving the inverse problem from experimentally obtained secondary magnetic fields using inverse algorithms in order to arrive at the final conductivity distribution within the region of interest.

$$S\sigma = \vec{B_e} \tag{2.21}$$

$$\sigma \cdot \begin{bmatrix} \frac{\partial H_1}{\partial \sigma_1} & .... & \frac{\partial H_1}{\partial \sigma_n} \\ .... & .... & .... \\ \frac{\partial H_n}{\partial \sigma_1} & .... & \frac{\partial H_n}{\partial \sigma_n} \end{bmatrix} = \frac{1}{\mu}(B_e) \tag{2.22}$$

$$\sigma = cS^{-1}\vec{B_e} \tag{2.23}$$

The sensitivity matrix is calculated using the Jacobian matrix of the system. The rate of change of the magnetic field detected in the secondary elements or the rate of change of voltages detected in the sensing elements to the electrical conductivity of the domain is calculated at every nodal point within the domain. From 1.29, it can be seen that it can be detected by measuring the secondary eddy generated magnetic fields. Every element within the sensitivity matrix S corresponds to $\frac{\partial H}{\partial \sigma}$ or $\frac{\partial V}{\partial \sigma}$. The experimentally measured magnetic fields or sensed voltages are caused due to the conductivity distribution of the domain. Thus these changes can be formulated as an inverse problem, where the source is calculated from the observed effect. In this case, a proportionality constant c that describes the system could be added to the inverse problem in accordance with the formulation. Normally, this is dealt with by the normalization of the sensitivity matrix, making them dimensionally equivalent.

Here, ψ is the magnetic scalar potential of the system, A is the magnetic vector potential, B_i is the primary magnetic field generated by the coils, B_e is the secondary magnetic field induced due to eddy currents, k is the skin depth of the sample, J_e is the strength of the generated eddy current and σ is the electrical conductivity of the sample. A is used to indicate magnetic vector potential both in (2.20) and (2.21), both as part of the PDE (Partial Differential Equation) and as part of the sensitivity matrix.

2.4 Spherical Harmonic Magnetic Fields

In general, Maxwell's equations to determine the magnetic fields and magnetic vector potentials within a domain are given by

$$\nabla \cdot \vec{B} = 0 \tag{2.24}$$

$$\nabla \times \vec{B} = -\frac{\partial \vec{E}}{\partial t} \tag{2.25}$$

where $\vec{E}$ is the electric field and B is the magnetic field.

In order to generate spherical harmonic vector magnetic fields within the required region of interest, the design philosophy of Romeo and Hoult [58] is followed. Considering Maxwell's equations for a region without a current source, the magnetic field within this region is given by

$$\nabla \cdot \vec{B} = 0 \tag{2.26}$$

$$\nabla \times \vec{B} = 0 \tag{2.27}$$

(according to Ampere's law, as $J = \frac{\partial B}{\partial t} = 0$)

The magnetic field is given by the curl of the magnetic vector potential A.

$$\vec{B} = \nabla \cdot \psi = \nabla \times \vec{A} \tag{2.28}$$

where ψ is the scalar potential.

When the Coulomb gauge is applied, it gives rise to three Laplacian equations [95].

$$\nabla \cdot \nabla\psi = \nabla \times \nabla \times \vec{A} = 0 \tag{2.29}$$

$$\nabla^2\psi = \nabla^2\vec{A} = 0 \tag{2.30}$$

The solutions to the Laplace equation is provided through Tesseral Spherical Harmonic functions within the region of interest. In two dimensions, spherical harmonics also take the shape of a 2D Fourier basis.

$$T_{nm}(\theta,\phi) = C_{nm}\begin{pmatrix} r^n \\ r^{-n-1} \end{pmatrix} P_{nm}(\cos\theta)\begin{pmatrix} \sin m\phi \\ \cos m\phi \end{pmatrix} \tag{2.31}$$

$$Y_n^m(\theta,\phi) = \sqrt{\frac{2n+1}{4\pi}\frac{(n-m)!}{(n+m)!}}e^{im\theta}P_n^m(\cos(\phi)) \tag{2.32}$$

The required magnetic field is derived from the Tesseral Spherical Harmonic formulation. A Biot-Savart law based least squares inverse formulation is used to arrive at the current distribution required for the desired spherical harmonic magnetic vector fields [95].

$$\vec{B}(r) = \frac{\mu}{4\pi}\iiint \frac{\vec{J_s}(r') \times |\vec{r} - \vec{r'}|}{|\vec{r} - \vec{r'}|^3} d^3r' \tag{2.33}$$

$$\Phi = \sum_j (B_j^{desired} - \sum_{k=1}^{K} I_k M_{jk}^I)^2 \tag{2.34}$$

where $B(r)$ represents the magnetic field that is to be generated as part of the primary magnetic field, J_s determines the source current of the excitor coils. Equation 2.32 represent the Biot- Savart law, and 2.33 represents the optimization problem that is solved to arrive at the required current distribution from the primary excitor coils. $B^{desired}$ is the required target magnetic field, M is the sensitivity matrix consisting of sensitivities to the overall magnetic field from individual wire elements of the excitor coils and I_k is the required current distribution for the derived target fields.

The four spherical harmonics, shown in Figure 2.10, chosen for the experiment are given by the following n and m values.

1. $n = 1;\ m = 1$; Spherical Harmonic Variation ($\frac{\partial \vec{B_y}}{\partial y}$)
2. $n = 1;\ m = -1$; Spherical Harmonic Variation ($\frac{\partial \vec{B_x}}{\partial x}$)
3. $n = 2;\ m = 0$; Spherical Harmonic Variation ($\frac{\partial^2 \vec{B_x}}{\partial x^2} + \frac{\partial^2 \vec{B_y}}{\partial y^2}$)
4. $n = 2;\ m = 2$; Spherical Harmonic Variation ($\frac{\partial^2 \vec{B_x}}{\partial x^2} - \frac{\partial^2 \vec{B_y}}{\partial y^2}$)

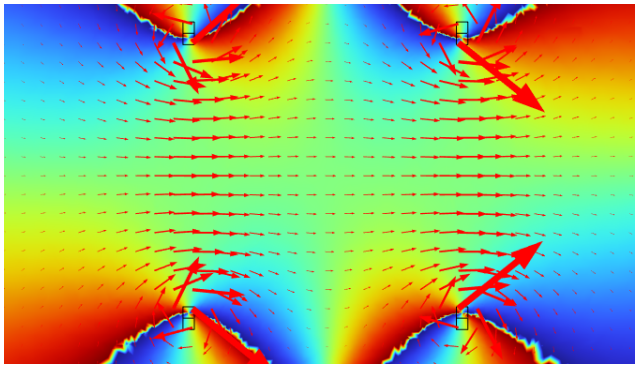

(a) Spherical Harmonic $n = 1, m = 1$ ($\frac{\partial B_y}{\partial y}$)

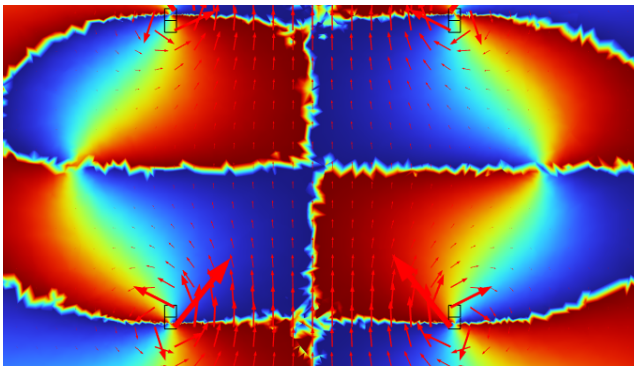

(b) Spherical Harmonic $n = 1, m = -1$ ($\frac{\partial B_x}{\partial x}$)

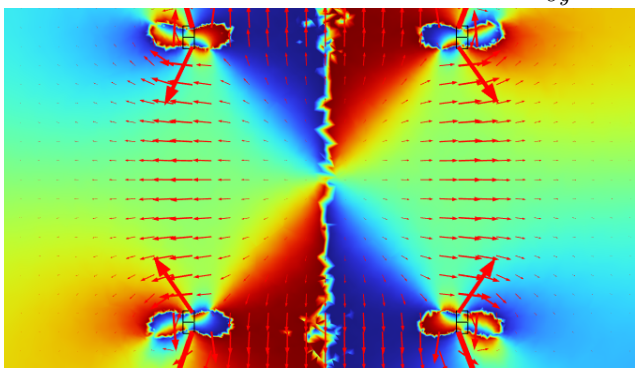

(c) Spherical Harmonic $n = 2, m = 0$ ($\frac{\partial^2 B_x}{\partial x^2} + \frac{\partial^2 B_y}{\partial y^2}$)

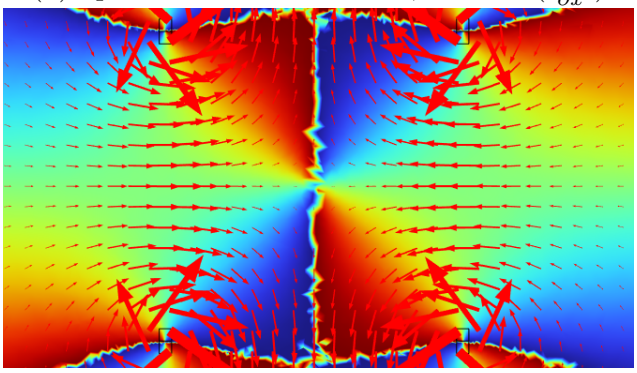

(d) Spherical Harmonic $n = 2, m = 2$($\frac{\partial^2 B_x}{\partial x^2} - \frac{\partial^2 B_y}{\partial y^2}$)

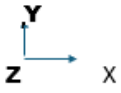

(e) Axes

Figure 2.10: Quiver Plots of Spherical Harmonic Vector Magnetic Fields

In Figure 2.10, the quiver plots showcases the directions of the spherical harmonic magnetic fields, while the colour plots indicate the phase variations caused by the primary excitor fields. As it can be seen from Figure 2.10, the phase and field patterns indicate that the target fields will produce unique responses from the region of interest. Thus it can be seen that, the primary magnetic field determined by various spherical harmonics are effective in producing unique reconstructions as their field and phase variations target different parts of the region of interest.

2.5 Calculation of Eddy Current Induced Secondary Magnetic Fields

Eddy currents are generated whenever there is a change in the magnetic field B, according to Faraday's law.

$$\nabla \times \vec{E} = -\frac{\partial \vec{B}}{\partial t} \tag{2.35}$$

$$\vec{J} = \sigma \vec{E} \tag{2.36}$$

where σ is the electrical conductivity of the sample.

The primary magnetic field is created by a time-varying, alternating electric current which when passed through excitor coils, generates a varying magnetic flux. The magnetic flux density from the primary excitor coil creates the required magnetic field. This time-varying flux in turn produces an alternating electric field, which when acts within the conducting region of interest, produces eddy currents. This conductivity within the region of interest is sought to be reconstructed in the inverse problem. The eddy current generated, in turn, produces secondary magnetic fields that are detected by the magnetometer to be used in formulating and solving the inverse problem.

According to eddy current theory, the magnetic vector potential is given by the equation [98]

$$\nabla \times \frac{1}{\mu} \nabla \times \vec{A} + j\omega\sigma\vec{A} = \vec{J}_s \tag{2.37}$$

where μ is the permeability of the region of interest, $\vec{J}_s$ is the source current used to create the applied primary magnetic field $\vec{B}_i$

In order to calculate the secondary, induced magnetic field from the eddy current generated by the applied primary magnetic field, a quasistatic approximation is used and it takes the form of an inhomogeneous Helmholtz equation.

$$\nabla^2 \vec{B}_e + k^2 \vec{B}_e = -k^2 \vec{B}_i \tag{2.38}$$

where k is determined by the skin depth.

2.5.1 Skin Depth

Skin depth, δ, is defined as the distance within the sample to which the induced eddy currents penetrate. It is a measure of depth up to which electrical conduction takes place within a

material. It helps us in determining the frequency at which Magnetic Induction Tomography can be carried out for different materials. It is given by

$$\delta = \sqrt{\frac{2\rho}{\omega\mu_0\mu_r}} \tag{2.39}$$

which is modified as

$$\delta = \sqrt{\frac{1}{\pi\sigma f\mu_0\mu_r}} \tag{2.40}$$

where δ is the skin depth, ρ is the resistivity of the material, ω is the angular frequency, f is the frequency, μ_0 is the permeability of free space, μ_r is the relative permeability and σ is the conductivity of the material.

In general, the larger the skin depth, the easier it becomes to image the object present within the region of interest.

2.5.2 Computational Simulations and Meshing

The eddy current based induced magnetic field is calculated using COMSOL simulations in its AC/DC Electromagnetics module [99]. Coils similar to the ones used in the experiment are used in the simulation. A fine mesh is used in the computational simulation which uses the Finite Element Method. The simulation is performed using the source current, the conductivity and permeability of the sample and the frequency as inputs and both the applied and induced (primary and secondary) magnetic fields are solved using it.The forward modeling calculations from the simulation are used in the formulation of the sensitivity matrix, which is later used in the inverse problem.

Meshing forms an important and a significant part of numerical analysis methods. Meshing also determines how accurate or noisy the simulations can be. Computational simulations require the domain where the Partial Differential Equation to be solved to be discretized into multiple smaller elements. The domain is to be subdivided into a number of nodes which could be combined together to form elements. There are multiple possible methods like Voronoi Tesellations and Delauney triangulations that can be used to subdivide the domains into nodes. The mesh elements can be of multiple shapes and size in order to attain and cover all the domains and the universe.

In this simulation, the element size is chosen to be extremely fine and the mesh is allowed to be a physics controlled mesh. The chosen mesh element shape is tetrahedral. The number of vertex elements is 192, the number of edge elements is 4274, the number of boundary elements is 103562 and the total number of elements in this simulation computed is 3009979. The maximum element size upon meshing is 0.004 m, and the minimum element size is 0.0014 m. The coarsest meshing gives rise to 5577 low quality tetrahedral elements within the universe. In general, in numerical simulations and computations, there is a trade-off between element size and computation time. The smaller the element size is, the finer the mesh is and hence the longer it takes to finish computations, but the results are less error-prone. Coarser meshes with smaller mesh sizes and quick and easy to solve, but are not as accurate as results with a finer mesh. It is possible to use user-defined meshes with customised element sizes and further mesh refinement.

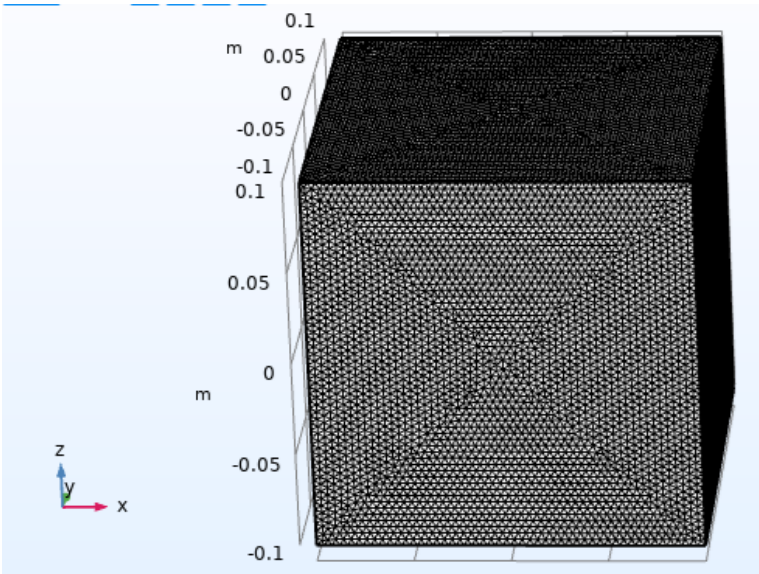

Figure 2.11: Extremely Fine Mesh

The application of spherical harmonic based primary magnetic vector fields becomes prominent when the Helmholtz equation is analyzed and considered in matrix form. In the absence of a sample within the region of interest, the governing equation is 2.18, a Laplace equation, which when expressed in matrix form becomes $A\sigma = 0$. When the primary magnetic field is shaped in a way that is a solution of this equation (Laplace equation), the inversion problem goes from an ill-posed problem to a more well-posed problem. In the presence of a sample within the region of interest, the governing equation is given by the inhomogeneous Helmholtz equation [100]. It is given by 2.20 and is represented in matrix form as $A\sigma = \mu J_e$. Spherical harmonics present an ideal solution to the Laplace equation. In the approach of this chapter, the ideal solutions are computed initially and are used as primary fields to probe the region of interest, and that aids in inversion when a sample is present by improving the condition number of the inversion problem and by providing unique solutions.

2.6 Experimental Setup

2.6.1 Skin Depth Calculations

If one seeks to image across the area of 40 mm ×40 mm, it is sensible to have a skin depth of at least 1 mm, so that the imaging and characterization can be done efficiently. Depending upon this targeted area and the range in conductivity to be measured, the frequency at which Magnetic Induction Tomography is to be performed is determined. In general, the frequency of the experiment and the skin depth are inversely proportional, as shown in Figure 2.12.

Since metallic objects are sought to be imaged initially, the following assumptions are made while calculating the skin depth. The conductivity σ is taken to be $5.8 \times 10^7 Sm^{-1}$. The magnetic permeability of free space is given by $4\pi \times 10^{-7} Hm^{-1}$ and relative permeability of copper is given by 0.9999. Based upon this, the frequency is decided to be 2000 Hz, as the skin depth at this frequency is 1.5 mm. It is indicated by the red circle shown in Figure 2.12.

$$\delta = \sqrt{\frac{1}{\pi \times 5.8 \times 10^7 \times 2000 \times 4\pi \times 10^{-7} \times 0.9999}} = 0.0015 \text{ m} \tag{2.41}$$

Usually, it would have been preferable to have the skin depth penetrate the complete sample. But the tradeoff is that the experiment will have to be performed at a lower frequency, which in turn influences the strength of the secondary magnetic fields generated due to eddy currents. That, as a consequence, would require for the sensing Hall probe based magnetometer to have a higher sensitivity than possible. Hence, a balance is struck between skin depth and frequency so that the sample is sufficiently penetrated at an optimal frequency which can induce secondary magnetic fields detectable at a distance.

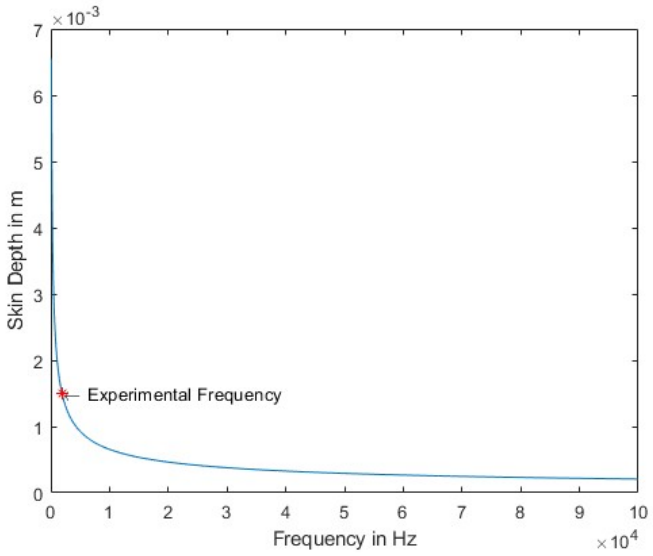

Figure 2.12: Frequency vs. Skin Depth

2.6.2 Coil Design and Specifications

Magnetic excitation fields are generated using current carrying conductors, based on Ampere's law.

$$\nabla \times \vec{H} = \vec{J} \tag{2.42}$$

where $\vec{H}$ is the magnetic field and $\vec{J}$ is the eddy current strength.

Coils and induction systems are used as a source for magnetic fields and they are designed using the Biot- Savart law, given by 2.32, as mentioned in Section 4.

$$\vec{B}(r) = \frac{\mu}{4\pi} \iiint \frac{\vec{J}_s(r') \times |\vec{r} - \vec{r'}|}{|\vec{r} - \vec{r'}|^3} d^3r' \tag{2.43}$$

To implement the considered four target orthogonal excitor fields illustrated under Figure 2.10, a simple coil based excitor setup is opted for and implemented. The design of the excitor is a square shaped coil [101] with the side of the outer perimeter $L1$ being 54 mm and the side of the inner perimeter $L2$ being 50 mm. The coil has 100 windings, which are required to get the excitor magnetic field to the order of 1×10^{-4} T to $5 \times 10^{-4}T$. It uses a Standard Wire Gauge No. 31 with a wire diameter of 0.2 mm. It has 10 layers and 10 turns per layer, which brings up the number of windings to 100.

The inductance L of a rectangular coil of width W, height h and diameter of wire d can be calculated using the following equation [102].

$L = \frac{\mu_0 \mu_r}{\pi}[-2(W+h) + 2\sqrt{W^2+h^2} - h\ ln(\frac{h+\sqrt{W^2+h^2}}{W}) - W\ ln(\frac{W+\sqrt{W^2+h^2}}{h}) + h\ ln(\frac{2h}{d/2}) + W\ ln(\frac{2W}{d/2})]$

Since it is a square coil, it can be considered that $W = h$. This formula for inductance calculation reduces to

$$L = -2.9346W + 2W\,ln(\frac{2W}{d/2}) \tag{2.44}$$

Based upon this formula, the self inductance of the coil is calculated to be 2.1 mH, by considering $W = L2$. The inner side of the square coil provides the required side length for inductance calculation of the square coil. This was also confirmed using a multimeter experimentally.

Figure 2.13: Coil Specifications

2.6.3 Design Choices

Once the coil design has been finalized, the required target fields are generated. A four coil based square shaped setup is used to induce and achieve spherical harmonic target excitor fields across an area of $40 \times 40mm^2$.

The required target fields are implemented and executed by using a parallel inductor combination. The four coils are connected in parallel to each other, and a constant voltage is maintained across the coils. The current into each coil is regulated through an RF amplifier. The directionality of the current is changed in order to arrive at the four target fields, as seen through the inverse modeling that was done. The current passing through the overall circuit across excitor coils is given by

$$I = \frac{V}{L_p \omega} = \frac{V}{L_p(2\pi f)} \tag{2.45}$$

Since the coils are connected in parallel and all the coils have the same inductance, the overall inductance of the circuit is given by

$$\frac{1}{L_p} = \frac{1}{L_1} + \frac{1}{L_2} + \frac{1}{L_3} + \frac{1}{L_4} \tag{2.46}$$

It is known that,

$$L_1 = L_2 = L_3 = L_4 = L \tag{2.47}$$

$$L_p = L/4 \tag{2.48}$$

(a) Four Coil Setup for Orthogonal Fields

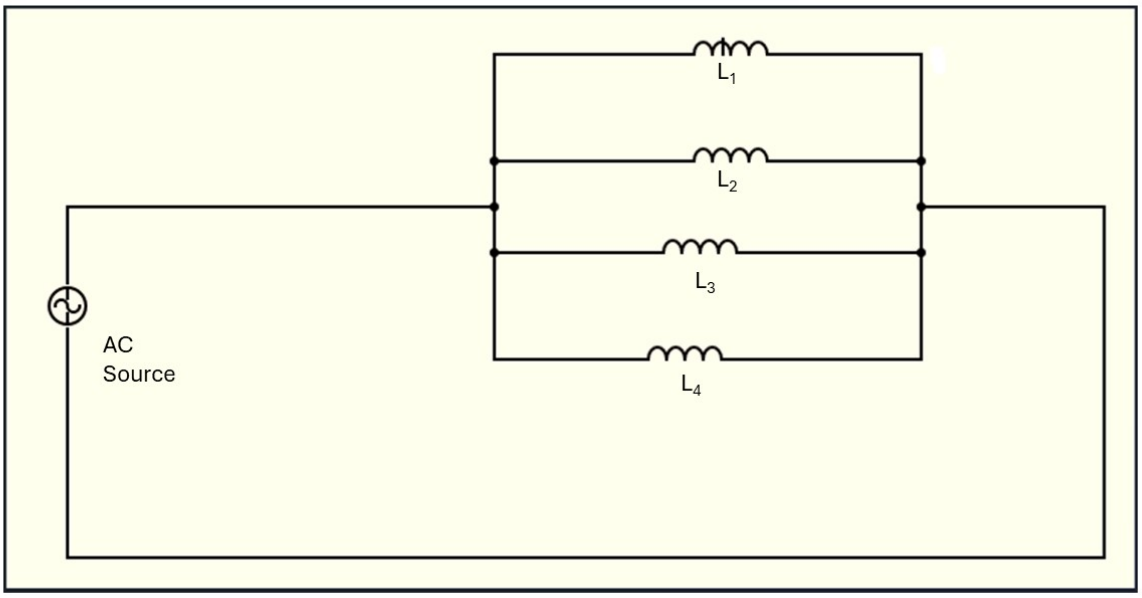

(b) Circuit Diagram consisting of the excitor coils with inductances L_1,L_2,L_3 and L_4 in parallel

Figure 2.14: Four Coil Setup and Circuit Diagram

The RF amplifier is responsible for providing a signal amplification of 7 V_{P-P}. Hence, the current through each excitor coil in terms of its magnitude is given by

$$I_1 = I_2 = I_3 = I_4 = I \tag{2.49}$$

$$I = \frac{7}{2 \times \pi \times 2 \times 10^3 \times 2.15 \times 10^{-3}} = 0.2603 \text{ A} \tag{2.50}$$

The current through each coil is given by 260.3 mA, the direction of the current is changed in accordance with the targeted excitor field required and that helps to achieve the spherical

harmonic based magnetic field. For higher order spherical harmonics, it is possible to look into different excitor coil configurations, changing the magnitude and the direction of the excitor current and using individual current amplifiers to excite individual coils. The derived current ratios are featured in Figure 2.15. It plots the relative current which passes through the four excitor coils, as a ratio of the total amount of current derived from the optimization algorithm used to solve Equation 2.34. The current ratio differences on the excitor coils helps create the spherical harmonic magnetic fields. The combination of magnetic fields from different coils with its current ratios creates the required spherical harmonic excitor magnetic fields.

Based on computational simulations from COMSOL, it is determined that, for excitor coil based primary fields of $0.1 - 0.5$ mT, the secondary magnetic fields based on eddy currents are $0.5 - 2$ μT. The eddy current based secondary fields are also AC based RF fields with a frequency and hence, a Lakeshore Teslameter [103] with a RF frequency range of DC to 75 kHz and a sensitivity of 0.1 μT was chosen to be the magnetic field measuring device for the experiment. The magnetometer works via the Hall effect, the classical phenomenon by which a potential is developed across an applied magnetic field.

The required vector spherical harmonic magnetic fields are generated using an experimental setup of four square coils. Figure 2.16 presents a block diagram of the planned experimental setup. It consists of a signal generator, a Radio Frequency (RF) amplifier which is used to amplify the input signal from the signal generator, the excitor coils that are used to create the primary magnetic fields and the magnetometer used to measure the secondary magnetic field as its building blocks. The final output is recorded and the data is acquired by the data accumulator [104], while the oscilloscope is used for input signal measurements.

The different patterns and sequences in which the coils were powered were derived from the current distribution are described in Section 2.3. Figure 2.17 presents the mounted experimental setup upon an optical breadboard and showcases the setup in measurement. The region of interest considered to be imaged is a plane of size 40 mm $\times$ 40 mm across the X-Y plane. Figure 2.18 shows the region of interest and the plane where Magnetic Induction Tomography is performed, shaded in red.

A standard signal generator was used to generate the required AC current and it was amplified using a RF amplifier to arrive at the required current. The current was then used to drive the excitor coils present within the four-coil setup. A cubical copper sample of dimensions 10 mm $\times$ 10 mm $\times$ 10 mm was used as the sample to be imaged. The sample was placed within the region of interest and the output was measured using a tri-axial Lakeshore magnetometer with a sensitivity of 0.1 μT in an open environment. The magnetometer uses the Hall effect to measure the magnetic field. The magnetometer probe was attached to a translational linear stage [105]. The data from the magnetometer was acquired using a data acquisition device using LabVIEW. The magnetic field magnitude and phase were measured at 36 different positions around the region of interest in the presence of the sample and without it. A difference measurement system is used to find the magnetic field magnitude and phase difference caused due to the sample. The eddy current based secondary magnetic field induced within the region of interest is measured in this manner using differential measurement.

The translational stage used was a Thorlabs 50 mm high speed DC servo stage. It had a dynamic range of 50 mm and a minimum achievable resolution or sensitivity of 0.05 μm. The measurements were performed at 8 different points in steps of 5 mm each, along all four cardinal directions, with the sensor being positioned at 32 different points across the region of interest. Six measurements were made at each position with and without the copper sample, as it was

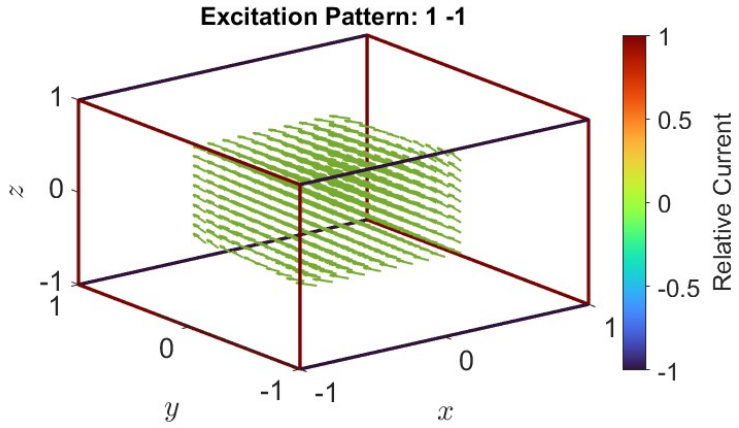

(a) SH 1,-1

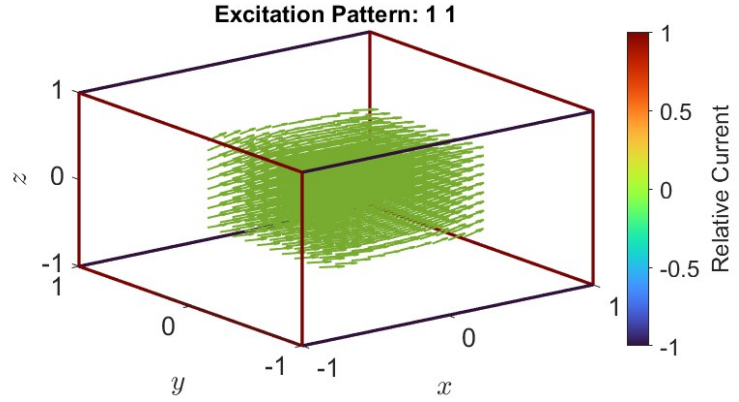

(b) SH 1,1

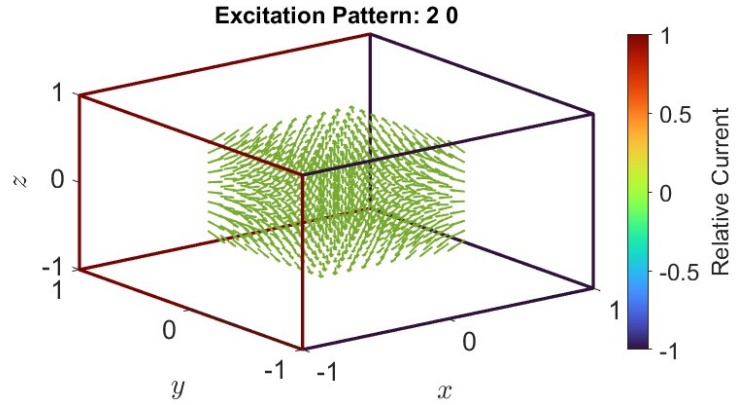

(c) SH 2,0

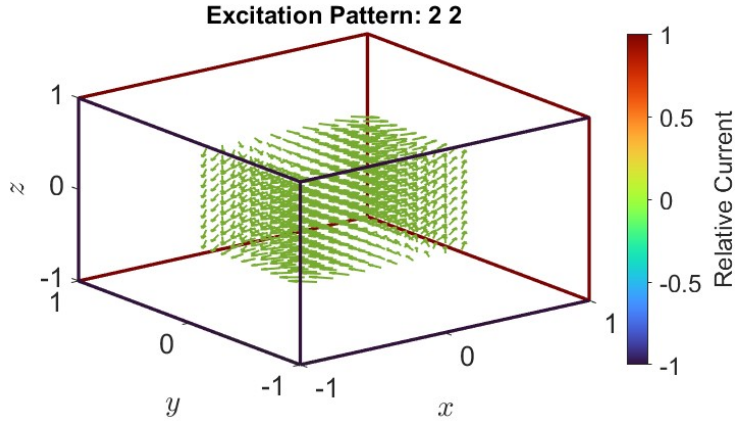

(d) SH 2,2

Figure 2.15: Current Configurations for Excitor Coils

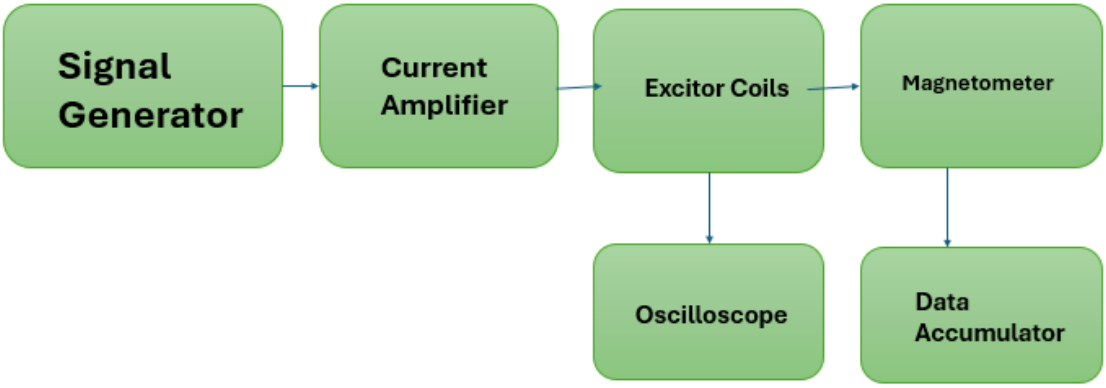

Figure 2.16: Experimental Setup Planning

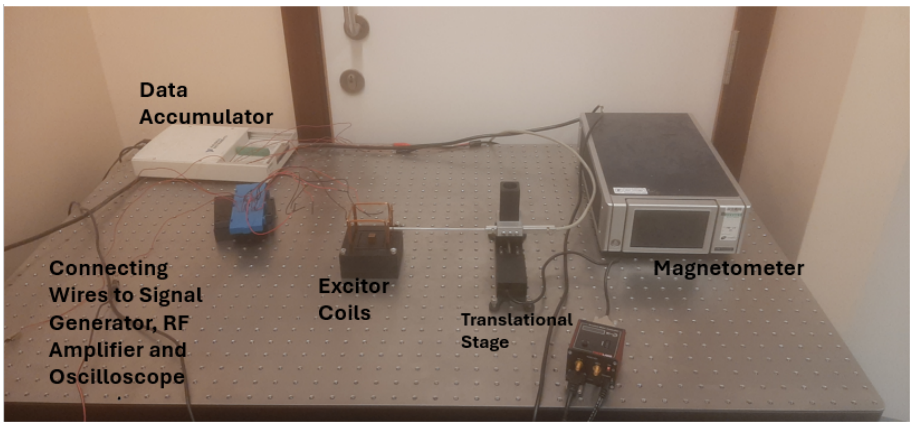

Figure 2.17: Experimental Setup

a difference measurement based imaging. Each measurement was performed for 30 seconds, and the final measurement was obtained after averaging. A triaxial vector magnetometer with a dynamic range of 0.1 μT to 30 T was used and all three field components were measured simultaneously.

2.7 Results

The region of interest of imaging is along the xy plane at a height of $z = 10$ mm. The cubical copper sample used is placed at the center of the region of interest. The region of interest is of size 40 mm $\times$40 mm. Four different spherical harmonic vector fields were implemented using the square coil setup and the measurements were made along four different lines present on the edge of the region of interest along four line segments - $y = 5$ mm, $y = 45$ mm, $x = 5$ mm and $x = 45$ mm, as showcased in Figure 2.19. Simulation results from COMSOL and experimental measurements are compared after data processing and filtering.

The noise in COMSOL simulations emerge from meshing related numerical errors. The simulations were run with a standard mesh with fine element sizes. The noise could be mitigated by customizing the mesh according to the geometry and looking for ways to modularize the simulation and perform it part by part. The numerical instabilities could also be avoided by redefining the skin depth properly according to the range of the frequency and the electromagnetic properties like conductivity and permeability used in the simulation. Further details on

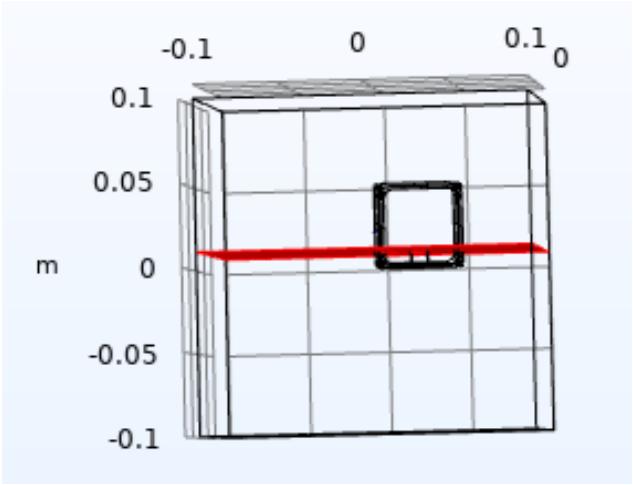

(a) Region of Interest

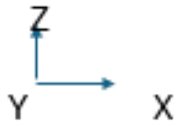

(b) Axes

Figure 2.18: Region of interest where secondary magnetic fields are measured

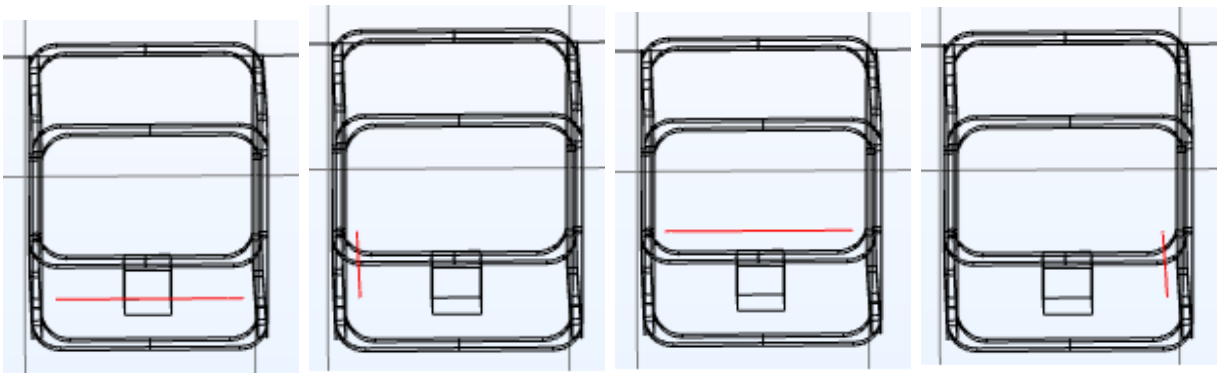

(a) Y= 5mm (b) X= 5mm (c) Y= 45mm (d) X= 45mm

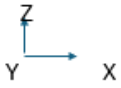

Figure 2.19: Measurement Positions

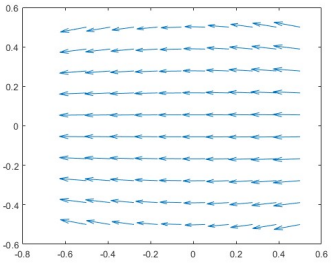

(a) Using Spherical Harmonic $n = 1, m = 1$ as excitor field

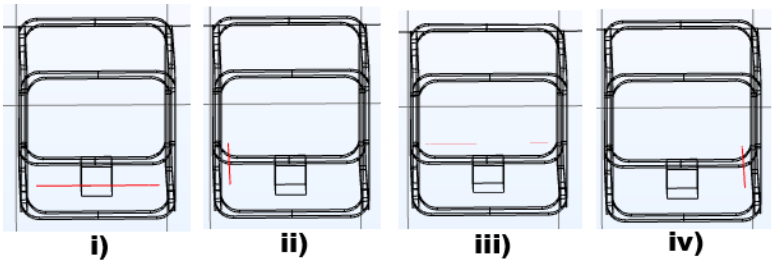

(b) i) Measuring line $Y = 5$ mm, ii) Measuring line $X = 5$ mm, iii) Measuring line $Y = 45$ mm, iv) Measuring line $X = 45$ mm, axes directions as given by Figure 2.19

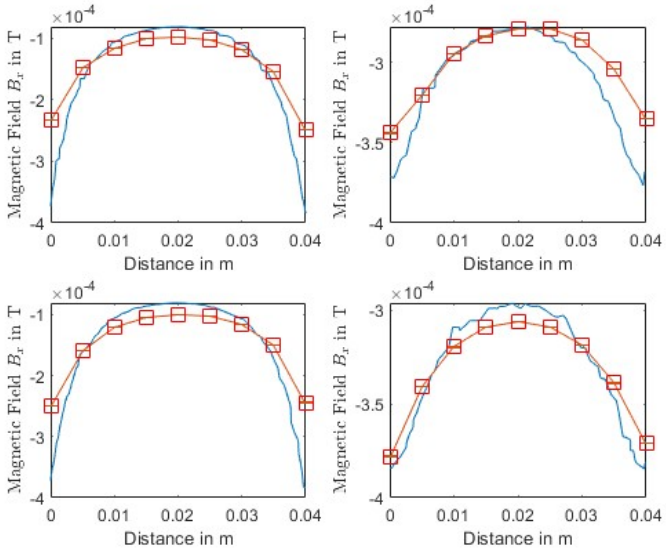

(c) Top Left: Magnetic Field B_x along $Y = 5$ mm, Top Right: Magnetic Field B_x along $X = 5$ mm, Bottom Left: Magnetic Field B_x along $Y = 45$ mm, Bottom Right: Magnetic Field B_x along $X = 45$ mm

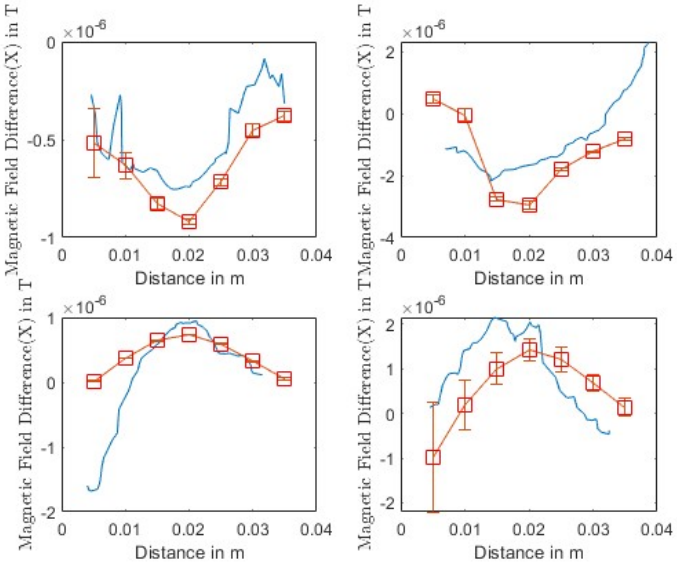

(d) Top Left: Magnetic Field Difference Bx_{diff} along $Y = 5$ mm, Top Right: Magnetic Field Difference Bx_{diff} along $X = 5$ mm, Bottom Left: Magnetic Field Difference Bx_{diff} along $Y = 45$ mm, Bottom Right: Magnetic Field Difference Bx_{diff} along $X = 45$ mm

Figure 2.20: Magnetic Field Strength and the field difference along X direction measured using X Gradient Field Vector as excitor field

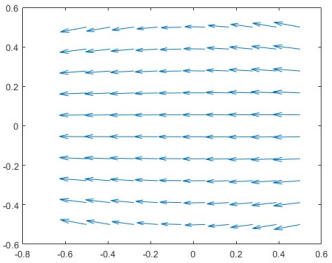

(a) Using Spherical Harmonic $n = 1, m = 1$ as excitor field

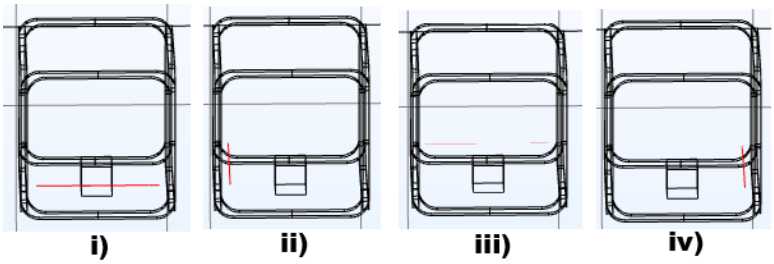

(b) i) Measuring line $Y = 5$ mm, ii) Measuring line $X = 5$ mm, iii) Measuring line $Y = 45$ mm, iv) Measuring line $X = 45$ mm, axes directions as given by Figure 2.19

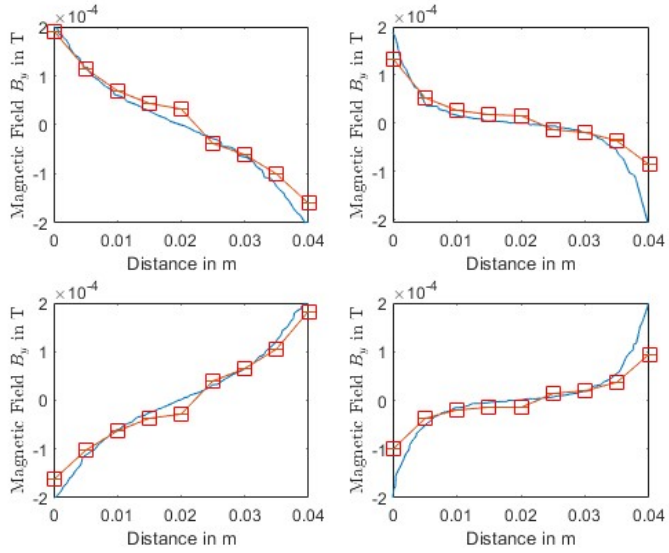

(c) Top Left: Magnetic Field B_y along $Y = 5$ mm, Top Right: Magnetic Field B_y along $X = 5$ mm, Bottom Left: Magnetic Field B_y along $Y = 45$ mm, Bottom Right: Magnetic Field B_y along $X = 45$ mm

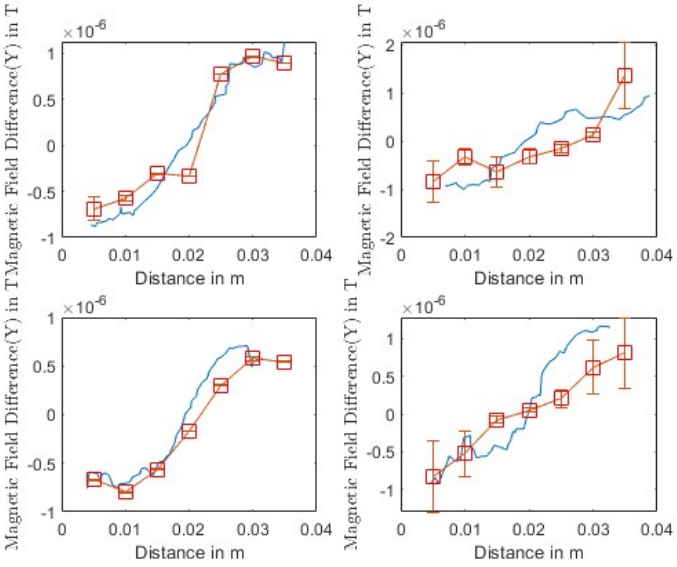

(d) Top Left: Magnetic Field Difference By_{diff} along $Y = 5$ mm, Top Right: Magnetic Field Difference By_{diff} along $X = 5$ mm, Bottom Left: Magnetic Field Difference By_{diff} along $Y = 45$ mm, Bottom Right: Magnetic Field Difference By_{diff} along $X = 45$ mm

Figure 2.21: Magnetic Field Strength and the field difference along Y direction measured using X Gradient Field Vector as excitor field

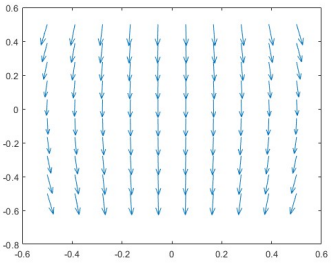

(a) Using Spherical Harmonic $n = 1, m = -1$ as excitor field

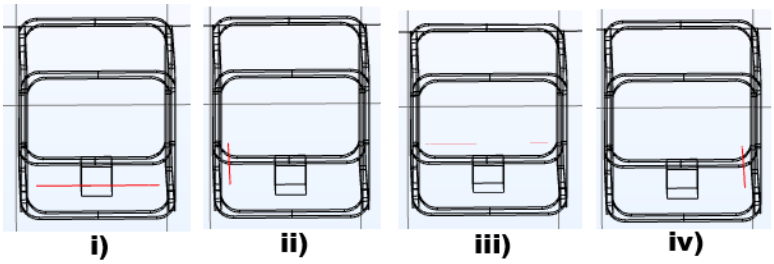

(b) i) Measuring line $Y = 5$ mm, ii) Measuring line $X = 5$ mm, iii) Measuring line $Y = 45$ mm, iv) Measuring line $X = 45$ mm, axes directions as given by Figure 2.19

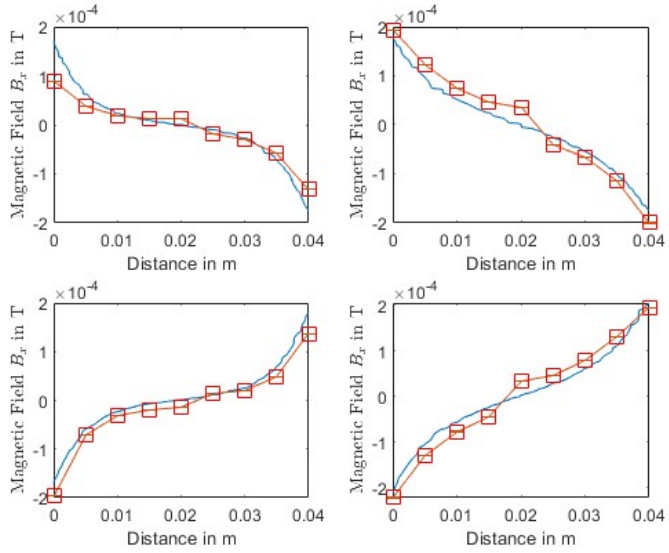

(c) Top Left: Magnetic Field B_x along $Y = 5$ mm, Top Right: Magnetic Field B_x along $X = 5$ mm, Bottom Left: Magnetic Field B_x along $Y = 45$ mm, Bottom Right: Magnetic Field B_x along $X = 45$ mm

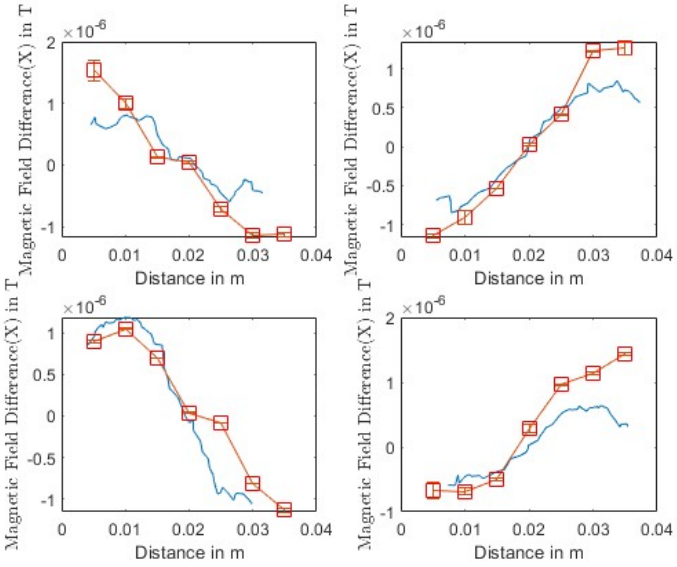

(d) Top Left: Magnetic Field Difference Bx_{diff} along $Y = 5$ mm, Top Right: Magnetic Field Difference Bx_{diff} along $X = 5$ mm, Bottom Left: Magnetic Field Difference Bx_{diff} along $Y = 45$ mm, Bottom Right: Magnetic Field Difference Bx_{diff} along $X = 45$ mm

Figure 2.22: Magnetic Field Strength and the field difference along X direction measured using Y Gradient Field Vector as excitor field

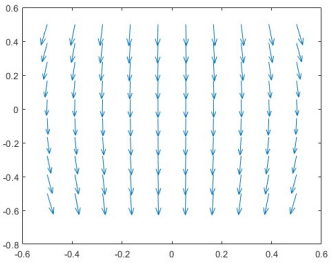

(a) Using Spherical Harmonic $n = 1, m = -1$ as excitor field

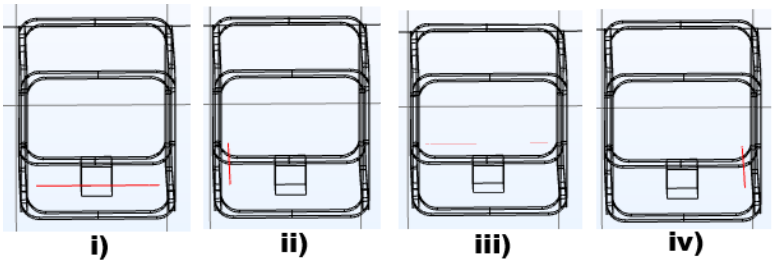

(b) i) Measuring line $Y = 5$ mm, ii) Measuring line $X = 5$ mm, iii) Measuring line $Y = 45$ mm, iv) Measuring line $X = 45$ mm, axes directions as given by Figure 2.19

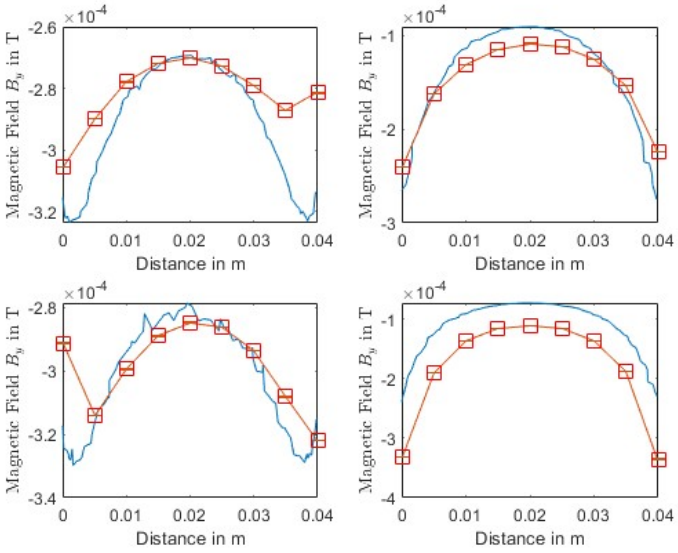

(c) Top Left: Magnetic Field B_y along $Y = 5$ mm, Top Right: Magnetic Field B_y along $X = 5$ mm, Bottom Left: Magnetic Field B_y along $Y = 45$ mm, Bottom Right: Magnetic Field B_y along $X = 45$ mm

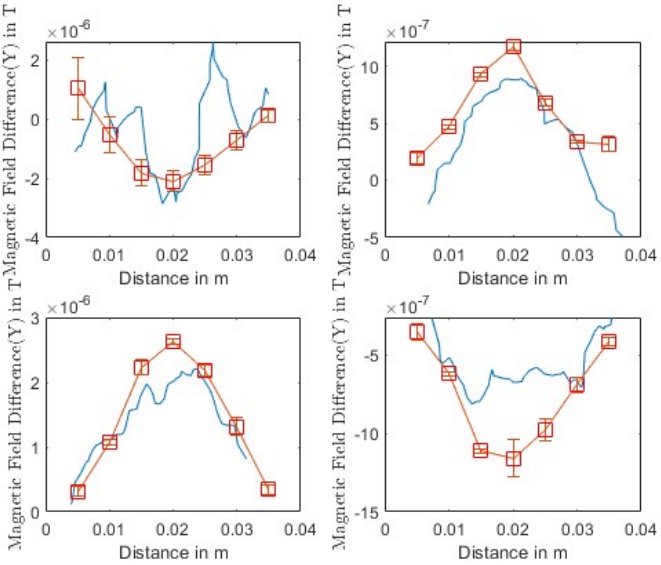

(d) Top Left: Magnetic Field Difference By_{diff} along $Y = 5$ mm, Top Right: Magnetic Field Difference By_{diff} along $X = 5$ mm, Bottom Left: Magnetic Field Difference By_{diff} along $Y = 45$ mm, Bottom Right: Magnetic Field Difference By_{diff} along $X = 45$ mm

Figure 2.23: Magnetic Field Strength and the field difference along Y direction measured using Y Gradient Field Vector as excitor field

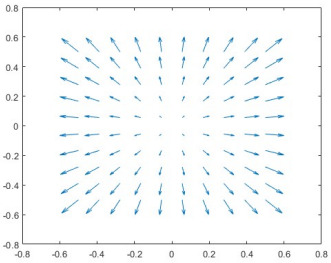

(a) Using Spherical Harmonic $n = 2, m = 0$ as excitor field

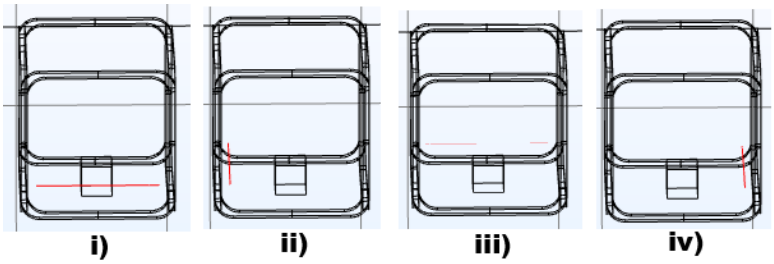

(b) i) Measuring line $Y = 5$ mm, ii) Measuring line $X = 5$ mm, iii) Measuring line $Y = 45$ mm, iv) Measuring line $X = 45$ mm, axes directions as given by Figure 2.19

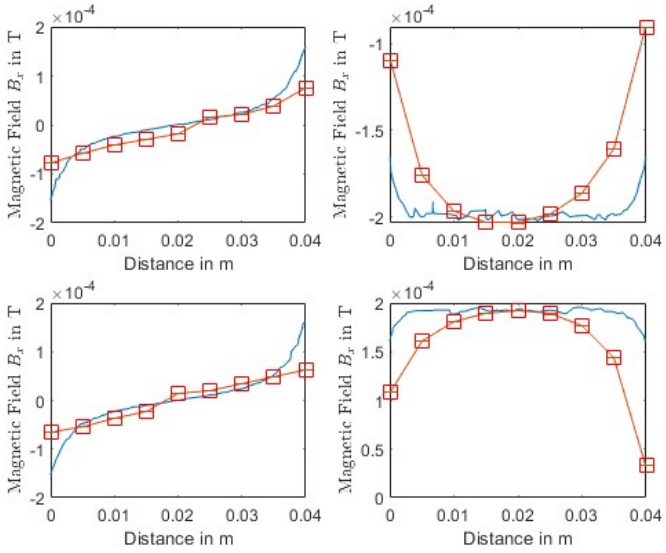

(c) Top Left: Magnetic Field B_x along $Y = 5$ mm, Top Right: Magnetic Field B_x along $X = 5$ mm, Bottom Left: Magnetic Field B_x along $Y = 45$ mm, Bottom Right: Magnetic Field B_x along $X = 45$ mm

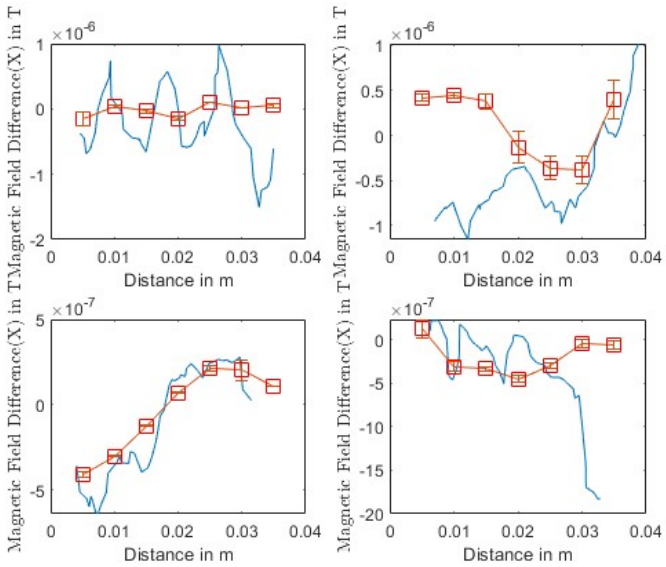

(d) Top Left: Magnetic Field Difference Bx_{diff} along $Y = 5$ mm, Top Right: Magnetic Field Difference Bx_{diff} along $X = 5$ mm, Bottom Left: Magnetic Field Difference Bx_{diff} along $Y = 45$ mm, Bottom Right: Magnetic Field Difference Bx_{diff} along $X = 45$ mm

Figure 2.24: Magnetic Field Strength and the field difference along X direction measured using SH2,0 Field Vector as excitor field

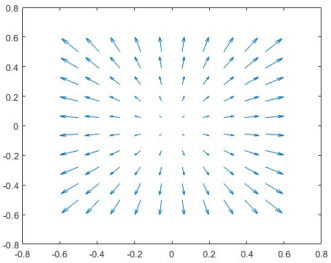

(a) Using Spherical Harmonic $n = 2, m = 0$ as excitor field

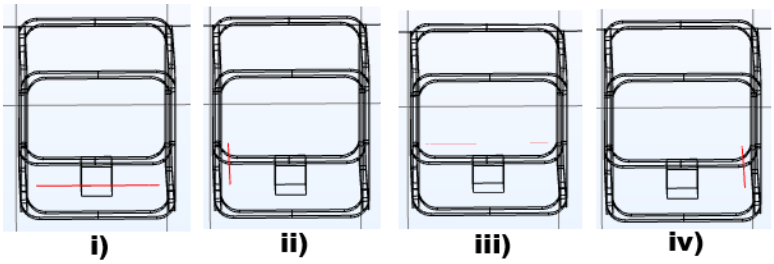

(b) i) Measuring line $Y = 5$ mm, ii) Measuring line $X = 5$ mm, iii) Measuring line $Y = 45$ mm, iv) Measuring line $X = 45$ mm, axes directions as given by Figure 2.19

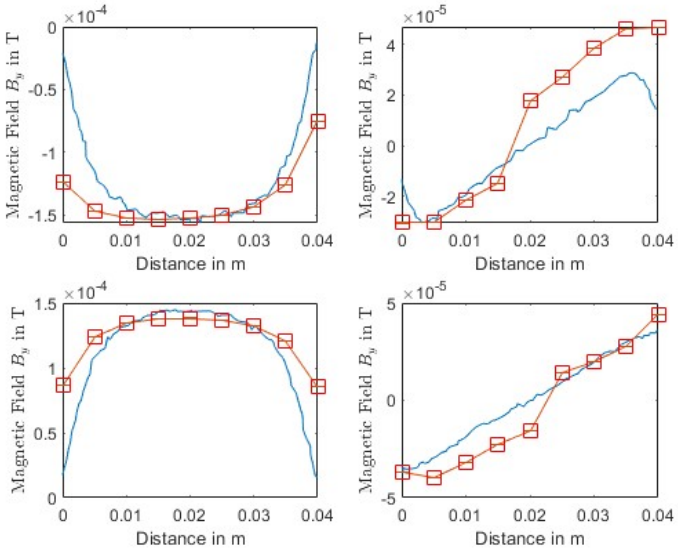

(c) Top Left: Magnetic Field B_y along $Y = 5$ mm, Top Right: Magnetic Field B_y along $X = 5$ mm, Bottom Left: Magnetic Field B_y along $Y = 45$ mm, Bottom Right: Magnetic Field B_y along $X = 45$ mm

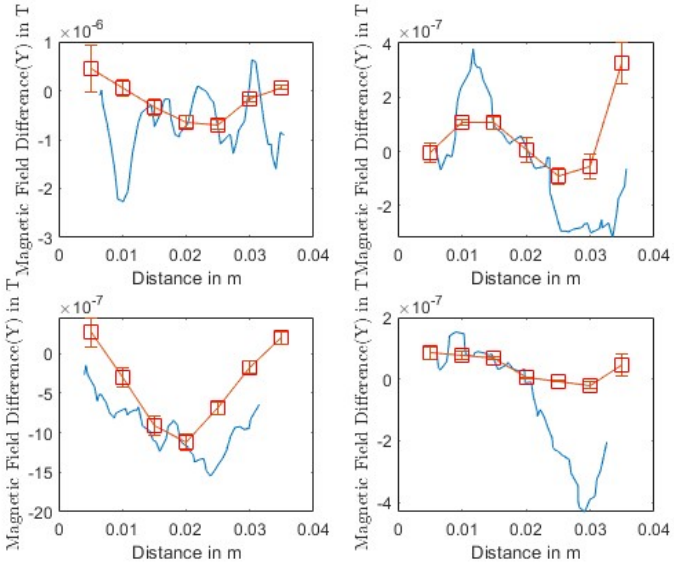

(d) Top Left: Magnetic Field Difference By_{diff} along $Y = 5$ mm, Top Right: Magnetic Field Difference By_{diff} along $X = 5$ mm, Bottom Left: Magnetic Field Difference By_{diff} along $Y = 45$ mm, Bottom Right: Magnetic Field Difference By_{diff} along $X = 45$ mm

Figure 2.25: Magnetic Field Strength and the field difference along Y direction measured using SH2,0 Field Vector as excitor field

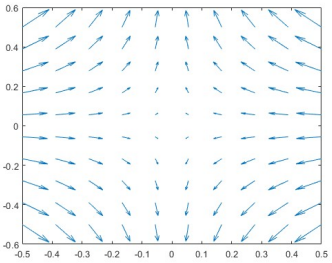

(a) Using Spherical Harmonic $n = 2, m = 2$ as excitor field

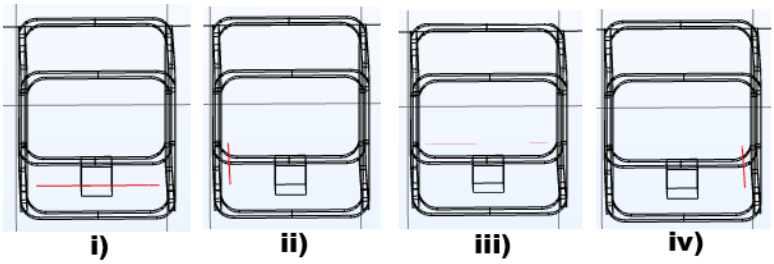

(b) i) Measuring line $Y = 5$ mm, ii) Measuring line $X = 5$ mm, iii) Measuring line $Y = 45$ mm, iv) Measuring line $X = 45$ mm, axes directions as given by Figure 2.19

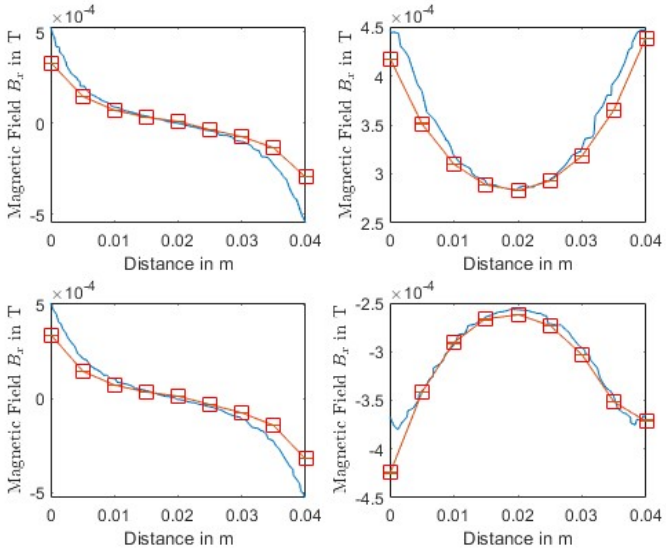

(c) Top Left: Magnetic Field B_x along $Y = 5$ mm, Top Right: Magnetic Field B_x along $X = 5$ mm, Bottom Left: Magnetic Field B_x along $Y = 45$ mm, Bottom Right: Magnetic Field B_x along $X = 45$ mm

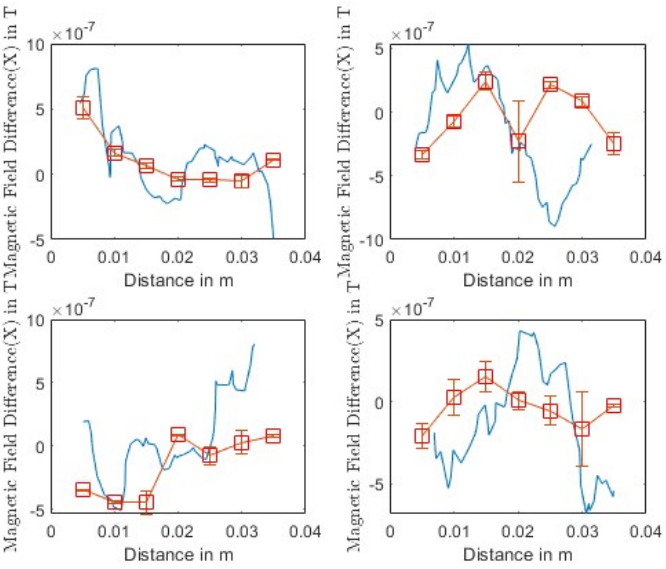

(d) Top Left: Magnetic Field Difference Bx_{diff} along $Y = 5$ mm, Top Right: Magnetic Field Difference Bx_{diff} along $X = 5$ mm, Bottom Left: Magnetic Field Difference Bx_{diff} along $Y = 45$ mm, Bottom Right: Magnetic Field Difference Bx_{diff} along $X = 45$ mm

Figure 2.26: Magnetic Field Strength and the field difference along X direction measured using SH2,2 Field Vector as excitor field

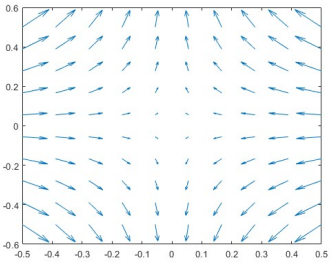

(a) Using Spherical Harmonic $n = 2, m = 2$ as excitor field

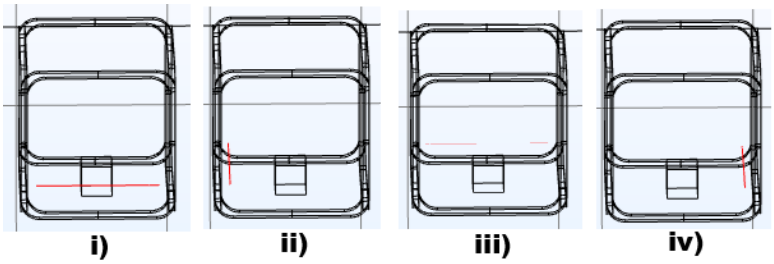

(b) i) Measuring line $Y = 5$ mm, ii) Measuring line $X = 5$ mm, iii) Measuring line $Y = 45$ mm, iv) Measuring line $X = 45$ mm, axes directions as given by Figure 2.19

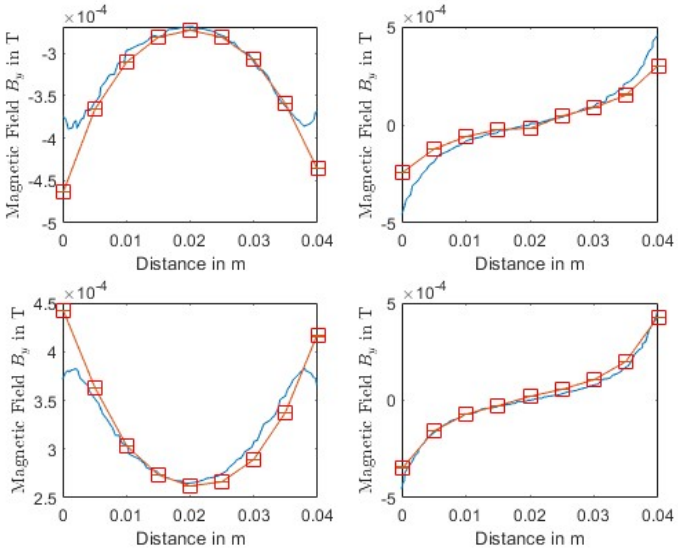

(c) Top Left: Magnetic Field B_y along $Y = 5$ mm, Top Right: Magnetic Field B_y along $X = 5$ mm, Bottom Left: Magnetic Field B_y along $Y = 45$ mm, Bottom Right: Magnetic Field B_y along $X = 45$ mm

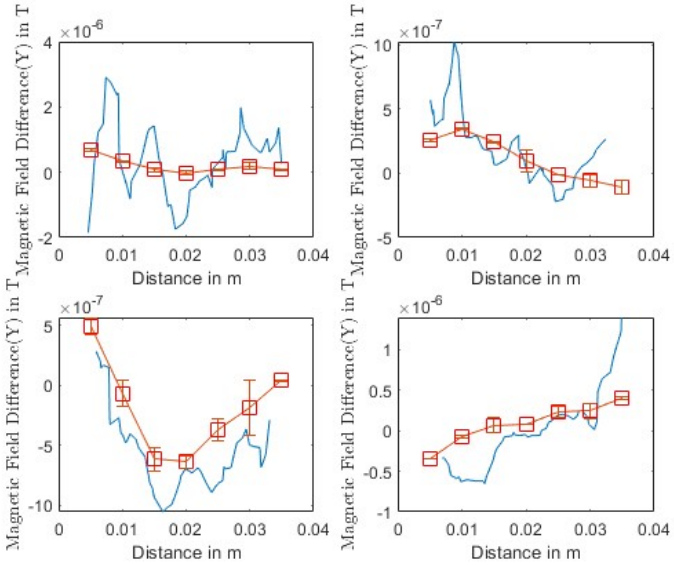

(d) Top Left: Magnetic Field Difference By_{diff} along $Y = 5$ mm, Top Right: Magnetic Field Difference By_{diff} along $X = 5$ mm, Bottom Left: Magnetic Field Difference By_{diff} along $Y = 45$ mm, Bottom Right: Magnetic Field Difference By_{diff} along $X = 45$ mm

Figure 2.27: Magnetic Field Strength and the field difference along Y direction measured using SH2,2 Field Vector as excitor field

the simulation are discussed in Chapter 3. The magnitude (RMS value) of the magnetic field was measured using the HF mode found within the Lakeshore magnetometer and the direction was determined using the DC mode of the magnetometer, as it had better provisions for measuring the magnetometer. The measurements obtained from both modes are presented in the results and hence it consists of both magnitude and direction information of the magnetic field. The standard error found from the six measurements made at each point on the measurement line is plotted as error bars in all the figures.

The three main properties that are compared for all implemented spherical harmonic fields are the magnetic field along the x axis B_x, the magnetic field along y axis B_y, and the difference between magnetic fields when the sample is placed and without the sample along all three different directions $B_{x_{withsample}} - B_{x_{withoutsample}}$, $B_{y_{withsample}} - B_{y_{withoutsample}}$ and $B_{z_{withsample}} - B_{z_{withoutsample}}$ for different spherical harmonic primary fields.

As it can be seen from Figure 2.20, the difference in magnetic field becomes greater along X when the SH11 harmonic (X Gradient) is used (Figure 2.20d), along Y when the SH1,-1 harmonic (Y Gradient) is used (Figure 2.23d) and along Z when the SH20 harmonic is used. The difference becomes greater along both X and Y axes when SH22 harmonic is used (Figures 2.26d and 2.27d). When a particular harmonic is used, the maximum difference that can be obtained along that axis is in the order of 2.5 μT (Figure 2.23d), whereas the maximum difference obtained in other cases is approximately 1 μT (Figures 2.20d, 2.24d, 2.25d, 2.26d and 2.27d). It can also be found that the differences found in the secondary magnetic fields when SH2,0 and SH2,2 harmonics are applied are on the order of -0.5 μT to 0.5 μT.

It can be observed that the use of spherical harmonic primary field patterns induce unique secondary magnetic fields, which, when in used in the inverse problem of Magnetic Induction Tomography, help in obtaining better and unique reconstructions of conductivity. The uniqueness helps target different parts of the region of interest, when we use these orthonormal, unique harmonic patterns without changing the position of the sample and its characteristics, we are able to obtain different and unique magnetic field difference patterns that help us image the region better. Since Magnetic Induction Tomography is an inverse problem based upon the inhomogeneous Helmholtz equation with the eddy current induced secondary magnetic fields obeying the Helmholtz equation of dispersion, the idea of unique fields makes for efficient reconstructions.

2.8 Image Reconstruction

The reconstruction of images in Magnetic Induction Tomography is directly related to the inverse problem and its solution. An inverse problem involves calculating the input variables based on recorded output data. In the case of Magnetic Induction Tomography, we seek to calculate the conductivity distribution from the observed secondary magnetic fields induced due to eddy currents. It consists of two parts - formulation of a sensitivity matrix and application of a corresponding inverse algorithm to arrive at the corresponding conductivity distribution. We have utilized two inverse algorithms for reconstruction of images - 1) Linear Back Projection and 2) Linear Regression using Tikhonov Regularization.

The orthogonality and the linear independence that the sensitivity matrix offers play a crucial role in reconstruction of conductivity. An orthogonal matrix is a matrix whose transpose is the same as its inverse. By using a spherical harmonic primary field, we try to exploit the

orthogonality property of the sensitivity matrix and use the transpose in the place of the inverse of the sensitivity matrix.

2.8.1 Construction of Sensitivity Matrices

A sensitivity matrix maps the relationship between internal input variables and external observed data and is given by the Jacobian matrix of the system. In the case of Magnetic Induction Tomography, the sensitivity matrix determines the change in relationship between the measured electromagnetic quantity and the physical parameters changed within the system like conductivity, permeability and permittivity. The Jacobian matrix, S, determines the spatial variation of conductivity.

$$\sigma = S^{-1} \cdot \vec{B_e} \tag{2.51}$$

$$\Delta\sigma = S^{-1} \cdot \Delta\vec{B_e} \tag{2.52}$$

$$S = \begin{bmatrix} \frac{\partial B_1}{\partial \sigma_1} & \frac{\partial B_1}{\partial \sigma_n} \\ \dots & \dots \\ \frac{\partial B_n}{\partial \sigma_1} & \frac{\partial B_n}{\partial \sigma_n} \end{bmatrix} \tag{2.53}$$

In multiple coil-based different approaches taken in Magnetic Induction Tomography so far, the point sensitivity at every point of space (the rate of change of secondary magnetic field with respect to conductivity) is determined by the dot product of characteristic vectors between the excitor and receiver coils. The characteristic vectors could be electric fields, magnetic fields or magnetic vector potentials and the sensitivity matrix is often determined through a FEM (Finite Element Method) simulation. Some of the known formulations of sensitivity matrix from the literature are [7][73][74][75].

$$S = \frac{\nu}{(I_1 I_2)} * (\vec{E_1} \cdot \vec{E_2}) \tag{2.54}$$

$$S = \frac{-j\omega}{I_1 I_2} \int \vec{H_1} \cdot \vec{H_2} dv \tag{2.55}$$

$$S = \frac{\omega}{I_1 I_2} * (\vec{A_1} \cdot \vec{A_2}) \int N_e . N_e^T dv \tag{2.56}$$

$$S = k\vec{B_1} \cdot \vec{B_2} \tag{2.57}$$

The sensitivity formulations are described in detail in Chapter 1 and Section 1.5.2. Equations 2.53, 2.54, 2.55 and 2.56 are modified matrix forms of equations 1.13, 1.14, 1.15 and 1.16. $\vec{E_1}$ and $\vec{E_2}$ are the electric fields, $\vec{H_1}$ and $\vec{H_2}$ are the magnetic fields fields, $\vec{A_1}$ and $\vec{A_2}$ are the magnetic vector potentials and I_1 and I_2 are the electric currents of primary excitor coils and secondary magnetic field sensors respectively. ν and ω indicate the frequency of the MIT system.

These are helpful when the detectors used are RF pickup coils. A sensitivity formulation that is compatible with the use of magnetometers in MIT is developed. Irrespective of the physical process by which the magnetometer measures the field (a Hall probe, a fluxgate magnetometer, an Optically Pumped Atomic Magnetometer or a SQUID), this formulation of sensitivity could be used to reconstruct images. The current sensitivity formulation is modified to reflect the changing nature of magnetic field sensing.

In order to exploit the property of linear independence and orthogonality of spherical harmonics, the sensitivity matrix is formulated using the magnetic vector potential of the excitor coils. The sensitivity matrix is calculated as a complex form of the magnetic vector potentials along the x and y directions. The excitor current and the unit current at sensing element formulation is considered as per Equation 2.56 and Section 1.5.2 from Chapter 1. The magnetic vector potential from the excitor coils within the region of interest, as mentioned in Equation 2.33, is calculated using

$$\vec{B}(r) = \nabla \times \vec{A}(r) \tag{2.58}$$

$$\vec{A}(r) = \frac{\mu}{4\pi} \iiint \frac{\vec{J_s}(r') \times |\vec{r} - \vec{r'}|}{|\vec{r} - \vec{r'}|^2} d^2r' \tag{2.59}$$

The calculation of magnetic vector potential at every point along the region of interest and discretizing it gives the sensitivity matrix.

$$S = A_x + iA_y \tag{2.60}$$

where $\vec{A_x}$ and $\vec{A_y}$ are the magnetic vector potentials along the x and y directions respectively.

The absolute forms of complex sensitivity matrices from the four different spherical harmonics are presented in Figure 2.28. They are a mapping of the magnetic vector potential of the region of interest. One of the core features and the significance of using spherical harmonic orthogonal magnetic fields is having orthogonal, linearly independent and diagnolazible sensitivity matrices that make inversion efficient. It can be seen that the matrices are linearly independent, as the rank of the sensitivity matrices equals their size. These matrices are of the size 27 $\times$ 27, with the rank 27.

Linear independence is a prerequisite condition for a matrix to be orthogonal. Linear independence can be observed in a matrix when it has no all zero rows or columns (all the elements of a particular row or column or trivial) or when no row or column is a direct linear multiple of any other row or column. It can be observed by looking at the distribution of elements within the sensitivity matrix.

The resultant products of sensitivity matrices with their transposes are showcased in Figure 2.29 in order to demonstrate and verify their orthogonality. As explained in Section 2.2, an orthogonal matrix is a matrix whose inverse equals its transpose. Figure 2.29 presents products of two different sensitivity matrices with their transposes. It can be seen from the figure that the matrix, with magnetic fields with greater fidelity and more robust magnetic vector potential calculations, would turn perfectly orthogonal. The presented matrix products have also been normalized, as it can be seen from Figure 2.29.

The product of an orthogonal matrix with its transpose would be a perfect diagonal identity matrix. As it can be seen from Figure 2.29, the products obtained from the sensitivity matrices aren't perfectly diagonal matrices. A comparison with a perfect harmonic based identity matrix can help realize how much more should the excitor magnetic fields be designed so that they are homogeneous spherical harmonic magnetic fields.

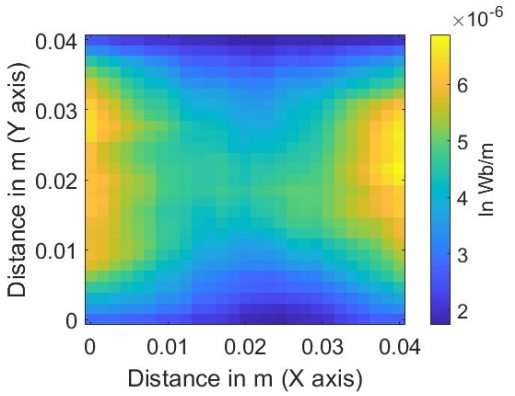

(a) Spherical Harmonic $n = 1, m = 1$ Sensitivity Matrix

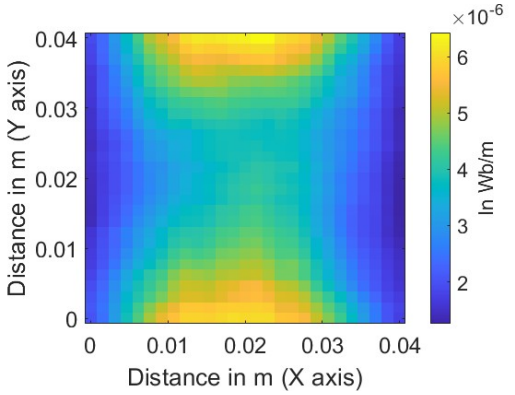

(b) Spherical Harmonic $n = 1, m = -1$ Sensitivity Matrix

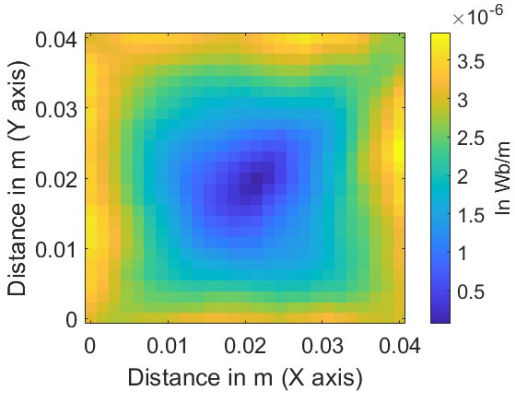

(c) Spherical Harmonic $n = 2, m = 0$ Sensitivity Matrix

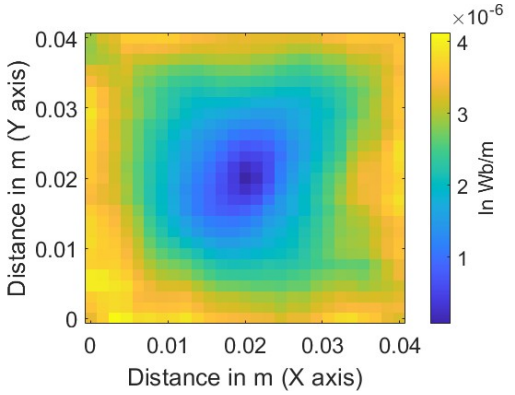

(d) Spherical Harmonic $n = 2, m = 2$ Sensitivity Matrix

Figure 2.28: Sensitivity Matrices based on Magnetic Vector Potentials of Spherical Harmonic Vector Magnetic Fields

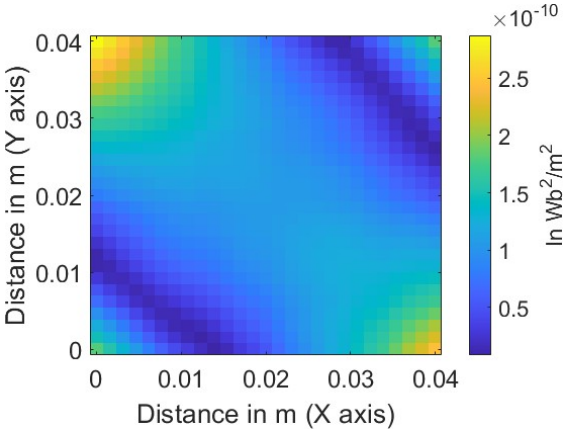

(a) $A_{20} * A'_{20}$

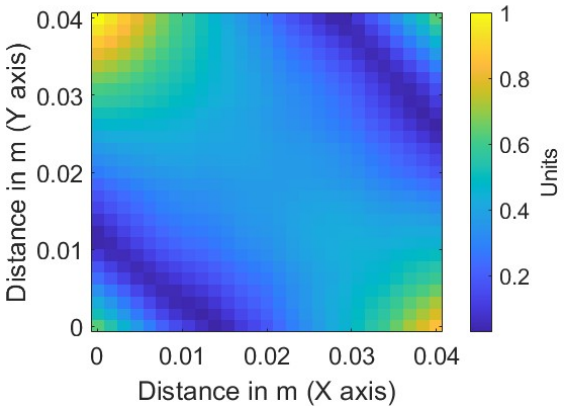

(b) Normalized $A_{20} * A'_{20}$

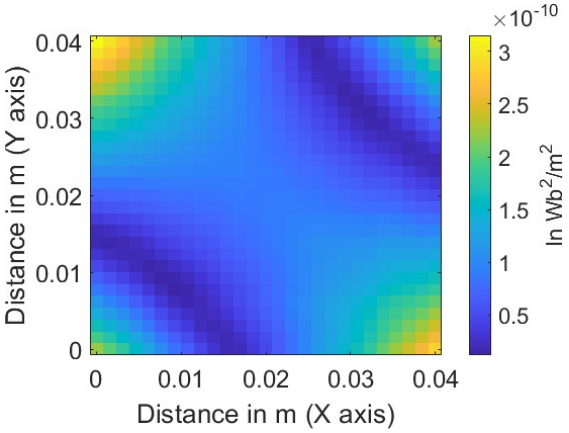

(c) $A'_{20} * A_{20}$

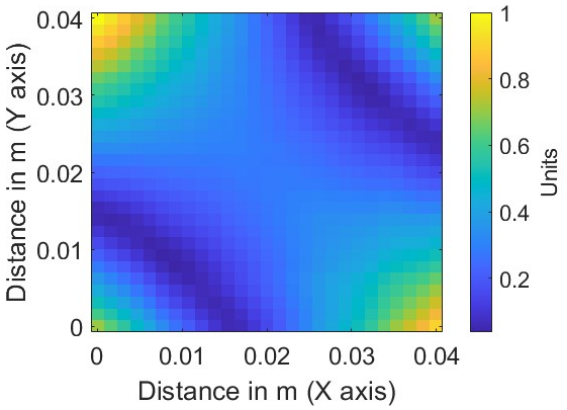

(d) Normalized $A_{20} * A'_{20}$

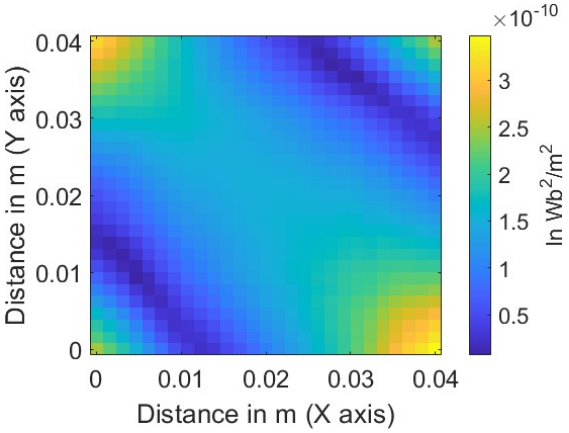

(e) $A_{22} * A'_{22}$

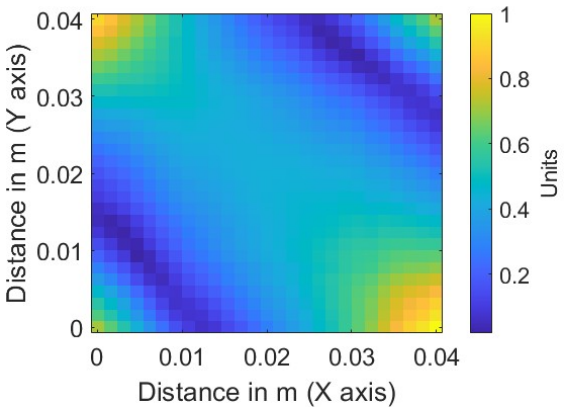

(f) Normalized $A_{22} * A'_{22}$

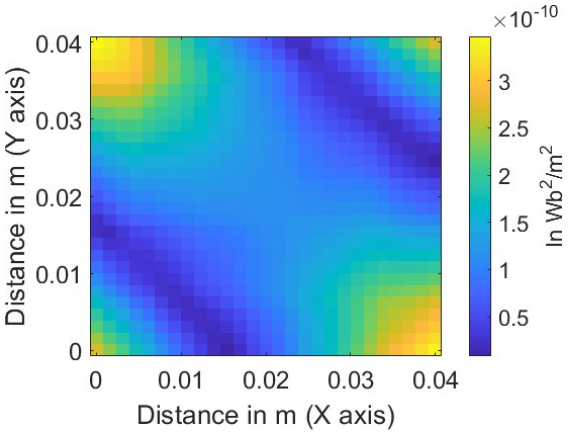

(g) $A'_{20} * A_{20}$

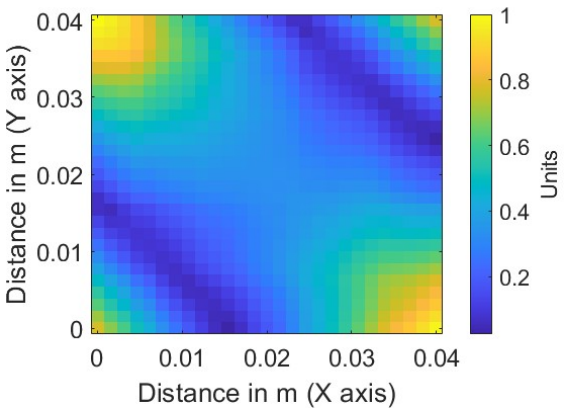

(h) Normalized $A'_{20} * A_{20}$

Figure 2.29: Products of sensitivity matrices

2.8.2 Application of Inverse Algorithms

The prime idea behind using vector spherical harmonic magnetic fields as excitor fields is that the orthogonality property that they share will make the process of inversion very effective and pose an efficient method of tackling the inversion problem that Magnetic Induction Tomography [106] offers. Inverse problems generally consist of erroneous observations which are represented by $\epsilon^{'}$ in Equation 2.61.

$$\sigma = S^{-1}B_e + \epsilon^{'} \tag{2.61}$$

The two fundamental algorithms that help take complete advantage of the orthogonality property are 1) Linear Backprojection [107] and 2) Linear Regression. These two algorithms are used to arrive at the final reconstructed images.

Linear Backprojection

The fundamental idea of an orthogonal matrix is that the inverse of the matrix is simply its transpose. Linear Backprojection is a method of reconstruction where the inverse of the sensitivity matrix is directly replaced by its transpose and normalized to recover the conductivity distribution. And since sensitivity matrices are constructed to be orthogonal, linear backprojection can be an efficient and a quick methodology to begin solving the inverse problem, arriving at their required reconstruction via electrical conductivity.

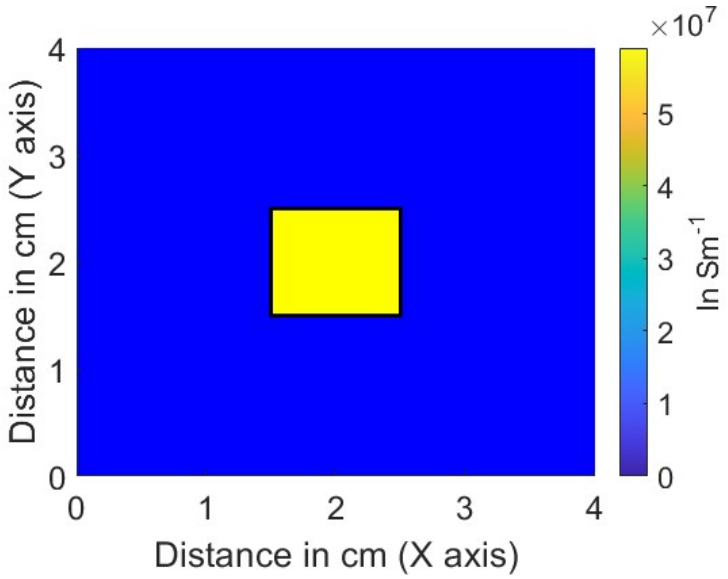

Figure 2.30: Ideal Target Image

$$\sigma = S^{-1} \cdot B_e \tag{2.62}$$

In order to obtain the final image reconstruction, we perform a normalization [108],

$$\sigma_\lambda = \frac{(S^T \cdot B_e)}{(S^T \cdot B_\lambda)} \tag{2.63}$$

where $B_\lambda = [1, 1, ..., 1]$, a matrix of ones and σ_λ refers to the finally derived conductivity distribution after applying linear backprojection.

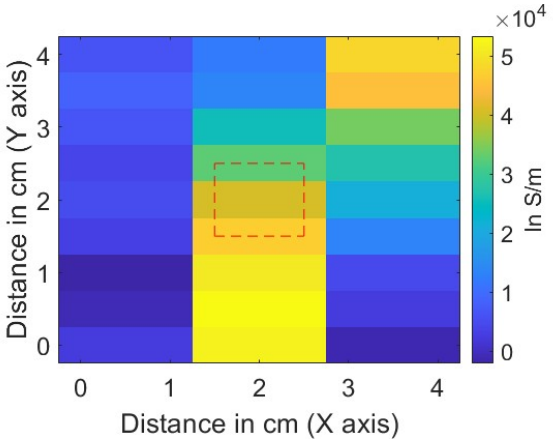

(a) X Gradient

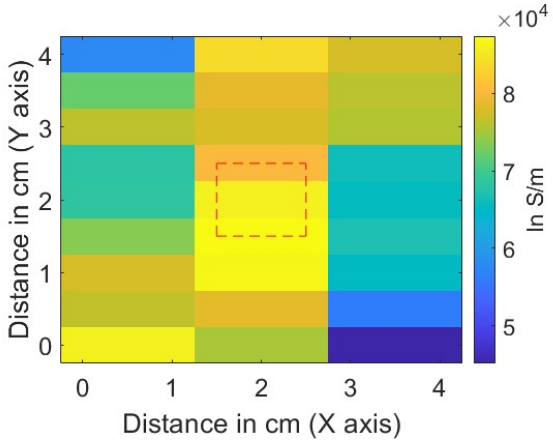

(b) Y Gradient

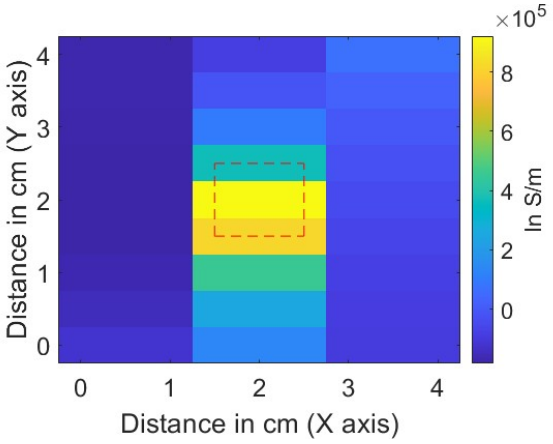

(c) SH 2,0

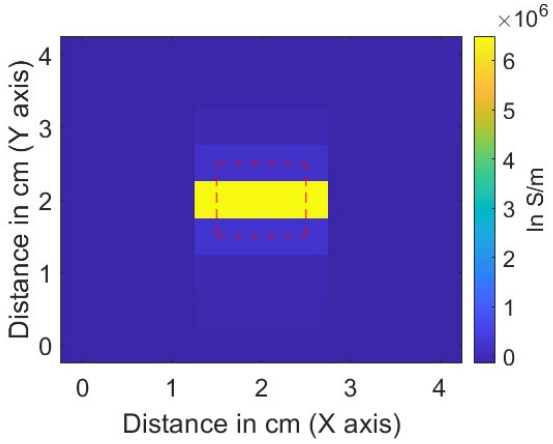

(d) SH 2,2

Figure 2.31: Images reconstructed through Linear Back Projection (The red square in the center indicates the ideal target image)

Linear Regression with Tikhonov Regularization

Linear regression is a statistical method used to draw the relationship between two variables based on recorded instances of observation. It is widely used in curve fitting and machine learning algorithms and provides with a great tool for solving inverse problems, as it tries to minimize the least squares error calculated through the Euclidean distance.

Tikhonov Regularization [109], also known as Least Squares Regression or Ridge Regression, is used in inversion problems to avoid bias and variance based errors and to arrive at the best possible fitting of data. It is performed using an identity matrix and a regularization parameter calculated using gradient descent. In order to arrive at the final conductivity reconstruction, it is normalized in a process similar to linear backprojection.

In Linear Regression, the conductivity distribution is given by

$$\sigma = (S^T S)^{-1} S^T B_e \tag{2.64}$$

The key challenge of Tikhonov Regularization is finding the regularization parameter. Tikhonov Regularization follows the process of using an identity matrix with a regularization parameter as a way to improve the condition number of the sensitivity matrix. It uses an L-curve method to arrive at the regularization parameter λ. The L-curve method is a heuristic method for finding the regularization parameter λ. It is often arrived at by using a logarithmic plot of the residual norm with the solution norm. The plot often resembles the letter L and hence it is called the L-curve method. λ is chosen in such a way that it falls in the curving region of the plot. The used regularization parameters for the regression are listed below. The regularization parameters are chosen with the help of the L-curve used in regularization in Tikhonov regularization based inverse problems.

Spherical Harmonic	Regularization Parameter
SH 1,1	1×10^{-15}
SH 1,-1	1×10^{-15}
SH 2,0	1×10^{-10}
SH 2,2	1×10^{-9}

After applying the Tikhonov Regularization parameter,

$$\sigma = (S^T S + \lambda I)^{-1} S^T B_e \tag{2.65}$$

After normalization, the final conductivity distribution is determined using,

$$\sigma = \frac{(S^T S + \lambda I)^{-1} S^T B_e}{(S^T S + \lambda I)^{-1} S^T B_\lambda} \tag{2.66}$$

Once the images are reconstructed using both Linear Backprojection and Linear Regression with Tikhonov Regularization, the rearrangement or the reshaping of the reconstructed conductivities at each and every point of reconstruction provides us with the final image.

2.9 Results and Discussion

The use of spherical harmonic based excitor fields and different inversion algorithms provide different sets of reconstructions, as can be observed from Sections 2.8.1 and 2.8.2. Multiple possible parameters can be used to arrive at the final reconstruction.

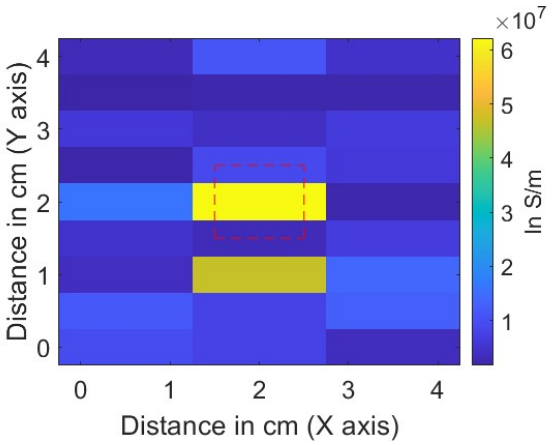

(a) X Gradient

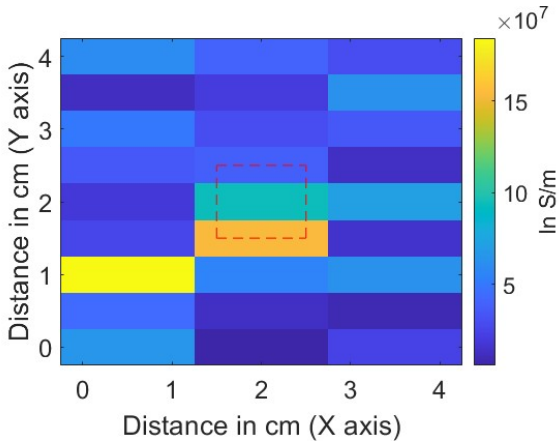

(b) Y Gradient

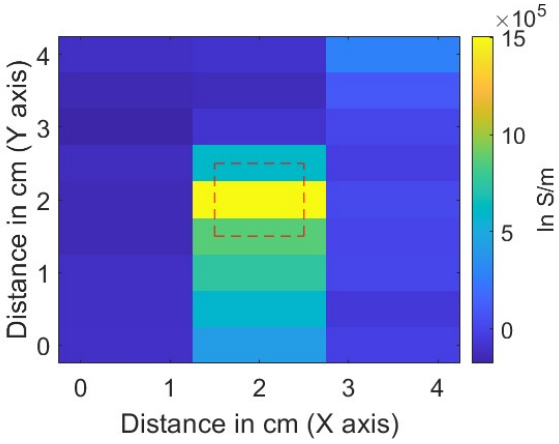

(c) SH 2,0

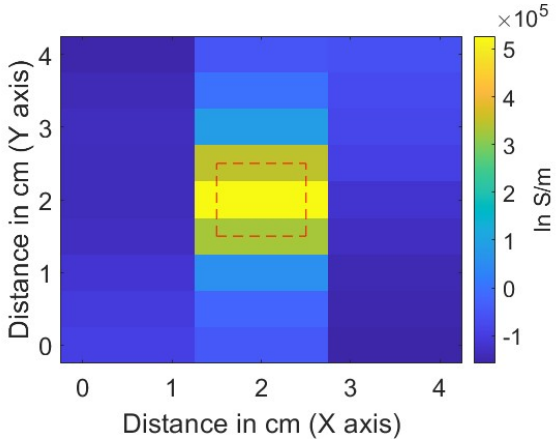

(d) SH 2,2

Figure 2.32: Images reconstructed through Tikhonov Regularization (The red square in the center indicates the ideal target image)

The orthogonality of a matrix is determined by how close the product of the matrix and its transpose are to the identity matrix. It is found that SH20 and SH22 harmonics perform better in terms of experimentally building an orthogonal matrix.

The two key parameters that have been considered to weight images and arrive at the final conductivity distribution are RMS Error between the measured and predicted magnetic fields and condition number of the sensitivity matrix. The RMS error is a measure of how accurate the reconstructed measurements are. The most direct way of calculating RMS Error is by using

$$RMS_E = B_e - S * \sigma \tag{2.67}$$

The 2-norm term associated with the RMS error is calculated using

$$RMS_e = \sqrt{\frac{1}{n}\sum_{i=1}^{n} |Be_i - (S * \sigma)_i|^2} \tag{2.68}$$

The RMS error tells us on an average how close are the predicted or reconstructed measurements from the inverse problems to the measured magnetic fields. The RMS error measures the average of square of predicted or reconstructed errors, in this case, how close the reconstructed product of the sensitivity matrix and the conductivity is to the measured secondary magnetic fields. The closer RMS error is to zero, it can be said that the reconstructions are closer to the measurements. It can be considered an average error bar to the conductivity predictions made. Figure 2.33 presents the comparison between reconstructed secondary magnetic field values and measured secondary magnetic field values. The magnetic field measurements were made at 32 locations along the four measuring lines (at eight different positions along each line) showcased in Figure 2.19. They are represented in X axis, while the field values are showcased in Y axis.

The condition number is determined by how stable the sensitivity matrix is and how immune it is to external numerical errors that tend to plague inversion problems. It is a measure of how much the matrix is affected when the input vector changes, when subject to external errors. In general, the more orthogonal the matrix is, the lower its condition number and the lower the condition number is, the more stable the sensitivity matrix tends to be. One of the key goals of solving an inverse problem is ensuring that the matrix that is sought to be inverted remains well-conditioned.

RMS Error		
Spherical Harmonic	Linear Backprojection	Linear Regression (Tikhonov Regularization)
SH 1,1	1.27×10^{-6}	2.91×10^{-7}
SH 1,-1	1.58×10^{-6}	3.21×10^{-7}
SH 2,0	4.98×10^{-7}	4.52×10^{-7}
SH 2,2	3.04×10^{-7}	2.80×10^{-7}

The condition numbers of sensitivity matrices formed using four different spherical matrices are presented below. In comparison, condition numbers of orthogonal matrices formed using Legendre polynomials and other special functions are on the order of 10^8.

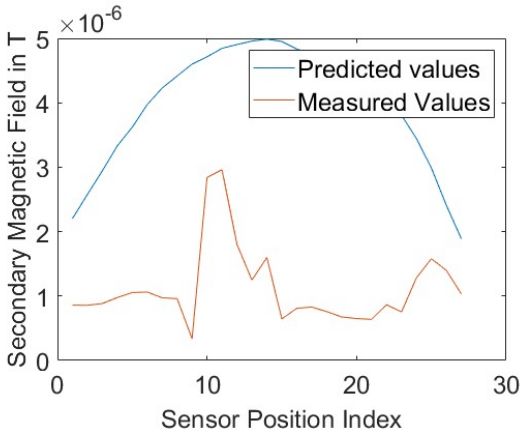

(a) Comparison between reconstructed and measured values of secondary magnetic field from Linear Backprojection

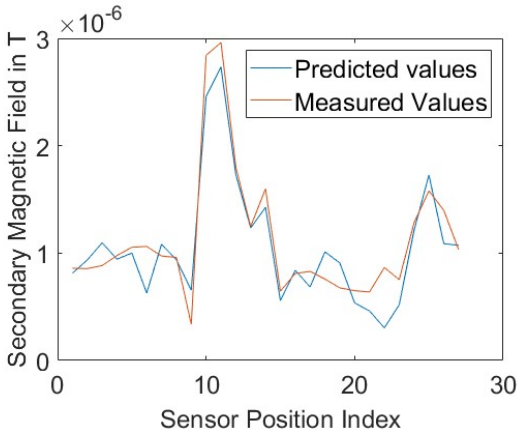

(b) Comparison between reconstructed and measured values of secondary magnetic field from Tikhonov Regularization

Figure 2.33: Comparison between reconstructed and measured values of secondary magnetic field using X Gradient as excitor field

Spherical Harmonic	Condition Number
SH 1,1	6.316×10^4
SH 1,-1	7.909×10^4
SH 2,0	1.110×10^5
SH 2,2	9.734×10^4

Figures 2.31 and 2.32 present the final image reconstructions obtained from spherical harmonic excitor magnetic fields using two algorithms. It can be seen from Figures 2.31 and 2.32 and the two tables of RMS Error and condition number that the SH22 harmonic is efficient and accurate in image reconstruction. The lower the RMS error is, the more accurate the reconstruction is. The lower the condition number is, the easier the inversion is. It can be seen from Figures 2.31 and 2.32 that harmonics SH2,0 and SH2,2 are more accurate than SH1,1 and SH1,-1 in image reconstruction given their lower RMS error, but they are also more time consuming to invert as their condition number is higher than SH1,1 and SH1,-1 harmonics. The algorithm chosen also plays a key role in the final reconstructed image which can also be observed from Figures 2.31 and 2.32. Thus, multiple factors like the choice of the algorithm and the pattern of the spherical harmonic chosen determine the final reconstructed image and how accurate it can be.

In terms of the speed of algorithm execution, matrix inversion and hence linear backprojection has a computational complexity of $O(N^2)$, while the computational complexity of using linear regression when the sensitivity matrix to be inverted is square (as in this case) is $O(N^3)$. Tikhonov Regularization and solving for the regularization parameter will add to the complexity of the inversion problem. So, if the speed and the computational cost of the two algorithms are to be considered, Linear Backprojection is a quicker method of execution while Regression using Tikhonov Regularization is more computationally intensive and hence takes greater time.

In general, the use of these two different algorithms can be summarized, in the following way. Linear Backprojection provides the conductivity distribution and solves the inverse problem quickly with a lesser use of computational resources at the cost of a greater RMS error. Regularized Linear Regression reduces the RMS error greatly and solves the inversion problem

with better accuracy, while it is computationally more demanding and takes time to solve. The orthogonality of the sensitivity matrices built based on the vector spherical harmonic fields help reduce the RMS error and improve numerical stability, helping the algorithms converge upon the final conductivity distribution quickly. It also improves the inversion problem to go from ill-posed to well-posed with better stability.

The main advantage of using spherical harmonic based vector magnetic fields as excitor fields lies in their orthogonality. From the reconstructed images, it is possible to obtain a linear combination of images with images being weighted depending the harmonic excitor field that they were obtained from. It provides us with an idea of how Magnetic Induction Tomography using spherical harmonics can be used to obtain an overall view of the region of interest that is sought to be imaged.

Producing perfect spherical harmonic magnetic fields within the required region of interest is a challenging task. The creation of homogeneous and uniform spherical harmonic magnetic fields would produce perfectly orthogonal sensitivity matrices. The square shaped four coil system is a sample system that seeks to produce perfect harmonics, but the arrangement, the shape and the structure of the four coil setup make it difficult to provide perfectly homogeneous spherical harmonic magnetic fields as excitor fields, with the magnetic fields varying with greater degree towards the edges of the four coil setup. The homogeneity of the spherical harmonic magnetic fields could be improved by increasing the number of coils, changing the ratio of excitor currents supplied to the coils, altering the shape of coils that are more conducive to generating spherical harmonic magnetic fields and designing specifically shaped coils that could generate specific target fields as excitor fields.

It is possible to explore the use of multiple different algorithms in inverting an ill-conditioned sensitivity matrix. Some of the potential options to be explored includes various regression methods, singular value decomposition based methods, convolutional neural networks and denoising based methods. Radon transformations are also helpful when it comes to image reconstruction. The use of spherical harmonics in inversion problems makes it possible to explore further such inversion methods with the element of orthogonality added into them.

2.10 Conclusion

The use of spherical harmonics as excitor fields, their role in construction of orthogonal, linearly independent sensitivity matrices and solving inversion problems are demonstrated. It paves the way for better image reconstruction in Magnetic Induction Tomography and the potential use for quantum sensors like Optically Pumped Magnetometers in Magnetic Induction Tomography. Other inversion algorithms like SART (Simultaneous Algebraic Reconstruction Technique) and iterative reconstruction algorithms could also be potentially investigated for better image reconstruction in Magnetic Induction Tomography.

Chapter 3

Computational Simulations, Experimental Methods and Phase Based Imaging using Spherical Harmonic Magnetic Vector Fields in Magnetic Induction Tomography

3.1 Overview

The chapter focuses on the phase effects of spherical harmonic magnetic fields in Magnetic Induction Tomography. Phase plays a crucial role in MIT theory as the secondary magnetic fields create a phase difference. This chapter explores the changes caused in phase and phase difference between the primary and secondary magnetic fields when spherical harmonic magnetic fields are applied.

It explains the computational simulations undertaken to calculate the phase difference using COMSOL modeling and further elaborates into the experimental setup required to measure the phase difference between the primary and secondary fields. It presents the results of the experiment and how the measured phase change varies when the spherical harmonic based excitor fields are changed. It also discusses the results and highlights how the measured phase differences are different in nature compared to secondary, eddy current based differences in magnetic field magnitude due to a sample.

The chapter continues with the experimental methods used to measure the phase difference of the secondary magnetic fields induced by the eddy current and concludes with image reconstructions based on Inverse Radon transforms from both magnetic field differences and phase differences. It ends with a discussion on how phase based reconstructions in Magnetic Induction Tomography can be improved.

3.2 Theory

In general, reconstruction of images in Magnetic Induction Tomography is based on secondary magnetic field differences as showcased in Chapter 2. But, in quite a few other approaches, it is possible to use phase difference ϕ as a primary measure of reconstruction.

$$\Delta\sigma = S^{-1}\Delta\phi \tag{3.1}$$

$$\sigma = S^{-1}\phi \tag{3.2}$$

where σ is the electrical conductivity and A is the sensitivity matrix.

The difference in phase is directly proportional to a physical electromagnetic quantity of the sample like conductivity, permeability or permittivity. Hence, measuring phase differences and using them as a way towards reconstructing images would provide much more comprehensive information about the region of interest.

The use of spherical harmonics creates a unique set of solutions in Magnetic Induction Tomography, as seen from Chapter 2. The induced secondary magnetic field caused due to the eddy currents within the sample temporally lags the applied primary field and that causes the phase difference detected in the sensor. The in-phase and quadrature phase components of the secondary magnetic field detected can help with image reconstruction.

In some ways of modeling the physics of Magnetic Induction Tomography, the secondary magnetic field is approximated as a series of sums of in phase and quadrature (out of phase) components. A complete theoretical exploration of in phase and quadrature phase components of the magnetic field components can be found in the literature [95]. As found in Section 2.8.1, it is found that the magnetic vector potential has a real component and an imaginary component,

$$S = A_x + iA_y \tag{3.3}$$

where A_x is the magnetic vector potential along the x direction and A_y is the magnetic vector potential along the y direction.

Based on the theoretical modeling, the real component and the imaginary component of the magnetic vector potential can be modeled separately, used to calculate the magnetic field components. The phase difference between the two magnetic field components provides information about the region of interest and its electromagnetic properties. According to the theoretical model presented in the literature, the skin depth of the material present within the region of interest affects the phase difference. Sensitivity matrix calculations can be adapted to incorporate the phase difference as we now explain.

According to Maxwell's equations, the Ampere's law that relates a magnetic field to an underlying current is given by

$$\nabla \times \vec{H} = \vec{J}. \tag{3.4}$$

It is known that,

$$\vec{B} = \mu\vec{H}. \tag{3.5}$$

Combining these two shows that when the frequencies are lower and the displacement current is not taken into account

$$\nabla \times \vec{B} = \mu\vec{J} \tag{3.6}$$

When the displacement current is also taken into account to model the skin effect, the total current within the sample is given by

$$\vec{J} = \vec{J_s} + \vec{J_e} \tag{3.7}$$

where J_s is the source current and J_e is the induced eddy current.

It is known that,

$$\vec{D} = \epsilon \vec{E} \tag{3.8}$$

and

$$\vec{J_e} = \sigma \vec{E}. \tag{3.9}$$

where $\vec{D}$ is given by the electric displacement field and ϵ is given by the permittivity of the medium.

Thus,

$$\nabla \times \vec{B} = \mu \vec{J} + \mu\sigma \vec{E} \tag{3.10}$$

It can also considered based on the gauge condition that,

$$\vec{E} = \frac{\partial \vec{A}}{\partial t} \tag{3.11}$$

Combining equations 3.10 and 3.11, we arrive at

$$\nabla \times \vec{B} = \mu \vec{J} + \mu\sigma \frac{\partial \vec{A}}{\partial t} \tag{3.12}$$

The curl of the magnetic vector potential is given by

$$\vec{B} = \nabla \times \vec{A} \tag{3.13}$$

Thus we arrive at the final relationship for the magnetic vector potential within a Magnetic Induction Tomography system.

$$\nabla \times \vec{B} = \nabla \times \nabla \times \vec{A} = \mu \vec{J} + \mu\sigma \frac{\partial \vec{A}}{\partial t} \tag{3.14}$$

$$-\nabla^2 \vec{A} = \mu \vec{J} + \mu\sigma \frac{\partial \vec{A}}{\partial t} \tag{3.15}$$

This equation proves the complex nature of the magnetic vector potential, and thereby the magnetic field, and provides a way to calculate its real and imaginary components via

$$-\nabla^2 \vec{A} = \mu \vec{J} + j\omega\mu\sigma \vec{A} \tag{3.16}$$

The in phase and the quadrature phase component can be calculated using the above equation. It can be solved using a Green's function expansion or other methods of solving a Partial Differential Equation. This equation confirms that the phase of the magnetic vector potential provides information about the skin depth and the conductivity of the material in the region of interest.

The approach that the chapter takes towards modeling the phase difference caused in MIT due to the sample in the region of interest is computational. The model is initially built, simulated, and solved in COMSOL, a PDE solving tool.

3.3 Computational Simulations

Modeling a physical system and calculating its properties can be done in two ways - i) theoretical and ii) computational. The computational modeling and simulation method is based upon solving a Partial Differential Equation using numerical algorithms. Some of the most commonly used numerical methods to solve PDEs include the Finite Difference Method (FDM), the Finite Element Method (FEM), the Finite Volume Method (FVM), the Method of Moments (MoM) etc.

The method that is used in general to solve magnetic vector potential based PDEs is the Finite Element Method (FEM). COMSOL uses the same to solve for magnetic field and magnetic vector potential. The method involves defining the domain where the Partial Differential Equation is to be solved, subdividing it into multiple small domains in a process called meshing, breaking them down into smaller linear systems, combining them together in the form of a stiffness matrix and solving it as a linear system.

COMSOL uses its AC/DC Electromagnetics module [99] to solve for the magnetic vector potential of the Magnetic Induction Tomography system. The two key equations that are to be solved to determine the magnetic vector potential and the magnitude and the phase of the secondary magnetic fields are described in Equations 2.32 and 2.36 in Chapter 2. The two equations are given by Biot- Savart Law and Ampere's law.

$$\vec{B}(r) = \frac{\mu}{4\pi} \iiint \frac{\vec{J_s}(r') \times |\vec{r} - \vec{r'}|}{|\vec{r} - \vec{r'}|^3} d^3r' \tag{3.17}$$

$$\nabla \times \frac{1}{\mu} \nabla \times \vec{A} + j\omega\sigma\vec{A} = \vec{J_s} \tag{3.18}$$

COMSOL solves the equations by dividing the domain where the PDE is to be solved into multiple subsections in a process known as meshing. Multiple types of meshes are possible, some of which are described below. The PDE is linearized and solved and then the stiffness matrix is compiled to arrive at the overall final solution. Once the final solution is found across the domain, post processing is performed in order to calculate the magnitude and the phase difference from the eddy current based secondary magnetic fields.

The steps that were used to simulate Magnetic Induction Tomography using the coil system described in Chapter 2 within COMSOL are now described.

3.3.1 Module Selection

Once the AC/ DC module is chosen, the Magnetic Fields interface within the Electromagnetic Fields window is used to create the required model. The Magnetic Fields interface is used to compute magnetic field and induced current distributions in and around coils, conductors and magnets. The simulation is done in three dimensions. The interface solves Maxwell's equations formulated using the magnetic vector potential as mentioned above.

3.3.2 Geometry

In order to create the domain for solving the PDE and creating the simulation, a Cartesian co-ordinate system is chosen. First, a universe within which the MIT system is to be simulated is drawn. It is a cube of size $200mm \times 200mm \times 200mm$.

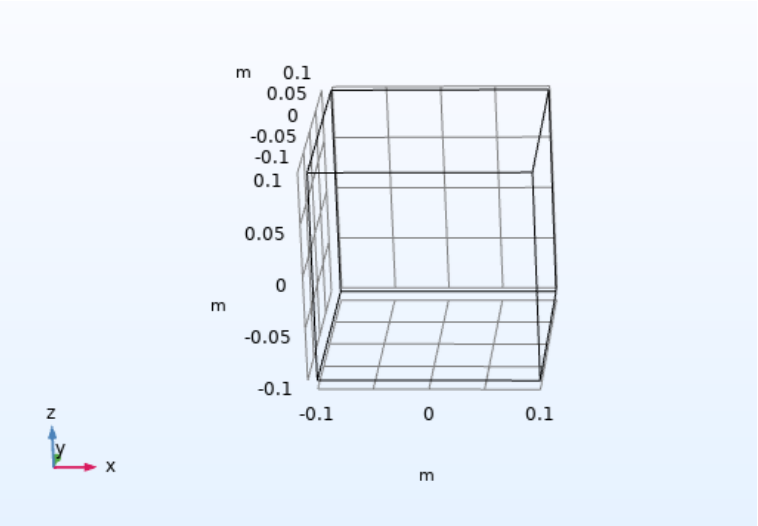

Figure 3.1: Universe for Simulation

The construction of the universe is succeeded by the design of the geometry of the excitor coil. The coil, as explained in Section 2.6.2, has an inner side of length 50 mm and outer side of length 54 mm.

The coil construction is started initially by choosing a 2D work plane. Two squares of sides 50 mm and 54 mm are drawn at the required co-ordinates to recreate the coil. The difference option is exercised to create the coil. A fillet option is used to chamfer off the sharp edges of the coil. A curve of radius 6 mm is used as the fillet.

Once a single workplane is confirmed, it is extruded by 2 mm to correspond to the thickness of the excitor coil. It is positioned at the required position co-ordinates (in this case, $x = 0, y = 0, z = 0$). The extruded version of the coil is shown below in Figure 3.3.

Now, the single coil within the domain can be replicated and rotated to create the four coil setup that would be used to generate the spherical harmonic excitor fields and probe the magnitude and the phase of the secondary magnetic fields.

A sample cubical block of size $10mm \times 10mm \times 10mm$ is placed in the center of the four coil setup and the region of interest, which is the imaging plane, is given by the $z = 10mm$ plane as shown in Figure 2.18. Figure 3.5 showcases the presence of the sample in the imaging plane. Once the block is placed in the center, it becomes a system that is experimentally realizable.

3.3.3 Materials

Once the geometry of the system to be simulated and the domain where it is placed are constructed, the material properties that are required for the simulation and the calculations are assigned to the respective domains.

Two main materials are to be used - i) one to define the coil and the sample and ii) one to define the space between them. One could either choose the required material from a previously available database or one could define the properties of the material and assign it to the respective domains.

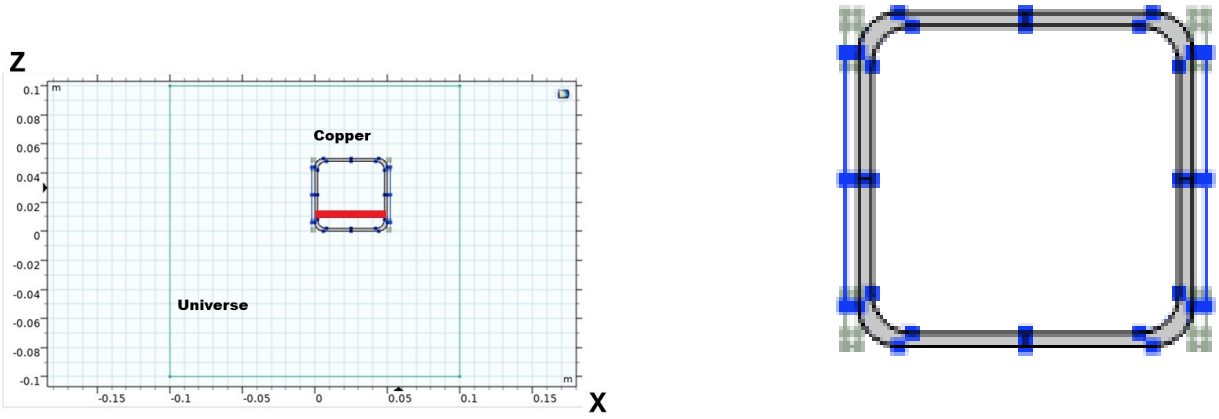

(a) 2D Workplane of Geometry

(b) Coil Model in COMSOL

Figure 3.2: Coil Geometry Modeling

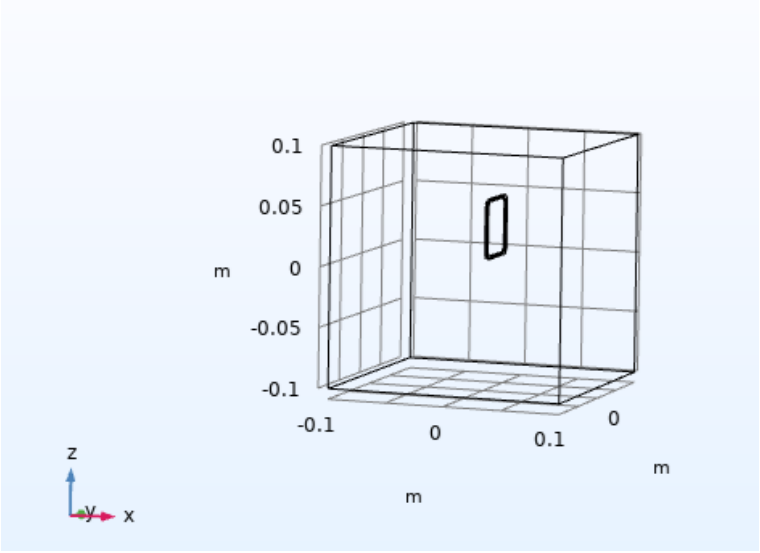

Figure 3.3: Single Excitor Coil within the domain

The two materials chosen are copper and air. The key properties that are defined are conductivity, permeability and permittivity of the materials. The following table has the defined values.

Material Properties			
Material	Conductivity in Sm^{-1}	Relative Permeability	Relative Permittivity
Copper	$5.9 * 10^7$	1.005	1
Air	0.000	1	1

Copper is assigned to the excitor coils and the sample, while air is assigned to the space in between them. Since a metallic Magnetic Induction Tomography imaging system is sought, the conductivity of copper is chosen as a specimen. In general, electrical conductivities of metallic conductors are on the order of 10^7 Sm^{-1}.

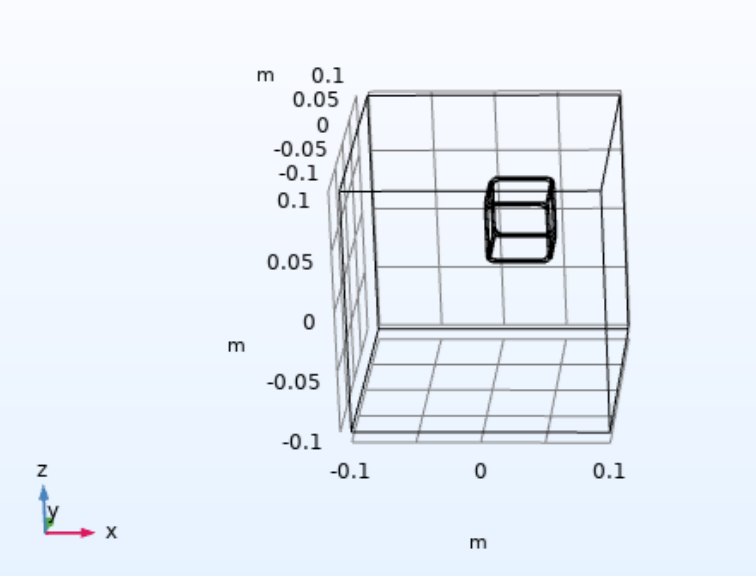

Figure 3.4: Four Coil Setup of the MIT System

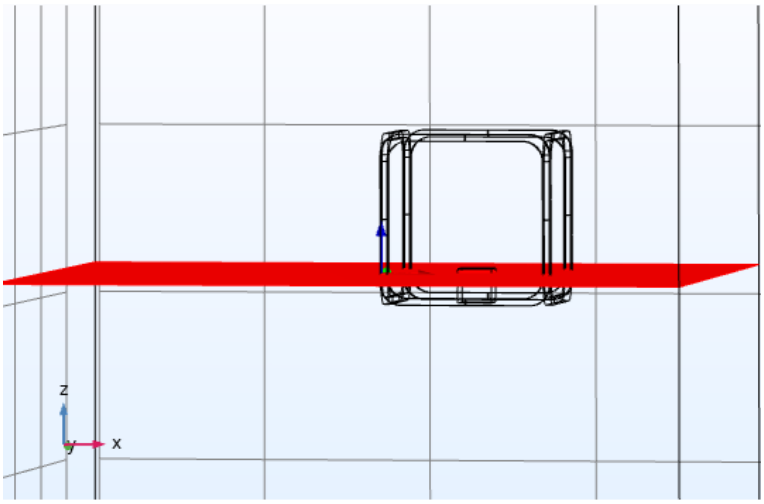

Figure 3.5: The final Magnetic Induction Tomography system with the cubical sample placed

3.3.4 Boundary Conditions

The computational simulation uses the Magnetic Insulation based boundary conditions present within the Magnetic Fields module as a boundary condition. It is determined by the equation

$$\vec{n} \times \vec{A} = 0 \tag{3.19}$$

The cross product of the magnetic vector potential with its normal vector is set to be null and it is applied across the universe of simulation. This is a form of Dirichlet boundary condition. There are many possible scenarios in which the Magnetic Insulation boundary condition is used. It could potentially be used as a symmetric boundary condition, a perfect electric conductor, an electrical ground connector, a waveguiding connection and others. In this case, the Magnetic Insulation boundary condition is used as an approximation of infinite free space.

The COMSOL Magnetic Fields module also incorporates the Ampere's Law based equation that is to be solved through out the universe. The equations that are being finally solved within the universe are given by

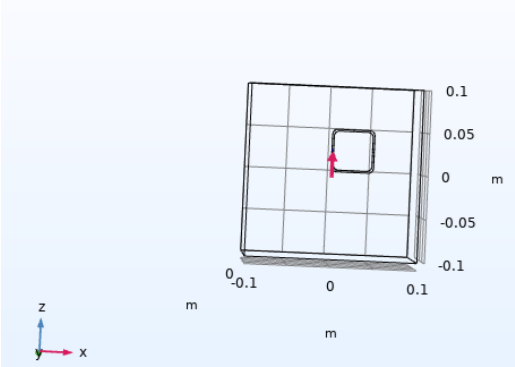

(a) Current Direction Determination

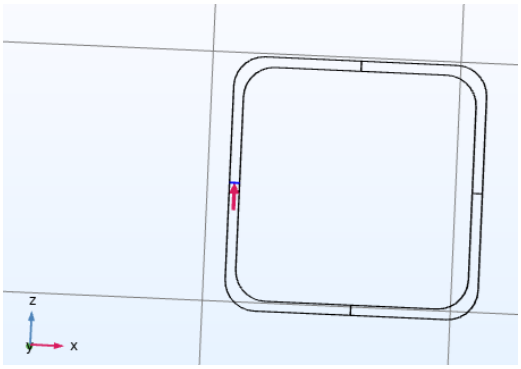

(b) Current Direction Determination along the cross section

Figure 3.6: Coil Current Direction Determination for a single coil

$$\vec{E} = -j\omega\vec{A} \tag{3.20}$$

$$\nabla \times \vec{H} = \vec{J} \tag{3.21}$$

$$\vec{B} = \nabla \times \vec{A} \tag{3.22}$$

$$\vec{J} = \sigma\vec{E} + j\omega\vec{D} \tag{3.23}$$

Once the Ampere's Law based equations are selected, the magnetization model is based upon the material and a linearized model is followed when it comes to magnetization permeability and dielectric permittivity.

$$\vec{B} = \mu_0\mu_r\vec{H} \tag{3.24}$$

$$\vec{D} = \epsilon_0\epsilon_r\vec{E} \tag{3.25}$$

The module of Magnetic Fields also has a subdivision called Coil, which is used to define the current strength and the direction of the current. The input magnetic field inducing element could be current based or voltage based. In this simulation, the current based magnetic field generation is chosen in order to easily correspond it with experimental results.

The current strength is 260.3 mA as calculated in Chapter 2. The number of coils is defined as 100 and the area of the cross section of the coil wire is 0.125 μm^2, as the wire is a Standard Wire Gauge No. 31. Within the geometry, the coil length multiplication factor and the coil area multiplication factor are set at 1.

The current density of the coil is calculated from the equation

$$\vec{J_e} = \frac{NI_{coil}}{\nu}\vec{e_{coil}} \tag{3.26}$$

where ν is the cross sectional area of the wire. The magnetic vector potential is initially set to 0 Wbm^{-1}.

The red arrow in Figure 3.6 indicates the direction of current flow considered, which is set using the interface of Geometry Analysis as an input option. Thus, the coil becomes a magnetic field source and a combination of these excitor coils could be used as primary fields in simulating Magnetic Induction Tomography.

Figure 3.7 shows the distribution of magnetic field produced by a single square shaped excitor coil placed in the origin along the $X = 0$ mm line. The direction of the magnetic field within the region of interest can be altered by changing the direction of the current within this excitor coil. Four such excitor coils put together form the experimental setup, as illustrated in Figure 2.14.

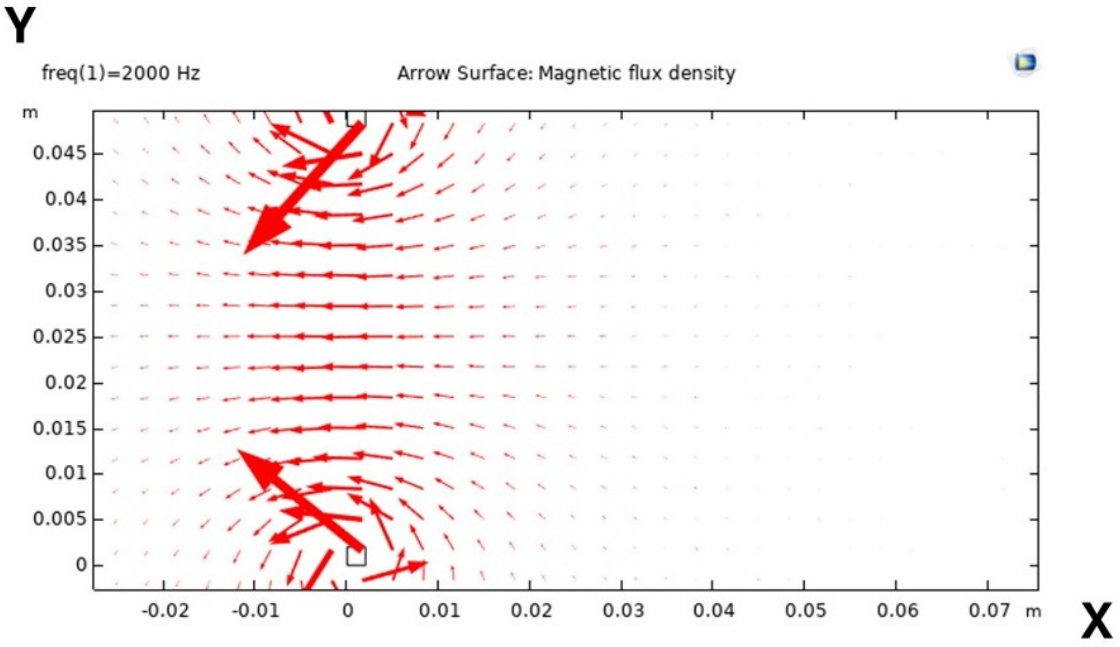

Figure 3.7: Magnetic Field distribution due to a single square shaped excitor coil

3.3.5 Meshing

The meshing of the universe is explained in detail in Chapter 2, Section 2.5.1. The same simulational setup is used in order to calculate both the secondary magnitude values and the phase caused due to the presence of the sample within the universe, and hence, the same meshing structure is used.

3.3.6 Equation Solutions

The equation solver that seeks to compute the final solution of the PDE involves in two parts - i) Coil Geometry Analysis and ii) Frequency Domain Analysis.

Coil Geometry Analysis is a preprocessing step that is used to compute the current distribution based on the input current and the current direction. The analysis is performed over a homogeneous multiturn coil in the case of this simulation.

The frequency domain analysis is the key component of the equation solver. The chosen frequency to run the analysis is at 2000 Hz. This part of the analysis compiles the stiffness matrix together by combining all the nodes. Sometimes, the problem becomes ill-posed due to the lack of proper meshing or problems with user defined materials. It is averted by the lack of adding a small element of conductivity to offset the zeros caused in inverting the stiffness matrix.

Two studies are set up so as to find the phase and the magnetic field difference caused due to the presence of the copper block shown in Section 3.2 (Figure 3.5). The time taken for the first study with the sample for four different spherical harmonics is approximately 2 to 3 hours. The time taken for the study without the sample is roughly 1 to 2 hours. It becomes easy to calculate the second study as there isn't a need to calculate skin depth based phase effects.

3.3.7 Results

The plane of imaging, as shown in Chapter 2, is given by $z = 10mm$. Line graphs and surface plots are used in order to present the results. The points of experimental measurement of phase are the same as the points of measurements of magnetic field differences and are illustrated in Figure 2.19. Quadratic Lagrange polynomials are used to interpolate the final results calculated at nodes out through the surface plot. The phase is calculated within the simulation and on the surface of the plot using the equations

$$\phi_x = \tan^{-1}(\frac{imag(\vec{B_x})}{real(\vec{B_x})}) \tag{3.27}$$

$$\phi_y = \tan^{-1}(\frac{imag(\vec{B_y})}{real(\vec{B_y})}) \tag{3.28}$$

Figures 3.8 and 3.9 display the phase difference across the plane of imaging when the sample is placed and when it is removed. The silhouette of the sample and the excitor coils are also shown in the figures. One can also find the variations in patterns of phase difference as different spherical harmonic excitor fields are applied to induce eddy currents. The black squares present within the simulated figures indicate the positions of the excitor coils used for primary fields. The final image reconstructions will be made with magnitude and phase difference measured along the lines shown in Figure 2.19.

3.4 Experimental Methods

As mentioned in Chapter 2, the experimental setup consists of a signal generator whose input signals are amplified by a RF amplifier. The signal is used as a current source for excitor coils. The magnetic field is measured by a Lakeshore F71 Teslameter, a Hall effect based magnetometer. The probe is attached to a 50 mm Thorlabs linear probe. The experiment uses a National Instruments Data Acquisition device NI-6205. The control code required for running the experimental setup is written in LabVIEW and Python. The entire setup is mounted on an optical breadboard with balance compensation. This section outlines the mechanism by which the magnitude and the phase of secondary magnetic field are recorded and the phase difference is calculated.

3.4.1 Measuring the magnitude of the magnetic field

The Lakeshore F71 Teslameter is a magnetometer that works based upon the Hall effect, where a voltage is developed across the cross section of applied magnetic fields. The magnetometer has a bandwidth and a frequency range of $0 - 75$ kHz. There are three different modes - DC, AC and High Frequency. The DC mode helps measure direct current based magnetic fields and the AC mode helps measure magnetic fields of frequencies $0 - 200$ Hz. For frequencies beyond 200 Hz, High Frequency mode offers the best results based on the sampling window. Since the experiment is performed at 2000 Hz, High Frequency mode is chosen to measure the secondary magnetic fields.

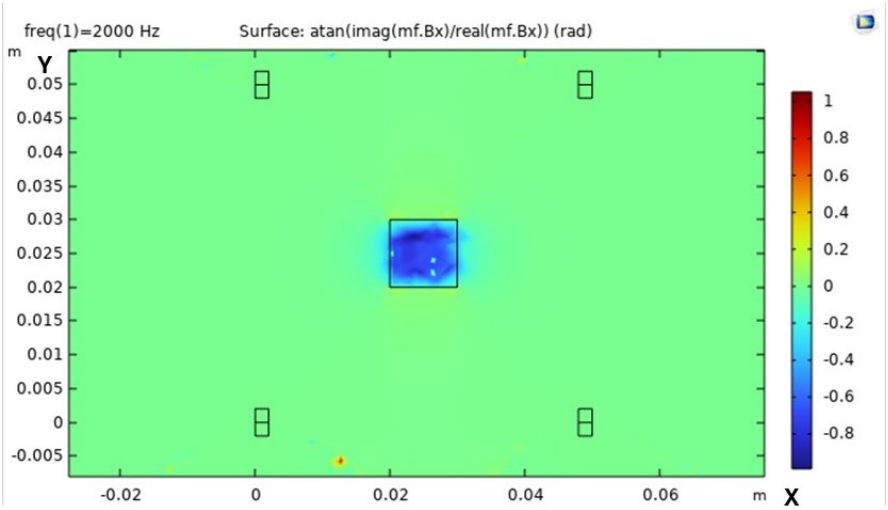

(a) X Gradient ϕ_x

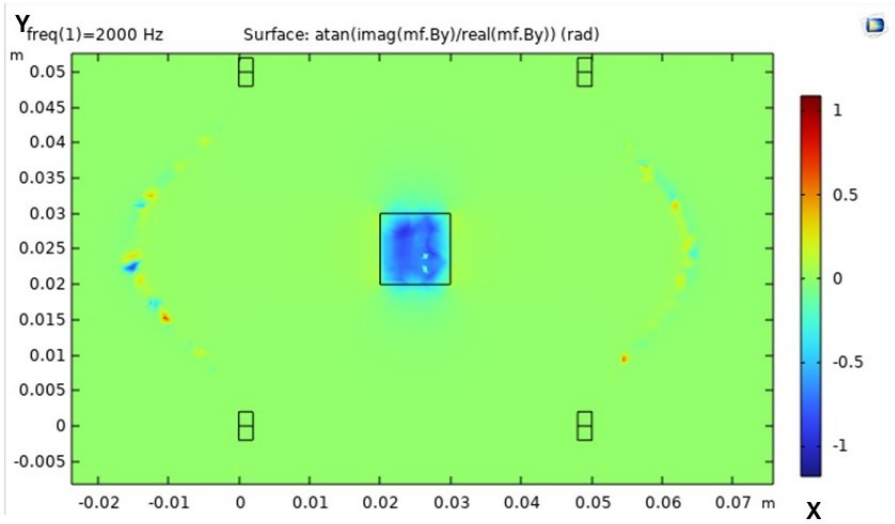

(b) Y Gradient ϕ_y

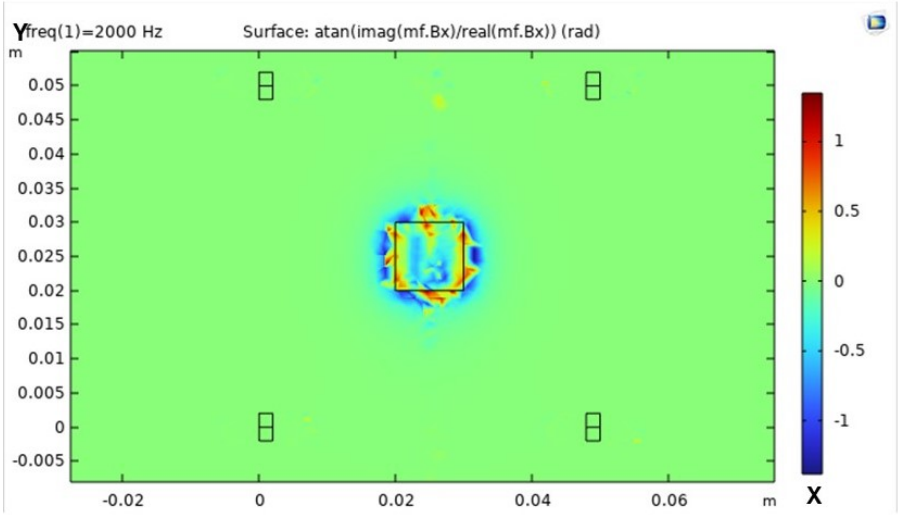

(c) SH20 Gradient ϕ_x

Figure 3.8: Phase Simulations of the Region of Interest of Imaging using a) X Gradient, b) Y Gradient and c) SH2,0 Phase Difference simulated along X axis using spherical harmonic excitor fields (The black squares indicate the positions of the four excitor coils)

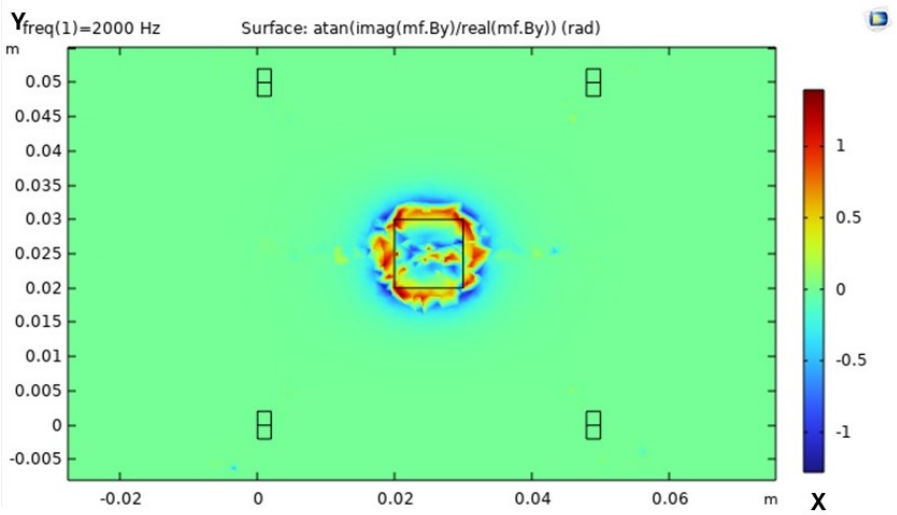

(a) SH20 Gradient ϕ_y

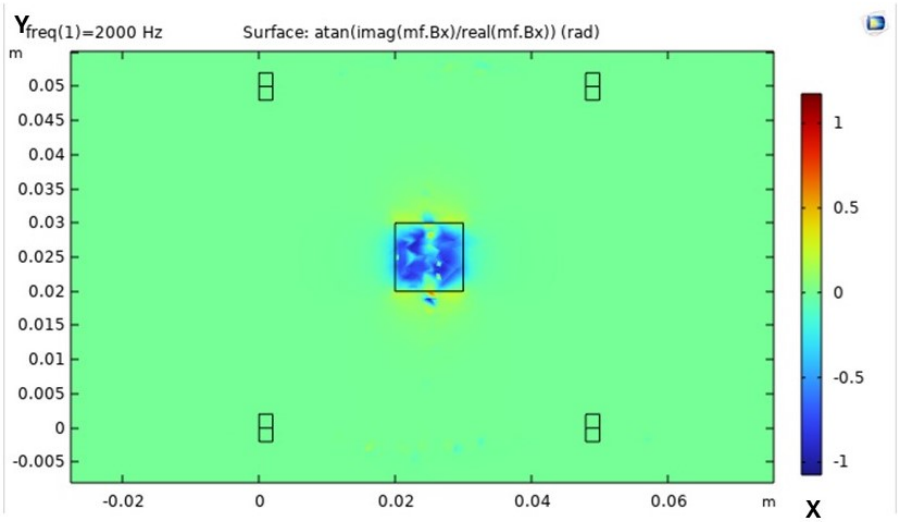

(b) SH22 ϕ_x

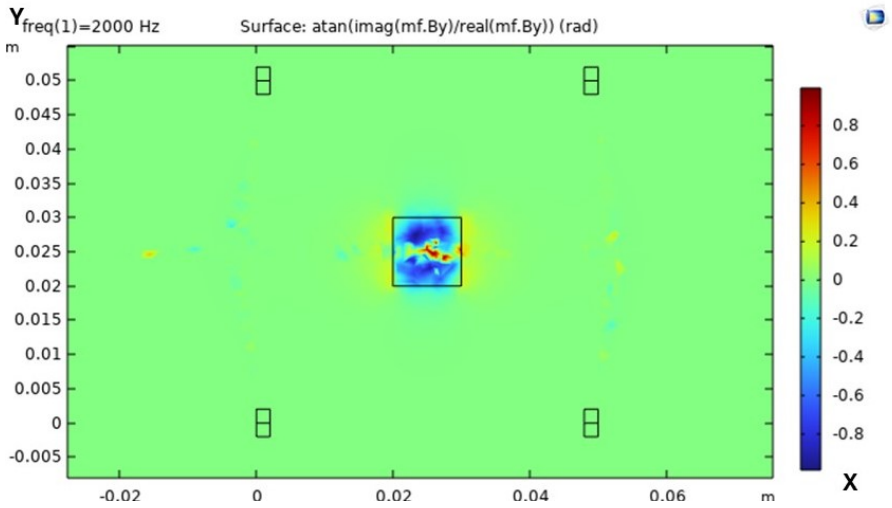

(c) SH22 ϕ_y

Figure 3.9: Phase Simulations of the Region of Interest of Imaging using a) SH20 simulated along Y axis, b) SH22 simulated along X axis and c) SH22 simulated along Y axis (The black squares indicate the positions of the four excitor coils)

There are two steps in measuring the magnetic field. The direction of the magnetic field is measured in DC mode as it is able to measure the polarity of the field better. The magnitude of the magnetic field (AC high frequency signal) is measured in terms of its RMS (Root Mean Square) value.

The excitor coils are mounted on the setup, which is additively manufactured using 3D printing, in a square setup as showcased in Figure 2.14. The CAD (computer Aided Design) design of the four coil setup used as a support in experimental measurements to be mounted on the optical breadboard is presented in Figure 3.10. The sensing probe is attached to a mount, and then screwed in to a Thorlabs linear translation stage that is capable of moving 50 mm with a minimum achievable resolution of 0.05 μm. The probe is controlled by a linear motor controller that actuates the linear translation stage.

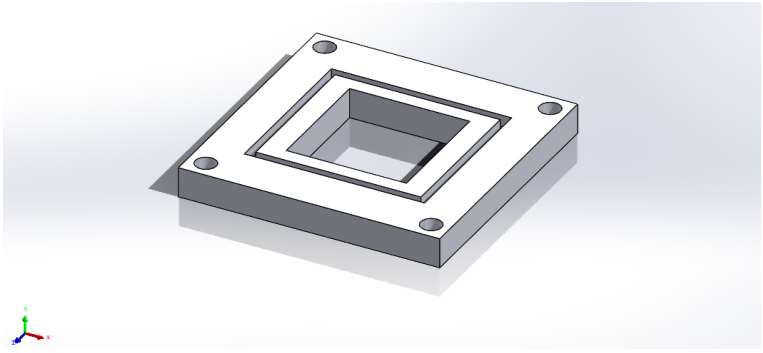

Figure 3.10: CAD Design used in additive manufacturing for experimental setup

In order to measure the magnitude and the polarity of the magnetic field, the magnetometer is set to DC mode first. The data is recorded for 5s. The sampling frequency is 100 Hz and 5 seconds of 10 ms of data are recorded and stored as a CSV file.

Once the polarity and the magnitude of the field are measured using the DC mode, the magnetometer is switched to High Frequency mode to measure the magnitude of the induced eddy based fields. The recorded data is then exported as a CSV file, then filtered and processed to find the AC magnitude of the magnetic field, to be compared later with the data acquired from the LabVIEW system. The filtering method used is an average filter (Savitzky-Golay filtering) [110], which acts as a smoothening filter. This procedure is repeated both in the presence and the absence of the sample placed within the region of interest, with the sensing probe placed at the lines of measurement as indicated in Figure 2.19.

3.4.2 Measuring the phase of the magnetic field

The data acquisition system for phase measurements is built using LabVIEW. The phase difference between the primary magnetic field and the secondary, induced magnetic field is found by simultaneously measuring the phase of both the fields. The code that is used to measure the phase difference is displayed in Figure 3.12.

The block diagram illustrates the way two different phases are measured and the phase difference is calculated. The National Instruments data acquisition device (DAQ) consists of 16 analog input and output (I/O) channels and 8 digital input and output (I/O) channels. Two analog I/O channels, AI_0 and AI_1, are used in the experiment. The input signal from

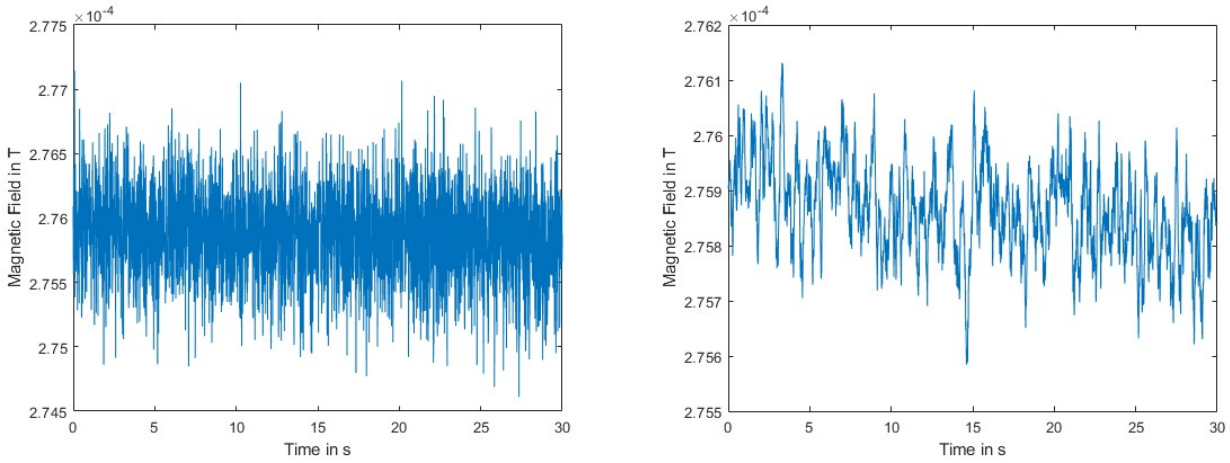

(a) Magnetic Field B_z measured at $X = 45$ mm line at the point (45 mm, 25 mm)

(b) Magnetic Field after Savitzky-Golay average filtering

Figure 3.11: Savitzky-Golay Filtering

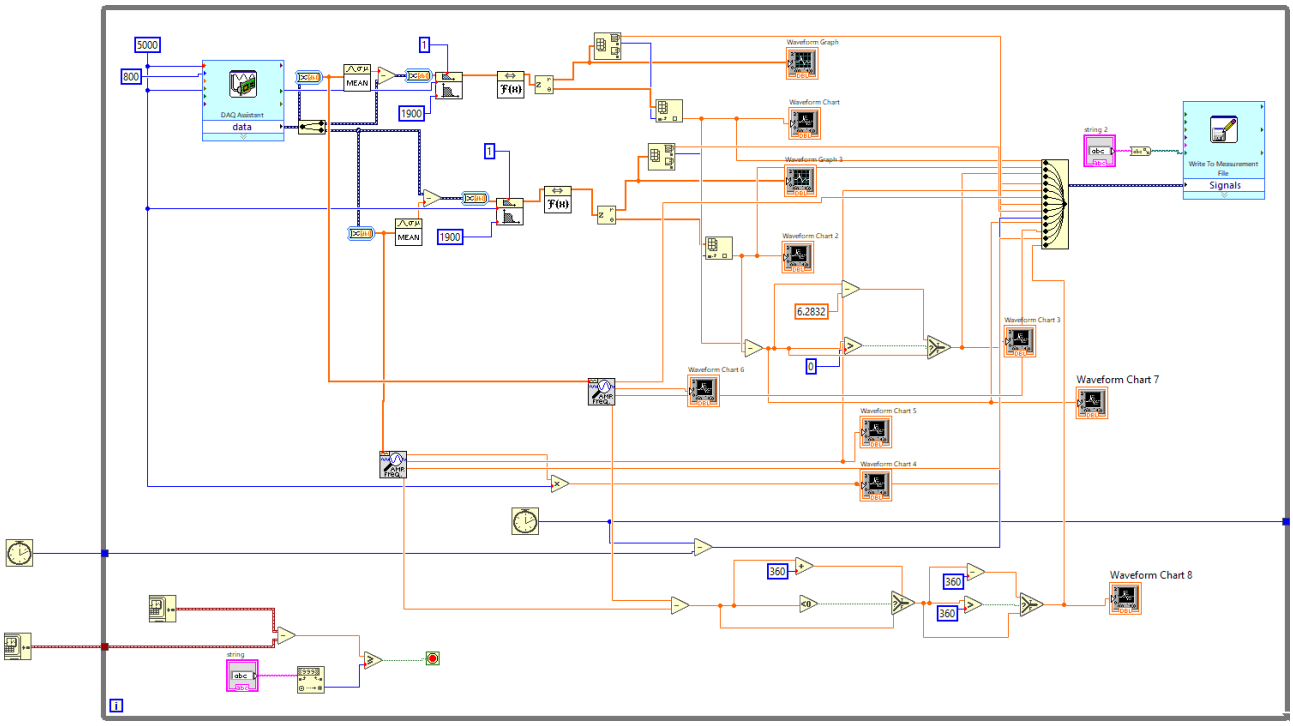

Figure 3.12: Block Diagram to measure phase difference

the signal generator that is used as a current source to the excitor coils to create the primary magnetic field is connected to AI_0. The sensor probe from the magnetometer is connected to AI_1. The LabVIEW block code shown in Figure 3.12 uses these two signals to calculate the phase difference.

The measured magnetic fields correspond to the voltages. The analog voltage from both the channels is acquired using the DAQ assitant in the block as the first step to calculating the phase difference. The experiment is run at a frequency of 2000 Hz. According to the sampling theorem, it is known that the sampling frequency should be at least twice the frequency of the signal to be measured.

$$f_s \geq 2f_m \tag{3.29}$$

Since the input signal frequency is 2000 Hz, the sampling rate is chosen to be 5000 Hz. The number of samples that will be recorded at 800 per second. In LabVIEW, there are two types of signal sample acquisition. While the sampling rate determines the rate at which the sample data points are acquired from the sensor, these data points are stored on a temporary buffer present within the DAQ device. The number of samples recorded determines the rate at which these samples are then sent to the software environment and processed. The analog channels and the DAQ device has a range of -10 V to $+10$ V and the sensed magnetic fields are converted and correspond to this scale of the analog channels.

The two measured input signals are initially filtered to remove other frequency components. First, the signals are subtracted from their means to get rid of the DC signal and low frequency signals on the range of $0 - 10$ Hz.

$$x_1^{'}(t) = x_1(t) - \mu(x_1(t)) \tag{3.30}$$

$$x_2^{'}(t) = x_2(t) - \mu(x_2(t)) \tag{3.31}$$

The signals are then sent through a high pass filter Butterworth Type 3 filter. The cut off frequency is 1900 Hz. The idea behind this filtering is to eliminate all of the lower frequency components completely before proceeding with the calculation of phase from the signal.

Once the filtering is performed and the signal at 2000 Hz is boosted, the signal is converted to frequency domain using a Fourier transformation.

$$X_1(\omega) = \int_{-\infty}^{+\infty} x_1^{'}(t) e^{-i2\pi\omega t} dt \tag{3.32}$$

$$X_2(\omega) = \int_{-\infty}^{+\infty} x_2^{'}(t) e^{-i2\pi\omega t} dt \tag{3.33}$$

After the signals are converted to frequency domain using the Fourier transform, the phase of the primary component (2000 Hz signals) of the signals is measured using

$$\phi_1 = \tan^{-1}\left(\frac{imag(X_1(\omega))}{real(X_1(\omega))}\right) \tag{3.34}$$

$$\phi_2 = \tan^{-1}\left(\frac{imag(X_2(\omega))}{real(X_2(\omega))}\right) \tag{3.35}$$

The final phase is calculated by considering if the secondary magnetometer signal is leading or lagging the primary signal by a full cycle and making adjustments accordingly. The final phase difference between the two signals - the input signal and the signal from the magnetometer is given by

$$\phi = \phi_1 - \phi_2 \tag{3.36}$$

The amplitudes and the phases of both the signals and the phase difference between them are recorded and exported to be post processed and analyzed further. The entire cycle of operations described above is programmed to happen for a particular period of predetermined time. There are also other inbuilt programmed functions as part of LabVIEW that could calculate the amplitude and phase of a signal and they are also explored and data measured by them is recorded as a supplementary figure to be compared with.

The difference in phase due to the presence of the copper sample is calculated by using a difference measurement. The copper sample is placed in its position first, the magnetometer probe is moved along the four lines of measurement shown in Figure 2.19, and the phase is measured and recorded. Since it is a differential measurement of phase, the sample is now removed, the probe is placed at the same position again and the phase is measured again. The difference between the two phase measurements gives the phase difference caused due to the presence of the copper sample.

The two measures of the magnetic field and phase difference are to take place simultaneously. An automation of the experiment is performed with Python controlling the time and the positions in which the measurements are made. The idea of multi-threading is used to measure the field and the phase difference simultaneously with a programmable trigger activating both. The magnetic field magnitudes and phase differences along all three axes are measured as part of the experiment.

3.5 Phase Effects of Spherical Harmonic Magnetic Vector Fields

In Chapter 2, the lines of measurement where the magnetic field magnitude and phase are measured are shown in Figure 2.19. The excitor spherical harmonic fields create different induction patterns within the region of interest and the copper sample of high conductivity, and it is reflected in the phase difference measured from the boundaries to be used for tomographic reconstruction.

Figures 3.13,3.14,3.15 and 3.16 showcases the difference in phase measured along various axes in the presence of different spherical harmonic magnetic fields as illustrated in Figure 2.10. As can be seen from the figures, the phase difference in the presence and absence of the copper sample has different ranges of magnitudes for different spherical harmonic magnetic fields. The figures showcase the phase difference along four measuring lines $Y = 0$ mm, $Y = 45$ mm, $X = 0$ mm and $X = 45$ mm. The phase difference is measured in radians. The blue lines are computationally simulated representations of phase difference made using COMSOL, while the red lines are experimentally measured at nine different points along the measuring lines mentioned above.

The Spherical Harmonic $m = 1, n = -1$ field with a constant B_x value has a phase difference ϕ_x of 0.006 radians along the $Y = 0$ mm and $Y = 45$ mm lines of measurement, which are shown in Chapter 2. The phase difference while using the same spherical harmonic excitor field along $X = 0$ mm and $X = 45$ mm is -0.003 radians. The presence of the sample in the same direction decreases the phase difference. This can be seen in Figure 3.13(c).

The use of the Spherical Harmonic $m = 1, n = 1$ field produces a similar effect in the phase difference measured in the presence and absence of the sample. This harmonic field reverses the phase effects caused by the SH $m = 1, n = -1$ field, since it has a constant B_y field along Y axis. Thus, the phase difference measured along Y axis, along the lines of $Y = 0$ mm and $Y = 45$ mm is reduced to -0.003 radians while, the phase difference measured along the X axis, along the lines of $X = 0$ mm and $X = 45$ mm is given by 0.006 radians. It is seen in Figure 3.14(c).

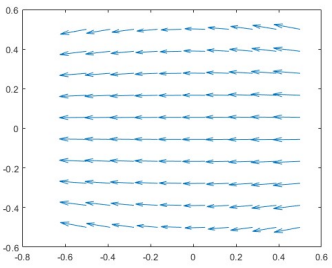

(a) Using Spherical Harmonic $n = 1, m = 1$ as excitor field

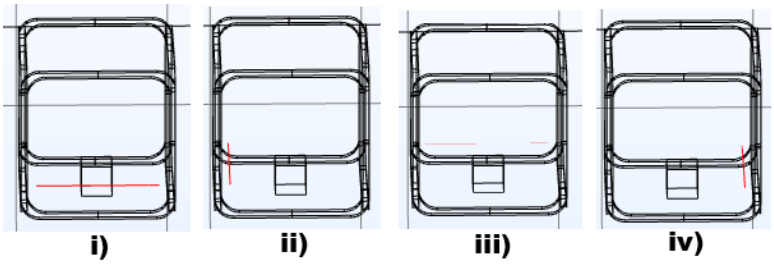

(b) i) Measuring line $Y = 5$ mm, ii) Measuring line $X = 5$ mm, iii) Measuring line $Y = 45$ mm, iv) Measuring line $X = 45$ mm, axes directions as given by Figure 2.19

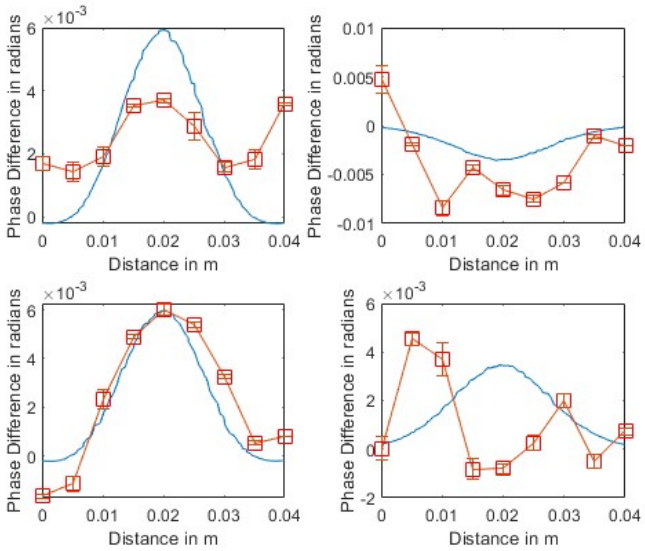

(c) Top Left: Phase Difference ϕ_x along $Y = 5$ mm, Top Right: Phase Difference ϕ_x along $X = 5$ mm, Bottom Left: Phase Difference ϕ_x along $Y = 45$ mm, Bottom Right: Phase Difference ϕ_x along $X = 45$ mm

Figure 3.13: Difference in phase in the presence and absence of a sample measured using spherical harmonic magnetic fields (in red) and calculated (in blue) using X Gradient Field Vector as excitor field

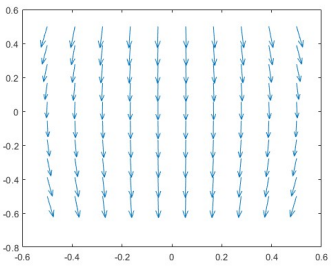

(a) Using Spherical Harmonic $n = 1, m = -1$ as excitor field

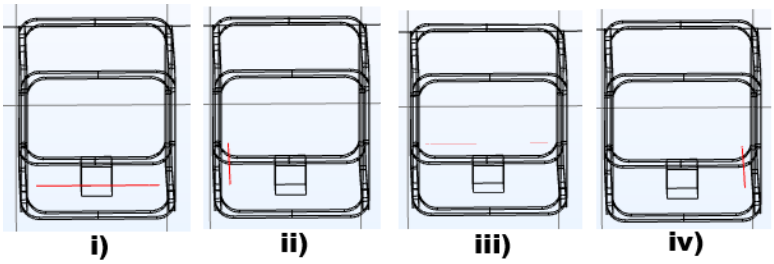

(b) i) Measuring line $Y = 5$ mm, ii) Measuring line $X = 5$ mm, iii) Measuring line $Y = 45$ mm, iv) Measuring line $X = 45$ mm, axes directions as given by Figure 2.19

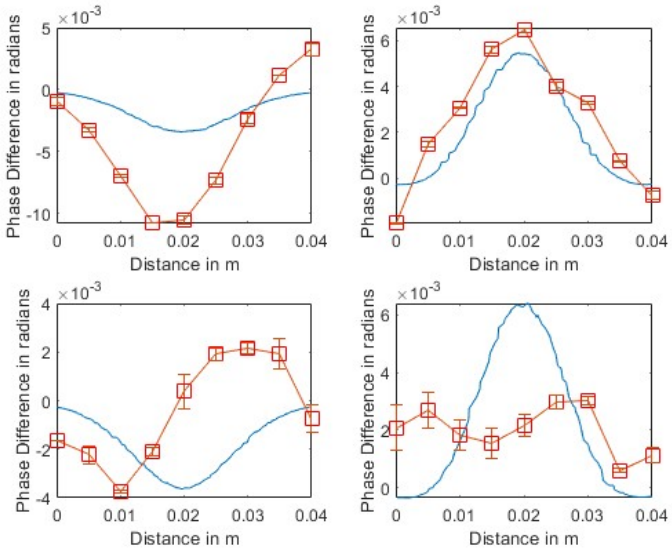

(c) Top Left: Phase Difference ϕ_y along $Y = 5$ mm, Top Right: Phase Difference ϕ_y along $X = 5$ mm, Bottom Left: Phase Difference ϕ_y along $Y = 45$ mm, Bottom Right: Phase Difference ϕ_y along $X = 45$ mm

Figure 3.14: Difference in phase in the presence and absence of a sample measured using spherical harmonic magnetic fields (in red) and calculated (in blue) using Y Gradient Field Vector as excitor field

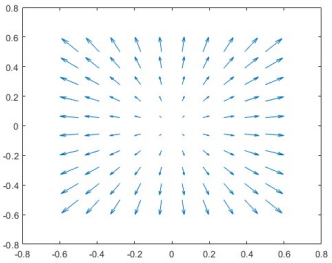

(a) Using Spherical Harmonic $n = 2, m = 0$ as excitor field

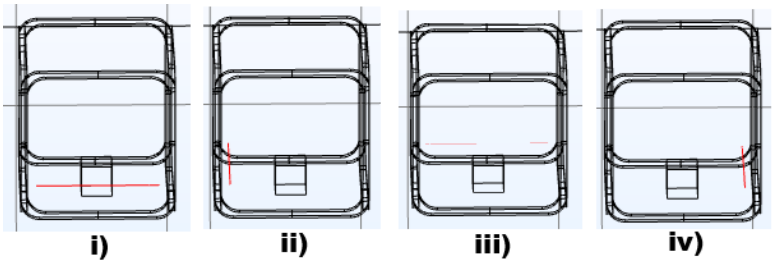

(b) i) Measuring line $Y = 5$ mm, ii) Measuring line $X = 5$ mm, iii) Measuring line $Y = 45$ mm, iv) Measuring line $X = 45$ mm, axes directions as given by Figure 2.19

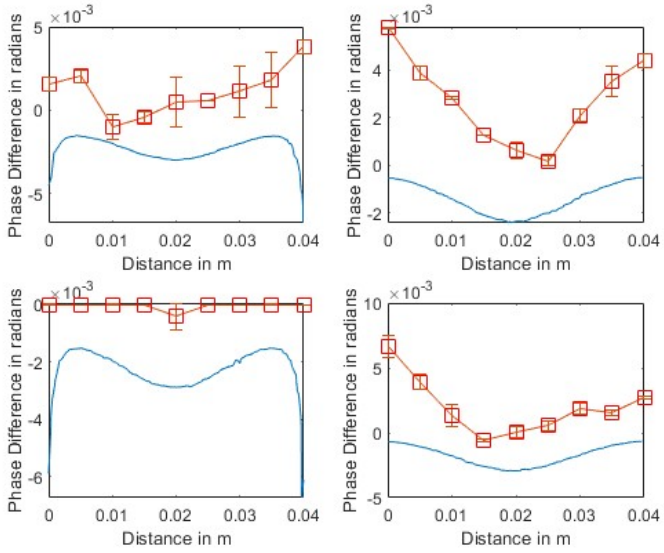

(c) Top Left: Phase Difference ϕ_x along $Y = 5$ mm, Top Right: Phase Difference ϕ_x along $X = 5$ mm, Bottom Left: Phase Difference ϕ_x along $Y = 45$ mm, Bottom Right: Phase Difference ϕ_x along $X = 45$ mm

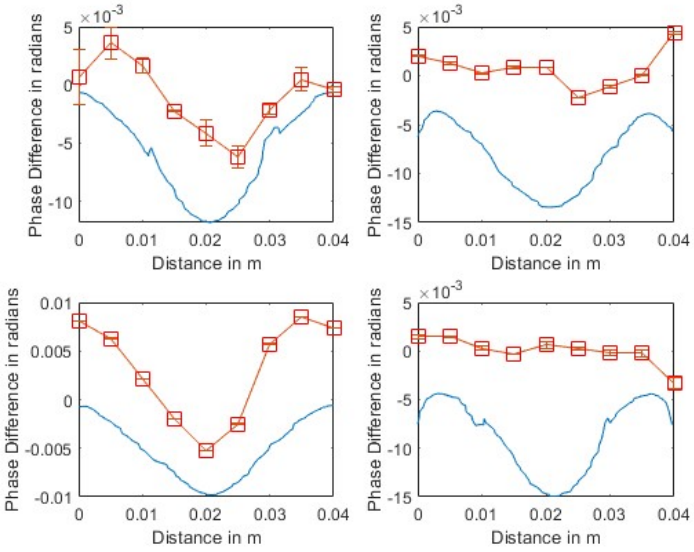

(d) Top Left: Phase Difference ϕ_y along $Y = 5$ mm, Top Right: Phase Difference ϕ_y along $X = 5$ mm, Bottom Left: Phase Difference ϕ_y along $Y = 45$ mm, Bottom Right: Phase Difference ϕ_y along $X = 45$ mm

Figure 3.15: Difference in phase in the presence and absence of a sample measured using spherical harmonic magnetic fields (in red) and calculated (in blue) using SH2,0 Gradient Field Vector as excitor field

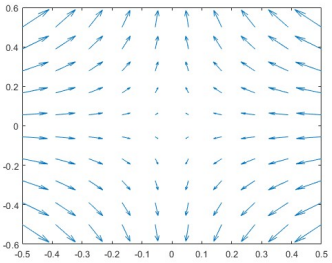

(a) Using Spherical Harmonic $n = 2, m = 2$ as excitor field

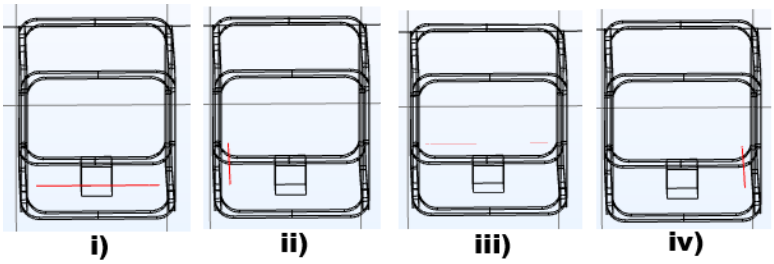

(b) i) Measuring line $Y = 5$ mm, ii) Measuring line $X = 5$ mm, iii) Measuring line $Y = 45$ mm, iv) Measuring line $X = 45$ mm, axes directions as given by Figure 2.19

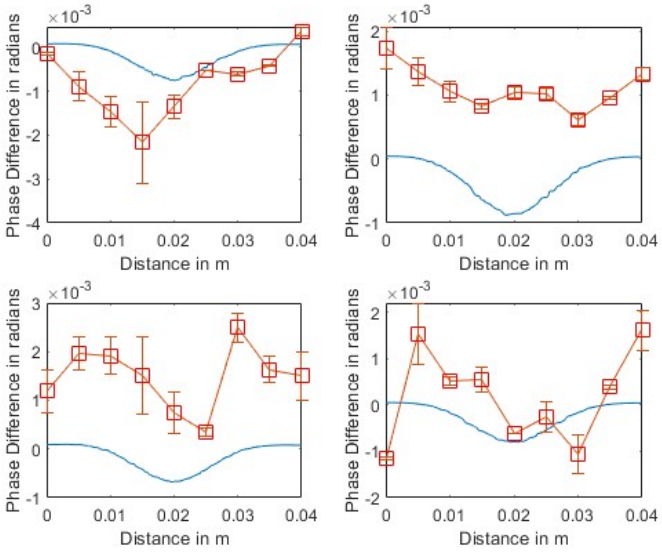

(c) Top Left: Phase Difference ϕ_x along $Y = 5$ mm, Top Right: Phase Difference ϕ_x along $X = 5$ mm, Bottom Left: Phase Difference ϕ_x along $Y = 45$ mm, Bottom Right: Phase Difference ϕ_x along $X = 45$ mm

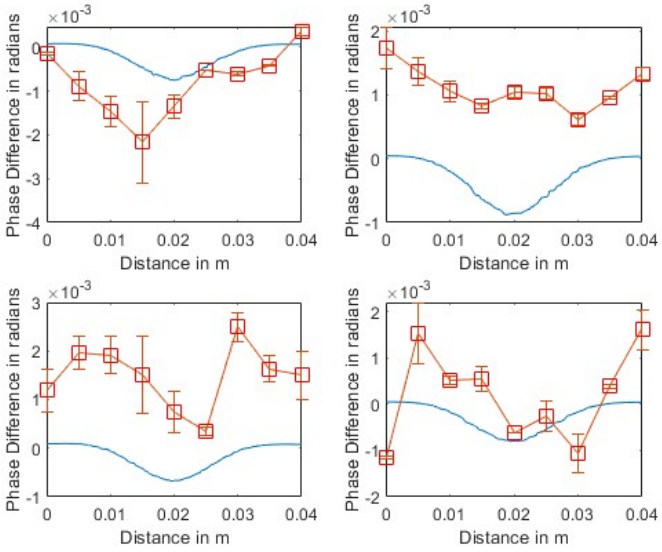

(d) Top Left: Phase Difference ϕ_y along $Y = 5$ mm, Top Right: Phase Difference ϕ_y along $X = 5$ mm, Bottom Left: Phase Difference ϕ_y along $Y = 45$ mm, Bottom Right: Phase Difference ϕ_y along $X = 45$ mm

Figure 3.16: Difference in phase in the presence and absence of a sample measured using spherical harmonic magnetic fields (in red) and calculated (in blue) using SH2,2 Gradient Field Vector as excitor field

Spherical Harmonic $m = 2, n = 0$ is a divergent field as shown in Figure 2.10c. The phase differences measured along all four measurement lines and both axes are presented in Figures 3.15(c) and 3.15(d). The phase difference, ϕ_x, along the X axis is -0.002 radians with two peaks along $Y = 0$ mm and $Y = 45$ mm lines and -0.002 radians with a single peak along $X = 0$ mm and $X = 45$ mm. The situation reverses for the phase difference, ϕ_y, along the Y axis with two peaks along $X = 0$ mm and $X = 45$ mm measuring lines, and one peak along $Y = 0$ mm and $Y = 45$ mm lines. The magnitude is -0.01 radians for the former and -0.005 radians along the latter. The nature of this phase difference variation is made possible because of the nature of the excitor field.

Finally, the phase differences caused by the spherical harmonic excitor field $m = 2, n = 2$ are displayed in Figure 3.16(c) and 3.16(d). The phase difference ϕ_x measured along the X axis along all the measurement lines is -0.00085 radians, while the phase difference ϕ_y measured along the Y axis will be 0.004 radians along the same measurement lines. The excitor field diverges away from the center as shown in Figure 2.10d, hence the phase difference pattern is measured to be really low.

The computationally calculated COMSOL and experimentally measured results have broadly similar profiles although the agreement is less good for spherical harmonic fields SH$m = 2, n = 0$ and SH$m = 2, n = 2$. The anomaly or the difference is 0.003 radians. The range is slightly measured to be higher. This can be attributed to external noise influences, including mild vibrations of measurements. Further accurate measurements can be made using more sophisticated phase measurement techniques like the use of Lock In Amplifiers and Phasemeters, and avoiding vibrations. Errors can also be dealt with using better inverse algorithms as mentioned in Section 1.6.2 for better and more efficient imaging.

3.6 Magnetic Field Magnitude and Phase Based Reconstructed Images Using Inverse Radon Transforms

Inverse Radon Transformation is a method used in medical imaging and tomography to reconstruct images based on their projections from various parallel sources. When a 2D image is projected by a set of parallel beams (could potentially be X- Rays in a CT or a PET scan, magnetic fields as in MRI scanning or other forms of electromagnetic waves in imaging), it forms a 1D projection. A Radon transform seeks to capture this projection from various angles ranging from 0 to 2π radians (0° to 360°) [111] [112]. The Radon transformation works on the principle of the Fourier Slice theorem, and is often referred to as a sinogram. The Radon transformation of a two dimensional function $f(x, y)$ is given by

$$R(\tau, p)(f(x, y)) = \int_{-\infty}^{+\infty} \int_{-\infty}^{+\infty} f(x, y)\delta[y - (\tau + px)]dxdy \tag{3.37}$$

$$R(r, \theta)(f(x, y)) = \int_{-\infty}^{+\infty} \int_{-\infty}^{+\infty} f(x, y)\delta[x\cos\theta + y\sin\theta - \rho]dxdy \tag{3.38}$$

$$0 \leq \theta \leq 2\pi$$

The δ(x) function converts the two dimensional integral to a one dimensional projection based integral along the parallel beam. Here, τ is the intercept of the line, p is its slope and, ρ is line along which the 2D function is converted to a projection.

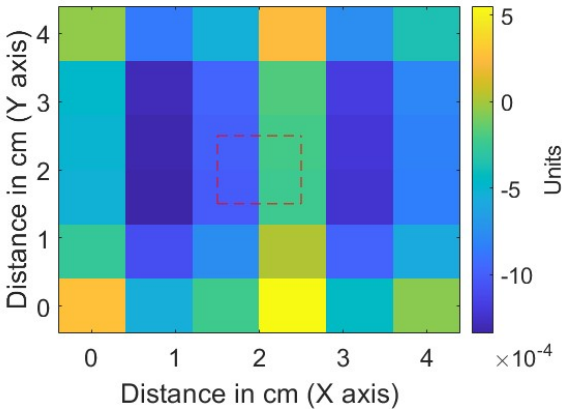

(a) Phase based reconstruction using projections from 4 different angles

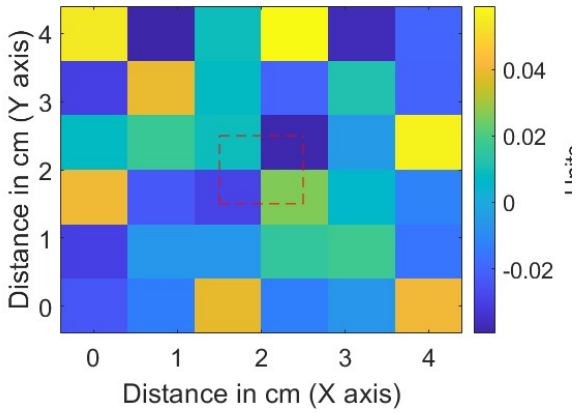

(b) Phase based reconstruction using projections from 8 different angles

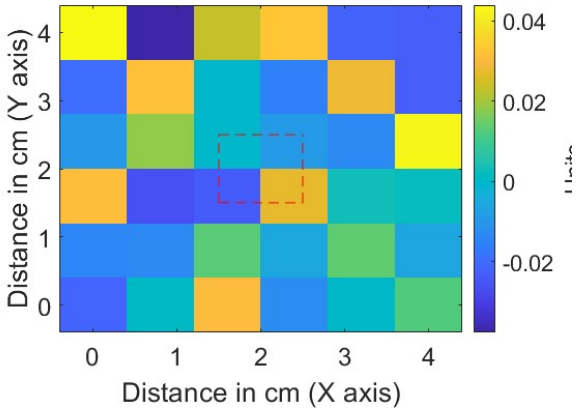

(c) Phase based reconstruction using projections from 12 different angles

Figure 3.17: Phase based reconstructed images of electrical conductivity using spherical harmonic magnetic fields through Inverse Radon Transform (The red square represents the ideal target image)

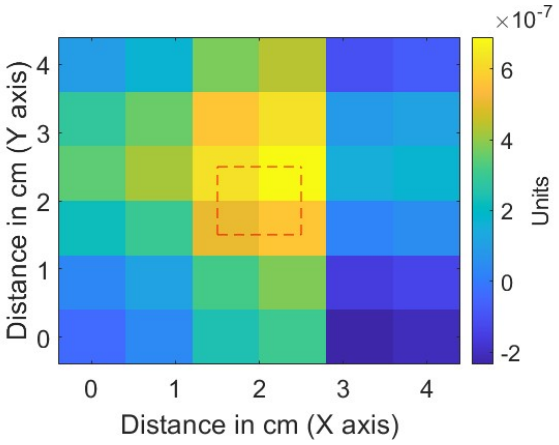

(a) Field based reconstruction using projections from 4 different angles

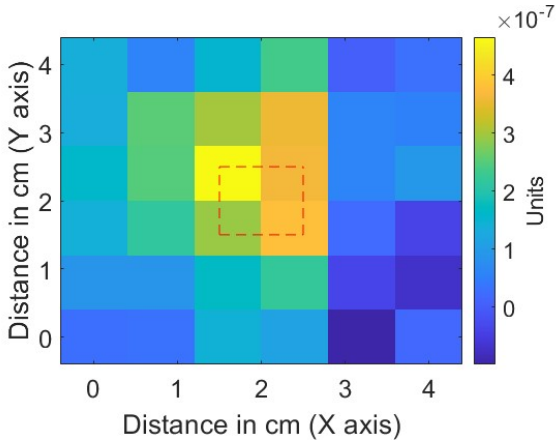

(b) Field based reconstruction using projections from 8 different angles

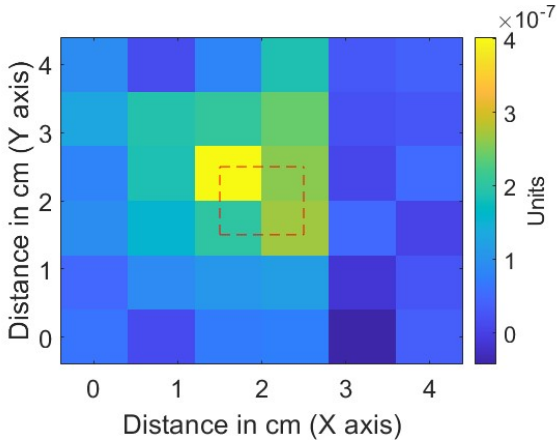

(c) Field based reconstruction using projections from 12 different angles

Figure 3.18: Field based reconstructed images of electrical conductivity using spherical harmonic magnetic fields through Inverse Radon Transform (The red square represents the ideal target image)

The inverse Radon transform [113] seeks to take the linear projection along a particular angle and convert it back to a 2D image. Multiple projections from across different angles are combined together to arrive at the final 2D image. The inverse Radon transform could also be formulated as an inverse problem, as usually done in the case of tomographic reconstructions. It is accomplished by a method known as Filtered Backprojection (FBP), based on the Fourier Slice or Central Slice theorem as mentioned above. The inverse Radon transformation is given by

$$f(x,y) = \frac{1}{2\pi}\int_{-\infty}^{+\infty} \frac{d}{dy} H[R(p, y - px)]dp \tag{3.39}$$

where H is the Hilbert transform and p is the slope of the line. It can be used to find the angle at which the parallel beams are projected.

Radon transformation also enables image reconstruction in Magnetic Induction Tomography. The spherical harmonic vector magnetic fields that have been used as excitor fields in this experiment are showcased in Chapter 2. The four spherical harmonics used can be considered parallel beams of magnetic fields and the magnetic field magnitude and phase differences are the linear projections caused by the parallel beams. There are 12 different angles from which the four spherical harmonic magnetic vector fields operate and they are used in the reconstruction of the final image of the sample.

The spherical harmonic excitor fields SH $m = 1, n = -1$ and SH $m = 1, n = 1$, commonly referred to as X Gradient and Y Gradient have projection angles of $0°, 90°, 180°$ and $270°$. The corresponding secondary magnetic field magnitude and phase differences used in the inverse radon transform in this case to reconstruct are differences (B_x and ϕ_x) along the lines $X = 0$ mm and $X = 45$ mm and differences (B_y and ϕ_y) along $Y = 0$ mm and $Y = 45$ mm. For the two other spherical harmonics SH $m = 2, n = 0$ and SH $m = 2, n = 2$, the field and phase differences caused by those spherical harmonics are considered from different measuring points from the lines. The inverse Radon transforms and the reconstructions are executed using MATLAB.

Figures 3.17 and 3.18 show the reconstructed images based on secondary magnetic field magnitude and phase differences, when they are considered as linear projections produced by various spherical harmonics. The SH $m = 1, n = -1$ and SH $m = 1, n = 1$ fields account for $0°, 90°, 180°$ and $270°$, while the addition of SH $m = 2, n = 0$ and SH $m = 2, n = 2$ account for the projections from angles $45°, 135°, 225°$ and $315°$, and $60°, 150°, 240°$ and $330°$ respectively.

As can be observed from the images, the more angular projections are added, the clarity and the quality of the images increase. It can also be observed that the phase based reconstructions are more noisy than the field based reconstructions, as can be expected from the experimental results in Figures 2.20,2.21,2.22,2.23,2.24,2.25,2.26,2.27 and Figures 3.13,3.14,3.15 and 3.16. More accurate measurements of phase can help mitigate this problem and improve the quality of the image to be equivalent to that reconstructed from field differences.

The most significant difference between using Radon transform based reconstructions and using spherical harmonic based excitor fields as orthogonal reconstructions is to see how quickly and accurately the image structure can be arrived at. The ease of inverting the sensitivity matrix is high using spherical harmonic based excitor fields as all it requires is transposing the matrix since spherical harmonic fields based matrices are orthogonal. This ease is not available with Inverse Radon transforms. The quality and the size of the reconstructed images also vary accordingly.

It is currently not suitable to quantify the quality of the image reconstruction using metrics like RMS error or condition number like it was done in Chapter 2, as the reconstruction wasn't done directly using a sensitivity matrix method. Better methods to quantify the quality and the accuracy of image reconstruction using Radon transforms can be an area of further work and research.

3.7 Conclusion

The chapter explains the theory behind the use of phase differences and how they relate to the electrical parameters like conductivity and permittivity in Magnetic Induction Tomography. It further elaborates into how these results are modeled in a computational simulation using COMSOL. Further improvements can be made in terms of mesh refinement and postprocessing to improve the accuracy of phase calculations and runtime of simulations. The experimental protocol followed to measure phase differences caused by the sample is explained and the results presented. Finally, the chapter concludes with the illustration of images reconstructed using Inverse Radon Transforms, and the images from phase and magnetic field magnitude differences are compared and contrasted with each other. Methods to improve phase based image reconstruction are also suggested to ensure better quality of images.

Chapter 4

Magnetic Induction Tomography of Low Conductivity Materials using Optically Pumped Magnetometers

4.1 Overview

The chapter begins with a brief introduction to quantum sensors, their role and use in magnetometry and presents their advantages in use in Magnetic Induction Tomography and how it helps in characterizing and measuring low conductivity materials. It delves into the kind of quantum sensors that can be used to detect ultra low magnetic fields, and how optically pumped magnetometers can measure those fields within a shielded environment.

It further elaborates how low conductivity samples are prepared for measurements and how the experimental setup to perform Magnetic Induction Tomography on low conductivity samples is built within a magnetic shield. It presents how an excitor coil can be used to induce eddy currents within low conductivity samples ($0 - 3$ Sm^{-1}). It talks about the control systems for quantum sensing and how these integrate the optically pumped magnetometer to be used for measurements. It further explains how canceling fields are used to null the effects of the excitor field upon the optically pumped magnetometer so that sensitive measurements are made possible.

The chapter also presents the experimental protocol used to measure the magnetic fields, including how eddy current induced magnetic field measurements are made using optically pumped magnetometers. It showcases the results obtained from measured magnetic fields and interprets the results. Further possibilities of how quantum sensing and optically pumped atomic magnetometry can be used to measure magnetic fields from materials of even lower conductivity using Magnetic Induction Tomography.

4.2 Introduction

There have been multiple methods used within Magnetic Induction Tomography techniques to measure materials of low conductivity, which includes quasi insulators like biomedical tissue, fresh water and saline, plastic and wood based material defects and food materials like fruit and agar. Some of the known methods for measuring low conductivity objects include increasing the frequency of the excitor magnetic fields and improving the excitor current used to improve the primary magnetic fields. These conventional techniques aim to induce a stronger secondary

magnetic field. The strength of the secondary magnetic field response is dependent upon the magnetic field strength of the primary excitor field and the skin depth to which the eddy currents penetrate. By increasing the excitor current, a stronger primary field response is generated which in turn increases the secondary field response. The increase in frequency leads to increased electric field according to Faraday's laws, whic generate stronger eddy currents of greater current strength and that in turn improves the strength of the secondary magnetic field response.

More recently, advances in quantum technologies enable and help measurement of weak and ultra low magnetic fields using specific sensors like optically pumped magnetometers or nitrogen vacancies in a diamond, SQUIDs (Superconducting Quantum Interference Devices) or SERF (Spin Exchange Relaxation Free) magnetometers. These magnetometers are extremely effective in measuring ultra low magnetic fields as their sensitivity is in the order of a few femtoteslas (fT), unlike classical magnetometers like electromagnetic coils, Hall effect based probes or fluxgate magnetometers. The sensitivity of SQUID magnetometers is between $1 - 10$ fT/$\sqrt{\text{Hz}}$ [114], while that of SERF or atomic magnetometers, including Optically Pumped Magnetometers is in the order of 15 fT/$\sqrt{\text{Hz}}$ to 1 pT/$\sqrt{\text{Hz}}$ [115]. Nitrogen vacancy based diamond magnetometers have a slightly higher sensitivity in the order of 170 pT/$\sqrt{\text{Hz}}$ to 1 nT/$\sqrt{\text{Hz}}$[116] [117]. This is the case of quantum magnetometers while classical magnetometers like fluxgate magnetometers have higher sensitivities. Their sensitivity is in the order of 6 pT/$\sqrt{\text{Hz}}$ to 60 μT/$\sqrt{\text{Hz}}$ [118]. Hall effect magnetometers have a sensitivity range of 2.5 nT/$\sqrt{\text{Hz}}$ to 0.1 μT/$\sqrt{\text{Hz}}$. Coils and induction sensors are used in the range of 1 μT/$\sqrt{\text{Hz}}$ [119] to 0.1 mT/$\sqrt{\text{Hz}}$ [120]. This approach of using quantum sensors or atomic magnetometers can prove to be significant and vital when it comes to performing Magnetic Induction Tomography on insulators and low conductivity materials.

4.3 Theory

4.3.1 Need for the use of Ultra Low Field Magnetometers in Magnetic Induction Tomography

Magnetic Induction Tomography works on the principle of inducing eddy currents within samples, measuring them and using these measurements for imaging and characterization of the samples. Physical properties like conductivity and permeability determine the skin depth which is crucial in knowing the extent to which the primary magnetic fields penetrate the surface of the sample. The eddy current strength or the eddy current density depends on these parameters as well, and having a stronger eddy current induced within the sample or the region of interest directly correlates to having a stronger eddy current induced secondary magnetic field. The secondary magnetic field strength is given by the Helmholtz equation as mentioned in Chapter 2. The skin depth of the overall system of Magnetic Induction Tomography also significantly varies, if it is a system comprised of multiple objects with different, varying conductivity. It is also dependent upon the frequency, as mentioned in Chapter 2, with lower frequencies being able to penetrate the sample further. Skin depth and frequency of operation are inversely proportional, as shown in Figure 2.12. Higher frequencies can have an increased secondary field response, but using higher frequencies will ensure that the primary field and the subsequent electromagnetic waves generated will not be able to penetrate the entire depth of the region of interest as the skin depth becomes shorter. Thus, there is a trade-off between wanting to image or characterize a larger amount of area within the region of interest and having a stronger secondary magnetic field response, and a balance needs to be achieved between the two.

All these physical parameters like electrical conductivity, permeability and the frequency of the Magnetic Induction Tomography determine the eddy current strength, which, in turn, influences the secondary magnetic field that is detectable and measurable by sensors. The inverse relationship between the frequency of the excitation system and the skin depth of the sample also plays a key role in the strength of the induced secondary magnetic field.

In Chapters 2 and 3, metallic objects were used as samples to be imaged and have eddy currents induced within them. The sample used was copper, which has an electrical conductivity of 5.9×10^7 Sm^{-1}. But, if Magnetic Induction Tomography is to be performed on insulators, better mechanisms are to be developed that can help detect and measure magnetic fields of low magnitude on the orders of a few picoteslas (pT). Quantum sensors are capable of detecting all the way down to femtoteslas (fT) with a very high sensitivity. Materials and objects of electrical conductivity within the range of $0 - 10$ Sm^{-1} generally fall in this category and detecting and imaging them through Magnetic Induction Tomography has immensely valuable applications in multiple fields like biomedical imaging [22][29][30][31][32][33][34][35][36][121], geophysical modeling [41] and imaging, non-destructive testing [98][37], structural engineering [38] [39] and food quality inspections [44][45][46].

4.3.2 Quantum Sensors and Atomic Magnetometers

The Zeeman Effect and Magnetic Field Measurement

Quantum sensors are devices that seek to sense or measure changes in physical properties based on atomic transitions, which are considered a part of broader quantum technologies. Magnetometers that are capable of measuring ultra low magnetic fields operate on the principle of using Zeeman transition and splitting to sense changes. The Zeeman splitting of energy levels or transition is caused when a magnetic field is incident upon an atom or a molecule. The magnetic field that is sought to be measured changes the energy levels. Accurate measurement of the frequency of the Zeeman transitions can be used as a way to precisely sense and measure the magnetic field that is incident upon it. The Larmor frequency of the atom used presents a way to measure the external magnetic field.

$$\omega = \gamma B \tag{4.1}$$

$$B = \frac{\omega}{\gamma} \tag{4.2}$$

where ω is the Larmor frequency, γ is the gyromagnetic ratio and B is the imposed static magnetic field.

By measuring the Larmor transition frequency, the external magnetic field can be measured.

Chip Scale Atomic Magnetometers

There are multiple methodologies by which atomic devices or quantum technologies can be realized [122]. Alkali vapour cells play a crucial role in creating quantum sensors that are used to measure time, frequency, magnetic fields and electric fields accurately. The advancements in manufacturing technologies have enabled the creation of multiple generations of alkali vapor cells that form the workhorse of the quantum sensor.

Initially, alkali vapor cells were used as clocks, magnetometers and gyroscopes. In general, alkali metal atoms are used in manufacturing atomic and quantum devices as the presence of the valence electron makes it easy to manipulate the energy levels of the atom. The first iteration of atomic devices was manufactured using micromachining, where alkali metal vapours like rubidium (Rb) and caesium (Cs) are fabricated into vapour cells using Pyrex glass and glass blowing techniques [123] [124]. MEMS (Micro Electro Mechanical Systems) were used to develop the next version of atomic devices. In this approach, fabrication is performed by combining mechanical and electrical systems at a micro level, combining the processes of deposition, lithography and etching to create the required device. The final version of scaling up atomic devices and quantum technologies would be to fabricate them into a chip [125], consisting of the cold atom gas and the control electronics required combined together, making it easy for large scale mass manufacturing [126] [124]. Magnetic Induction Tomography has been performed [23][28] and imaging of structural defects [25][26][27] has been done by using such chip scale atomic devices.

4.3.3 Optically Pumped Magnetometers

Working Principle of Optically Pumped Magnetometers

Optically pumped magnetometers are a subcategory of chip scaled atomic devices, that function on the principle of Zeeman splitting. Optical pumping is the phenomenon by which the atomic spin of the alkali metal within the vapor cell is manipulated in order to measure the incident ultra low magnetic fields [127].

SERF(Spin Exchange Relaxation Free) Regime

Optically pumped magnetometers operate within the SERF(Spin Exchange Relaxation Free) regime. In order to use the Zeeman effect in sensing and metrology, it is required for the alkali metal vapour present within the vapor cell to be in the hyperfine state. Measuring the frequency shift between Zeeman transitions in the presence of the field to be measured when the alkali metal like Rubidium or Caesium is in the hyperfine state gives a precise measurement of the strength of the field present [128].

Spin Exchange is an interaction mechanism present within alkali metal vapor where due to the collision of the atoms, the spin of the atoms get reversed. These interactions conserve the angular momentum of the colliding atoms, but the hyperfine state of the atoms undergoes decoherence. Hyperfine states precess in opposite directions due to spin exchange collisions. SERF (Spin Exchange Relaxation Free) magnetometry is a method in which spin exchange collisions are avoided, in order to ensure the alkali atoms stay in the hyperfine state to measure the incident magnetic fields accurately using Zeeman effect.

The SERF regime is achieved by trying to eliminate or limiting spin-exchange collisions. It is achieved by increasing the density of the alkali-metal vapor present within the vapor cell and by operating in a low magnetic field, which is achieved by the use of magnetic shielding [129]. The SERF magnetometers run the risk of being saturated when operated in a higher magnetic field range.

Working Mechanism of Optically Pumped Magnetometers

An optically pumped magnetometer consists of three parts - i) A laser source, ii) A vapor cell containing an alkali metal atom gas and iii) A detection system consisting of a photodetector.

The alkali metal atoms present within the vapor cell have magnetic moments. In their normal state, the magnetic moments of the alkali metal atoms are aligned in random directions. The laser source, known as the pump, injects a circularly polarized laser light upon the alkali metal atoms present within the vapor cell. The atoms become polarized and aligned, with their spin pointing towards a particular direction. This procedure happens before the magnetometer can start sensing the required magnetic field that is sought to be measured. Once the alkali metal atoms are saturated with their spins aligned, the photodetector, in the form of a photodiode, measures the intensity or the amount of photons incident upon it [127].

When the external magnetic field that is to be measured is incident upon the vapor cell and the cold atom clouds within it, the alignment of the polarized alkali metal atoms is changed by it. The alkali metal atoms undergo a Zeeman splitting or a transition when the magnetic field to be measured is incident. This, in turn, increases the ability of the atoms to absorb the incident laser photons upon them. The photodetector system that keeps monitoring the intensity of the circular polarized laser now starts measuring a drop in the intensity of the incident laser from the source. This reduction in intensity is directly proportional to the magnitude of the magnetic field that is incident upon the vapor cell. This is the working principle of an optically pumped magnetometer that is used to measure ultra low magnetic fields that are incident upon it. The alkali metal atoms roughly act as a magnetic compass that moves according to the magnitude and the direction of the incident magnetic field to be measured.

The above mentioned is the common constructional design of an optically pumped magnetometer. In some other designs, a probe laser is used along with a pump laser as part of the photodetection system, to measure the intensity of the absorbed photons.

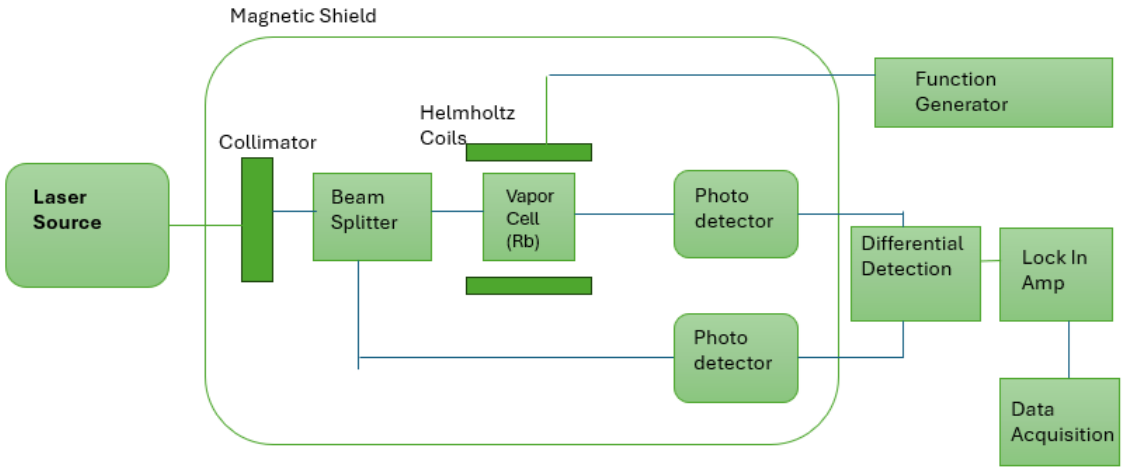

Figure 4.1: Block Diagram of a SERF optically pumped magnetometer

Figure 4.1 presents the block diagram of a differential detection mechanism of a SERF optically pumped magnetometer [130], with the laser source, vapor cell consisting of alkali metal vapor and the photodetector forming its key components.

Advantages and Disadvantages of Optically Pumped Magnetometers

One of the advantages of using optically pumped magnetometers is that their compact size and dimensions makes sure that they are easily deployed and many channel systems can be

engineered and fabricated easily. Commercially available magnetometers are mm size and dimensions of the order $30 \times 30 \times 30$ mm.

Another primary advantage of using optically pumped magnetometers is that, unlike superconducting quantum interference devices (SQUIDs), they don't require a cryogenic cooling system. An optically pumped magnetometer can function within room temperature without the need to cool it down using liquid helium or nitrogen. They depend only upon optical pumping. The control electronics used to operate the magnetometer can be realized using Field Programmable Gate Arrays (FPGAs).

The challenge of using an optically pumped magnetometer in a particular environment is that it is extremely sensitive to noise as it has a very high sensitivity. Earth's magnetic field varies between 25 μT to 65 μT, depending upon where it is measured. It is roughly considered to be 50 μT, in many parts of the world. The earth's magnetic field and external magnetic sources including power outlets and electronic appliances can heavily interfere with and saturate the optically pumped magnetometer. In order to make the optically pumped magnetometer operational and be able to make sensitive measurements, the magnetometer must therefore be isolated and shielded magnetically. It is possible to use active and passive magnetic shielding to make optically pumped magnetometers work. In many cases, a pair of Helmholtz coils are used to cancel out external magnetic field based noise.

Applications of Optically Pumped Magnetometers

Optically pumped magnetometers have a wide variety of application in various fields. They are used in biomagnetic field measurements, magnetoencephalography (MEG) and magnetocardiography in order to image and measure magnetic fields within human anatomical organs like the brain and the heart [24] [121]. They are also used in Zero to Ultra Low Field Nuclear Magnetic Resonance (ZULF) measurements to measure chemical properties in NMR (Nuclear Magnetic Resonance) spectroscopy [131]. Structural defects within materials can be imaged using optically pumped magnetometers [23][25][26]. They are also directly used in high energy physics applications like dark matter searches and axion searches [132].

4.3.4 Skin Depth

As mentioned in Chapter 2, skin depth is given by

$$\delta = \sqrt{\frac{1}{\pi \sigma f \mu_0 \mu_r}} \tag{4.3}$$

where δ is the skin depth to which the primary magnetic fields penetrate, σ is the electrical conductivity to be measured, μ_0 is the permeability of free space and μ_r is the relative permeability of the material.

Commercially available optically pumped magnetometers (off the shelf) unfortunately do not have a large bandwidth that enables them to be used in the RF (Radio Frequency) range. They are available to be used within the low frequency range of $0 - 100$ Hz. The following is a calculation of skin depth considering a frequency of 99 Hz. The considered low conductivity range is $0 - 10$ Sm^{-1}.

From the calculations of skin depth, it can be seen that the skin depth is in the range of 20 to 40 m, and hence can penetrate the full size of smaller samples used in experiments.

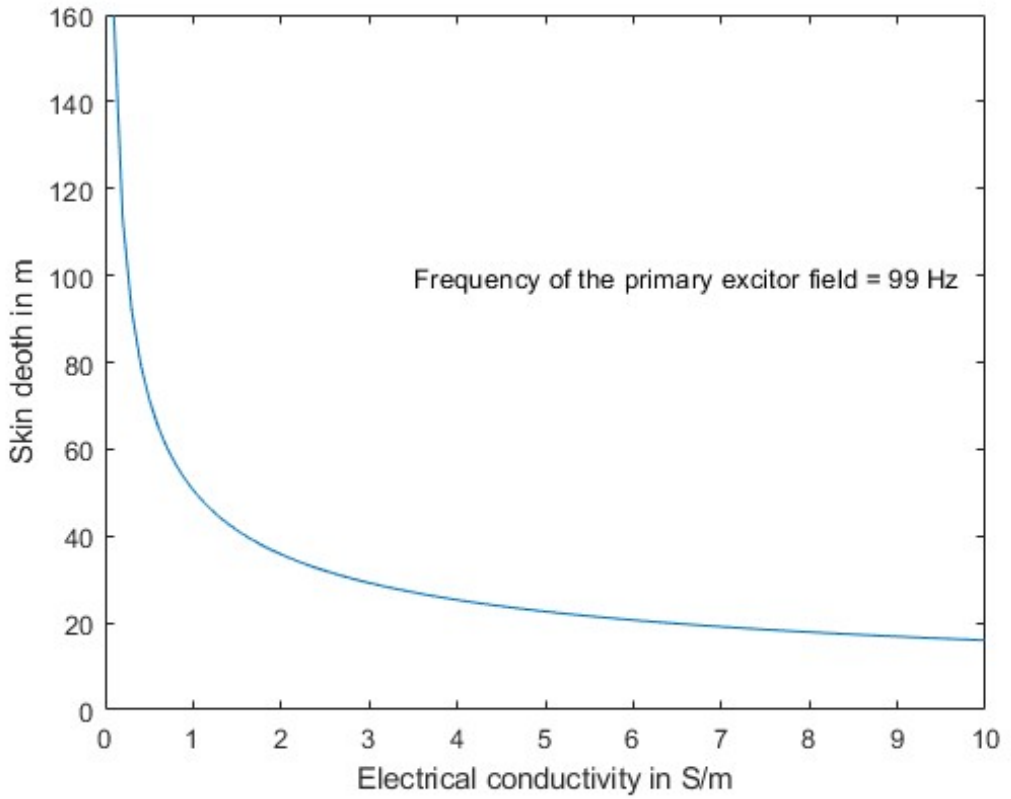

Figure 4.2: Skin depth in metres vs. Electrical Conductivity in Sm^{-1}

4.4 Initial Computational Simulations

Some initial computational simulations were done using COMSOL, to calculate the range of eddy current induced secondary magnetic fields within low conductivity materials. The simulation procedure is exactly the same as described in Chapter 3.

The simulation setup consists of a single excitor coil as described in Chapter 3, and a sample cube of size $10 \times 10 \times 10$ mm. The electrical conductivity of the sample is chosen to be 10 Sm^{-1} and it is placed at a distance of 20 mm from the excitor coil. The amount of electric current used in the simulation is 4 mA.

The results of the simulation and the magnitude and the phase of the magnetic field calculated are presented in Figures 4.4 and 4.5. The measurement line is at a distance of 60 mm from the excitor coil, marked in red in Figure 4.3. The simulation measures the same vector field component which is measured by the optically pumped magnetometer in the experiment described in Section 4.5, given by X in this figure. It is found at a line close to the 0.05 m mark along the axis in Figure 4.3. From the simulation, it can be learnt that the secondary magnetic field to be measured is in the order of $0.01 - 0.5$ nT (a few hundred picoteslas), for the range of low conductivity ($0 - 10$ Sm^{-1}) that is to be investigated. The phase of the magnetic field is in the range of -6×10^{-5} to 6×10^{-5} radians. Figure 4.4 shows the secondary magnetic field calculated for the setup in Figure 4.3. The simulations were carried out to determine the range of the secondary magnetic fields to be detected and pick the right kind of the sensor with appropriate levels of sensitivity. From the simulations, it can be seen that for the given range of conductivity, the secondary magnetic field induced could be detected using an optically pumped magnetometer. The simulations are performed just as an assessment to check

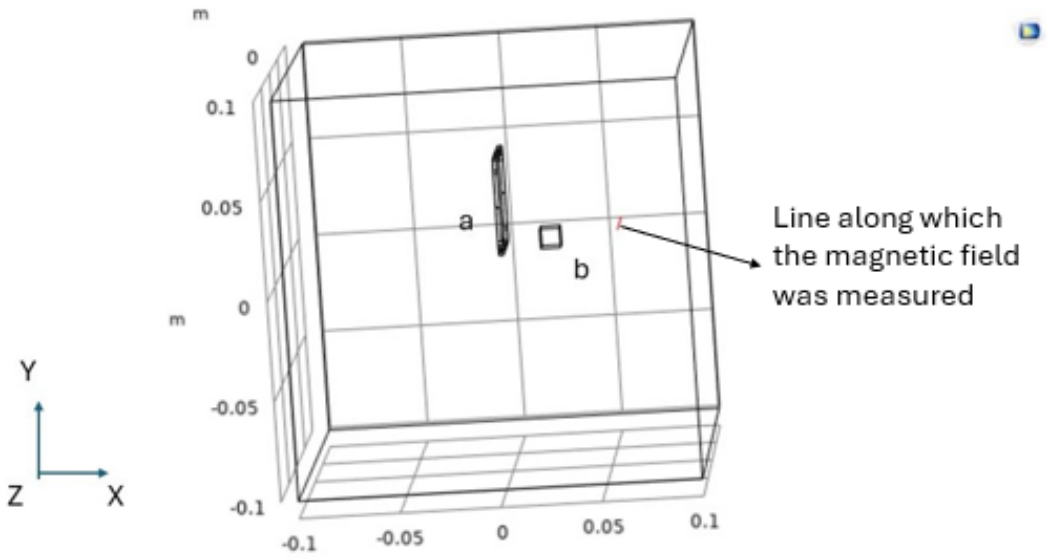

Figure 4.3: Simulation with a) a single excitor coil on b) a low conductivity material

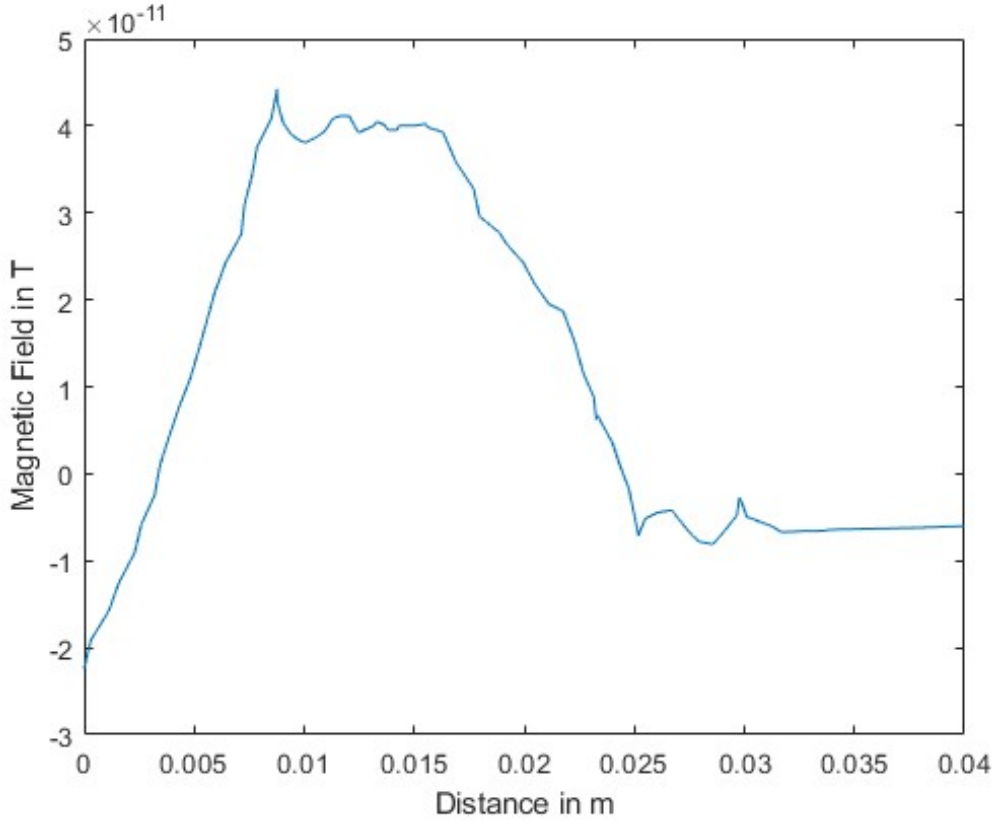

Figure 4.4: Secondary Magnetic Field in T vs. Distance in m

the range of induced secondary magnetic fields. It is obvious that based upon the skin depth calculations and the level of sensitivities required to detect the low conductivity materials, an optically pumped magnetometer would prove to be a perfect and an efficient fit, to sense and measure ultra low magnetic fields in Magnetic Induction Tomography measurements. Hence, it is to be used in the experiments to measure and characterize low conductivity materials.

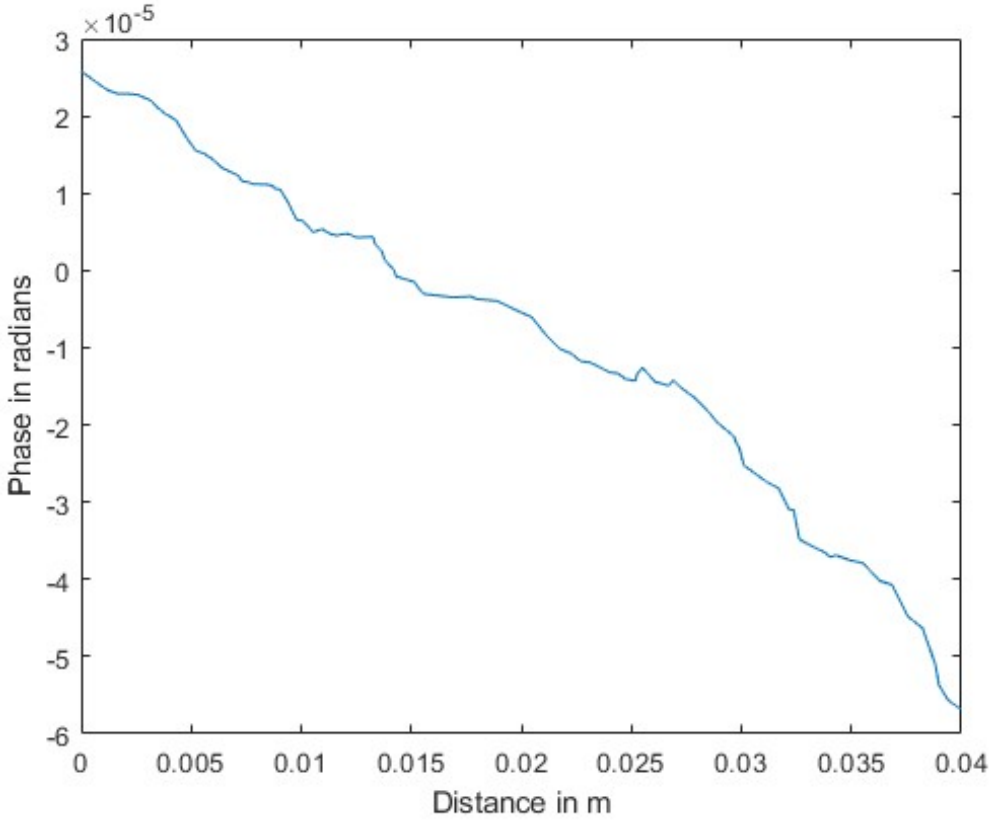

Figure 4.5: Phase Difference between magnetic fields in radians vs. Distance in m

4.5 Experimental Procedures

The experiment to measure secondary magnetic fields consists of several phases. First, samples of different electrical conductivity in the required range of $0 - 10$ Sm^{-1} must be prepared with precision. An excitor coil is used to induce eddy currents within the samples. In order to make the entire setup work, it needs to be enclosed within magnetic shielding to avoid the influence of external noise and more importantly, to avoid saturating the optically pumped magnetometer. The experiment consists of a single excitor coil which is mounted on a stand within a magnetic shield with the sample placed in front of it. The shield provides the acting canceling magnetic field and nulls earth's field that cancels out the effect of the primary magnetic field upon the quantum sensor (optically pumped magnetometer). The detection system then detects the field changes caused due to the induced eddy current within the sample, which is acquired by the data acquisition system and processed.

The following are the methods and procedures that are executed the experiments in measuring the secondary magnetic field using optically pumped magnetometer.

4.5.1 Sample Preparation

In order to measure eddy current based secondary magnetic fields in low conductivity materials ($0 - 10$ Sm^{-1}), samples need to be created that fall in this conductivity range. Electrical conductivity is an intrinsic property of materials, and these materials need to be refashioned as samples to be used in the experiment. Literature suggests that the lowest conductivity measured using Magnetic Induction Tomography so far is 3.8 Sm^{-1} [133]. So, the target for sample preparation and the overall experiment is to reach conductivity levels that are lower

than the present measured conductivity ($0 - 3$ Sm^{-1}).

Insulators usually fall within the required range of conductivity of $0 - 10$ Sm^{-1} and they are chosen for this purpose to be used for sample preparation. Polymers like polyethylene or glycol generally have electrical conductivities of this order. There are multiple plastics and polymers that fit the requirements. Many biomedical tissues and cells and food materials also have a range of conductivity of $0 - 3$ Sm^{-1}.

Initially, graphite is considered as a suitable material for preparing the required samples of low conductivity. The electrical conductivity of a material is given by

$$\rho = \frac{RA}{l} \tag{4.4}$$

$$\sigma = \frac{1}{\rho} = \frac{l}{R\nu} \tag{4.5}$$

where ρ is its electrical resistivity, σ is its electrical conductivity, R is the resistance of the material, l is the length of the material and ν is its surface area. Graphite from artist's charcoal can be remade into smaller samples, with its resitance measured using a multimeter set to resistance mode. The measured resistance can be then be used to calculate the sample's electrical conductivity. This approach produces only samples of electrical conductivity of 8.1 Sm^{-1}. Moreover, it doesn't provide a granular or fine control over changing the electrical conductivity of the sample.

Saline water (solutions of salt dissolved in distilled water) provide better control over electrical conductivity within the low conductivity range, and prove to be better and more efficient samples that can be used in eddy current induced secondary magnetic field measurements. By increasing or decreasing the amount of salt ($NaCl$) dissolved in a specific volume of water, the conductivity of the saline solution could be changed with a resolution that can be calculated.

The conductivity of the saline solution is determined and calculated using the total amount of dissolved solids and the mass of the salt dissolved. It is modeled as a linear relationship between the electrical conductivity and the amount of substance dissolved in the saline solution, within the range of conductivity explored [134]. The relationship is given by

$$\sigma = KC \tag{4.6}$$

where σ is the conductivity, K is the proportionality constant and C is the concentration of the saline solution, dependent upon the total amount of dissolved solids in the solution. Based upon previous literature, the proportionality constant K is calculated to be 0.0039 $Slmg^{-1}m^{-1}$.

The electrical conductivity has a temperature dependence, especially in the low conductivity regime. The conductivity of the saline solutions calculated is considered to be at room temperature conditions (25°C). The relationship between electrical conductivity at room temperature and electrical conductivities in other temperatures is determined by a temperature compensation factor [135]. The relationship between electrical conductivities across multiple temperatures is given by

$$\sigma_T = \sigma_{25}[1 + a(T - 25)] \tag{4.7}$$

where σ_T is the electrical conductivity of the sample at temperature T, σ_{25} is the electrical conductivity at 25°C, a is the temperature compensation factor and T is the temperature of the sample at which the conductivity is to be measured in °C. While changes in temperature affect the electrical conductivity, the temperature of the experimental environment is maintained at a constant to ensure it doesn't have a bearing upon the samples. It is ensured that the samples continue to remain at a constant temperature as well. The temperature within the shielded environment was measured regularly to ensure that the temperature remains close to the room temperature. Electronic control systems and optically pumped magnetometers were used intermittently in a manner in which their operation doesn't increase the temperature of the shielded environment. When the optically pumped magnetometers or other electronic devices get heated up, the shieling environment is air cooled by opening it up. The insulation provided around the magnetometer is also helpful in reducing the temperature. The trial of the experiment and the measurements were done in such a manner that the increased temperature of electronics and optically pumped magnetometers doesn't affect the sample.

Multiple samples are prepared by dissolving a particular amount of salt in a constant volume of distilled water and creating an electrolytic saline solution. A cylindrical glass sample holder, of dimensions of height 5.2 cm and radius 2.5 cm, is used to hold the saline solution samples. Borosilicate glass is chosen because it doesn't interfere the excitor based primary magnetic fields. Five different samples of different concentrations and total dissolved solids are prepared by dissolving five different concentrations in 15 mL of distilled water. The concentrations and the corresponding electrical conductivities are mentioned below in the table.

Total volume of water = 15 mL	
Concentration of salt in mL	Electrical Conductivity in Sm^{-1}
51	0.2
87	0.35
157	0.61
204	0.8
737	2.9

These samples are used as phantoms in Magnetic Induction Tomography to represent the low conductivity regime.

4.5.2 Magnetic Shielding

One of the key challenges of using quantum sensors is that their sensitivity is very low compared to classical sensors, in the order of a few femtoteslas ($\leq$ 15 fT). This level of sensitivity means that the sensor picks up magnetic noise from the external environment, including earth's magnetic field, power outlets and mobile phone signals. This external noise disturbs the sensitive measurements of low magnitude magnetic fields like neuron signals in Magnetic Resonance Imaging and eddy current induced magnetic fields in Magnetic Induction Tomography. Another huge disadvantage with bringing quantum sensors to use in a magnetically noisy environment is that the sensors get saturated and fall out of operating range, which is typically between -5 nT to 5 nT.

In order to ensure that the optically pumped magnetometer or any type of quantum sensor remains operational, it needs to be shielded so that it can avoid external noisy magnetic fields. There are some mechanisms by which it can be made to be functional in an unshielded

environment, but it compromises on the accuracy of magnetic field measurements. This experiment shields the optically pumped magnetometer to accurately measure the required secondary magnetic fields.

There are two ways in which magnetic shielding is achieved and incorporated around the sensor - i) passive shielding and ii) active shielding. The idea of passively shielding a quantum sensor is to use a magnetic shield made of high permeability material like Mu-metal, which has a relative permeability in the range of 80000 to 100000. The shield can be manufactured in various configurations and dimensions and used to enclose the sensors in a low field within their operational range.

Active shielding on the other hand uses a power source, electromagnetic coils like a Helmholtz pair of coils to cancel out the effects of external noisy magnetic fields upon the sensor. There are coils of different dimensions that can be used to achieve a lower noise based configuration within the sensor by using coils within a closer proximity. The primary difference between active and passive shielding is the use of a power source that uses active supplied currents to cancel out external noise, whereas passive shielding does not require that. An active approach allows for real time compensation of fields depending upon the change in the frequencies of noisy external fields and expands out the range of frequencies that can be blocked by the active use of a control system.

Magnetic shielding works based upon the principle of keeping the magnetic flux lines out of the target area. The magnetic flux lines are attracted or rerouted by the presence of high permeability material and the magnetic flux tends to follow the path of least magnetic reluctance. By taking advantage of material properties and structural design of the magnetic shields designed, the magnetic field lines and the magnetic flux that seek to penetrate are kept out of the region of interest that is to be shielded. Active shielding uses current sources to create a magnetic field in the opposite direction, thereby cancelling out the penetrating shield lines.

There are also hybrid approaches that are possible in magnetic shielding, which tries to combine advantages of both types of shielding. Such systems typically use constant field Helmholtz coils and first and second order gradient coils to cancel out the stray fields and are enclosed within a mu-metal shield to make use of its high relative permeability.

Our experiment uses a hybrid, benchtop magnetic shield known as the GA-4 [136] [137], manufactured by Magnetic Shields Limited, which is specially designed for atomic magnetometry usage and shielding. The shield is cylindrical in shape and is made of mu-metal which acts as a passive shielding system. It consists of four mu-metal nested cylinders, with the outer radius of the shield being 150 mm and the inner radius being 100 mm. The length of the outer cylinder is 480 mm, and the length of the inner cylinder is 300 mm. There are nine PCB (Printed Circuit Board) coils within the shield, that provide the required compensation fields to actively perform noise cancellation. The nine coils that generate the cancellation target fields are - 3 uniform fields along three directions (B_x,B_y,B_z), 5 linear gradient fields ($\frac{\partial B_x}{\partial x}, \frac{\partial B_y}{\partial x}, \frac{\partial B_x}{\partial z}, \frac{\partial B_y}{\partial z}, \frac{\partial B_z}{\partial z}$) and 1 second order gradient ($\frac{\partial^2 B_z}{\partial z^2}$), where Z is the shield's cylindrical symmetry axis. The coils could be used to create the required target fields to cancel out the external noise.

The shielding efficiency, SE, of a magnetic shield is defined by the ratio of the magnitude of measured magnetic field at a point in an unshielded environment to the magnitude of the

measured magnetic field at the same point within the shielded environment.

$$SE = |\frac{B_{unshielded}}{B_{shielded}}| \tag{4.8}$$

The shielding efficiency of the GA-4 shield along the axial direction is between 1×10^6 to 4.5×10^6, while the shielding efficiency along the transverse direction is 20×10^6 to 39×10^6 [136].

The experiment is conducted in the central part of the inner cylinder where the shielding efficiency is optimized with accurately achievable target fields and the influence of external noise magnetic fields is minimal.

4.5.3 Optically Pumped Magnetometers in experiment

As explained in Section 4.3.3, optically pumped magnetometers are atomic magnetometers that work based on the principle of Zeeman splitting and polarized magnetic moments of alkali metal atoms to measure ultra low magnetic fields incident upon them.

There are multiple commercially available optically pumped magnetometers like Twinleaf and Fieldline. The sensor chosen for the experiment is the Quspin Gen-2 Zero Field Magnetometer (ZFM) [138]. The sensor uses rubidium (Rb) vapor atoms as alkali metal sensing element to sense and measure magnetic fields.

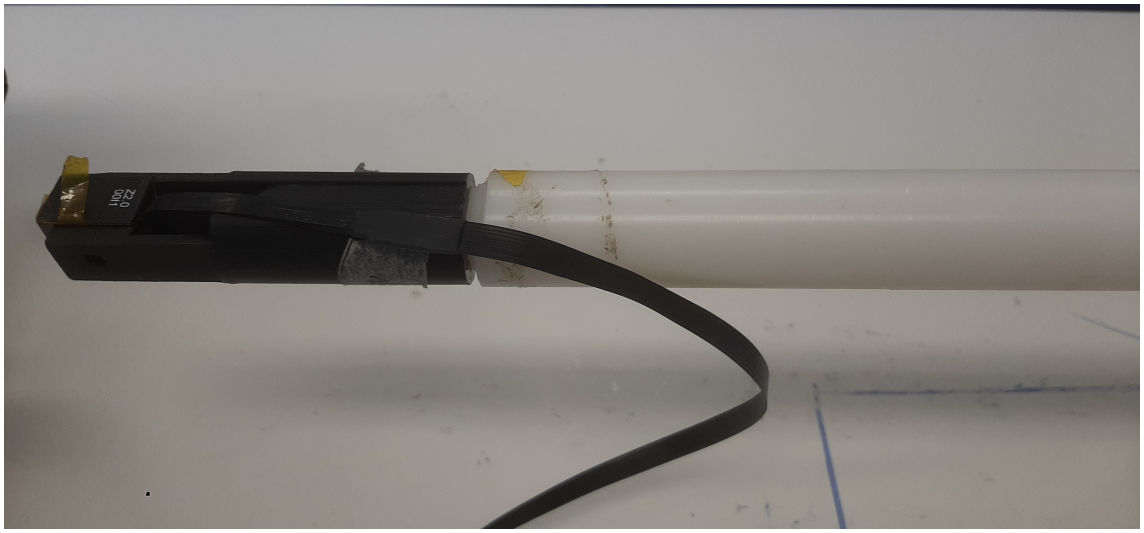

Figure 4.6: QuSpin Zero Field Magnetometer

Optically pumped magnetometers are of two types - i) Zero Field Magnetometer and ii) Total Field Magnetometer [139]. Zero field magnetometers have a smaller dynamic range, can make extremely highly sensitive measurements and are used in biomagnetic measurements. Total field magnetometers have a larger dynamic range, being resistant to noise from orthogonal axes and directions, and are hence used in geomagnetic measurements and applications where a larger range is required. This experiment uses a zero field magnetometer as the eddy current induced secondary magnetic fields are on the same range as biomagnetic fields. The magnetometer used is a Gen 2 Zero Field Magnetometer.

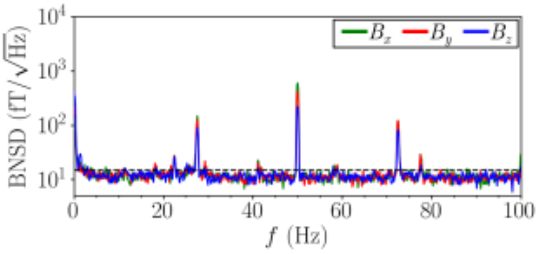

(a) Magnetic Noise Spectral Density present within an empty shield

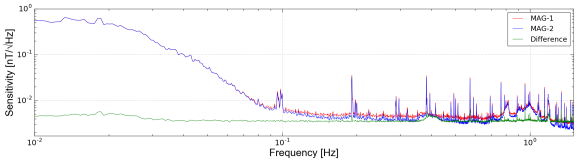

(b) Magnetic Power Spectral Density measured using two Quspin Optically Pumped Magnetometers

Figure 4.7: Magnetic Noise Spectral Density and Magnetic Power Spectral Density showcasing the bandwidth of the sensor [136][138]

The magnetometer is bi-axial with its ability to measure the incident magnetic field along two axes simultaneously. The dynamic range of the chosen optically pumped magnetometer is -5 nT to 5 nT, with a sensitivity of ≤ 1 pT/$\sqrt{\text{Hz}}$. Optically pumped magnetometers still operate only within the DC range, having a bandwidth of $0 - 100$ Hz. Given the smaller bandwidth of the optically pumped magnetometers, the experiment is designed to run at a lower frequency of 97 Hz. The development of Radio Frequency (RF) (300 Hz to 1 MHz) based Optically Pumped Magnetometers can help improve the state of play in adapting the magnetometers for use in Magnetic Induction Tomography. RF OPM magnetometers [140] [141] would help detect secondary magnetic fields in an efficient manner as higher frequencies induce stronger eddy currents.

Figure 4.7 presents the magnetic noise spectral density [136] measured within an empty magnetic shield. It also presents the magnetic power spectral density which showcases the bandwidth of the sensor [138].

There are two Helmholtz coils next to the vapour cell containing rubidium atoms on board the chip package, which are used to do initial noise cancellations. Further developments using the coils are possible which could be used for adaptive noise control, implementing a control system which could change the amount of current strength supplied to the Helmholtz coils.

The magnetometer also uses a plug and play connection system, which makes it easy to be controlled, positioned within a magnetic shield and be put into use for measurement. The sensor is integrated with a FPGA (Field Programmable Gate Array) control box, and then it is calibrated and controlled using LabVIEW. It is mounted on a stand and a longer translational stage along Z axis and a shorter translational stage along Y axis.

4.5.4 Excitor Coil and Experimental Setup

The excitor coil used to produce primary magnetic fields is the same as the one used in Chapter 2 and Chapter 3. It is a square coil with dimensions $50 \times 50 \times 2$ mm. A single coil is mounted on an additively manufactured stand, that also provides for it to hold the sample container at a constant distance from the excitor coil and the sensor, mounted on two translational stages. The entire setup, consising of the excitor coil along with the sample, is attached together to the GA-4 magnetic shield using 5 mm insulator plastic screws so as not to interfere magnetic measurements. A block diagram of the setup is found in Figure 4.8.

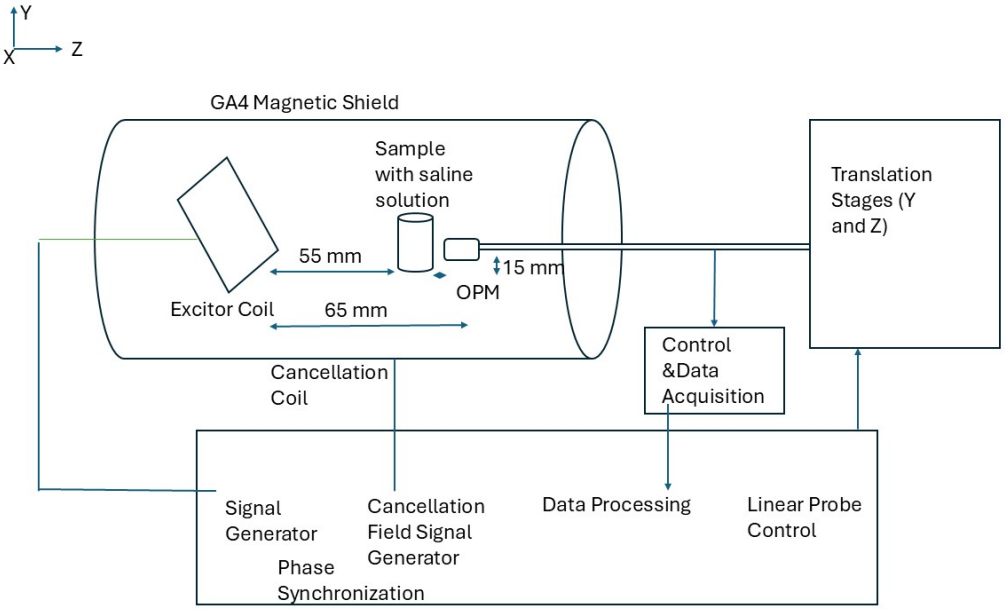

Figure 4.8: Block Diagram of Experimental Setup

The optically pumped magnetometer is placed on a custom designed additively manufactured sensor holder, and a printed sensor attacher is used to attach it to the translational stage. The sensor is placed and positioned in such a way through both the translational stages that it can be placed adjacent to the sample to sense the secondary eddy current induced magnetic fields. It can also be retracted from the same position to make room for the samples to be changed. The sensor holder from the translational stage extends in through the central hole provided within the GA-4 magnetic shield. The longer translational stage can move through a range of 300 mm, while the shorter probe moves for 50 mm.

The excitor coil is placed at the centre of the GA4 shield, at an optimal location to ensure the remnant magnetic field from the external noise sources remains low and minimal. The sample holder is placed at a distance of 55 mm away from the coil, while the sensor is placed at 10 mm further away from the sample along Z axis. The sensor is at 65 mm away from the excitor coil along Z axis and is placed at a height of 15 mm from the floor of the sample holder. The idea of placing the sensor at a height of 15 mm is to ensure that the secondary magnetic fields from the saline solution can be measured effectively. The sensor is directly parallel to the symmetry axis of the cylindrical magnetic shield and the air or vacuum within the sample holder is avoided.

One of the key challenges of using optically pumped magnetometers or any kind of quantum sensors in Magnetic Induction Tomography is that the primary field that is required to induce eddy currents sometimes overpowers the sensor, falling out of the dynamic range of the sensor, saturating the sensor. In applications like magnetoencephalography (MEG), the ultra low magnetic fields are detectable and measurable relatively easily as they don't require a primary magnetic field to be induced. Whereas, in Magnetic Induction Tomography using quantum sensors (MIT), the role that the primary field plays is a significant one.

The primary field needs to be in the optimal range in order to be able to make Magnetic Induction Tomography work using optically pumped magnetometers. It needs to be large enough such that it induces eddy current based induced secondary magnetic fields, yet small

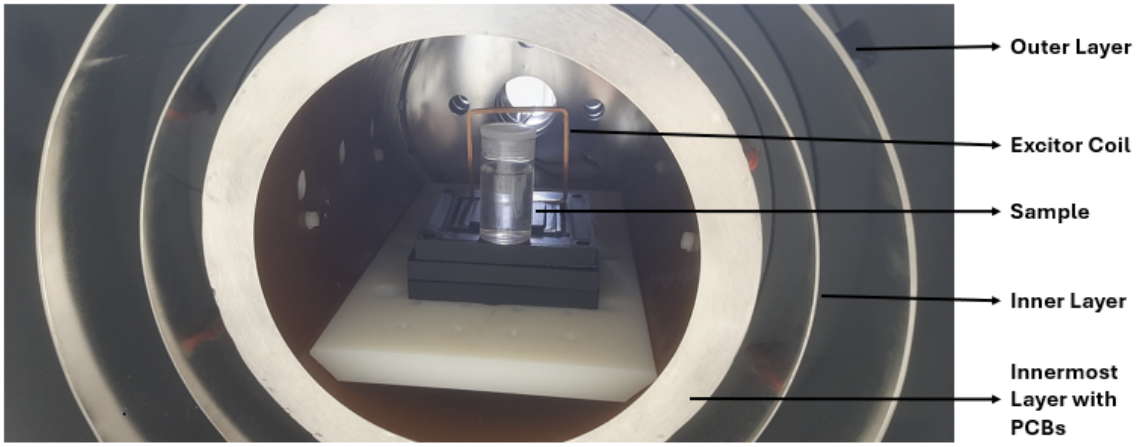

Figure 4.9: Excitor Coil and Sample within the magnetic shield

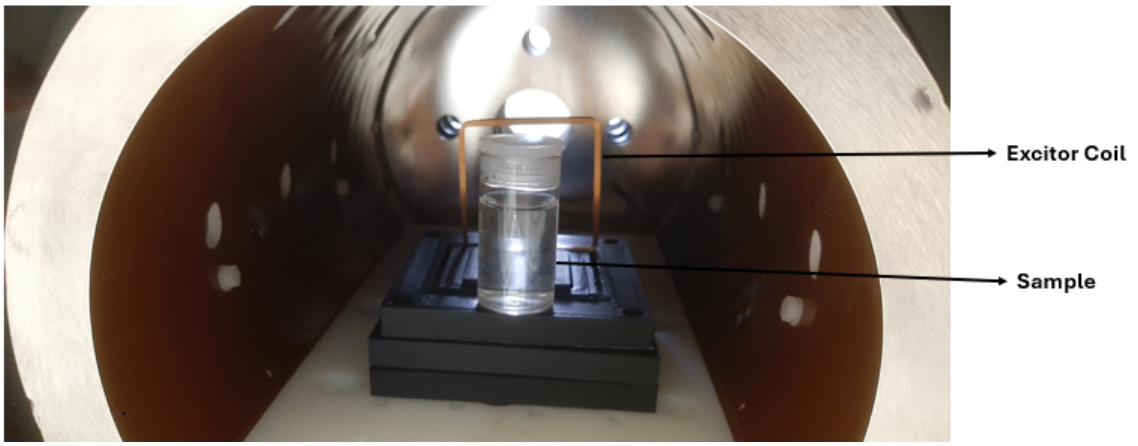

Figure 4.10: A closer version of the setup in Figure 4.9

enough so that it can be easily cancelled, ensuring it doesn't affect the operations of the sensor. This provides challenges for the positioning of the optically pumped magnetometer and measurements of the fields from the sample. In some cases, an active cancellation system is used to nullify the effect of the primary field upon the sensor.

For the experiment, the cancelling field is provided by the B_z field coil present within the GA4 shield. The axial field, B_z, along the cylinder is a constant field that can be controlled by an external power source as mentioned Section 3.5.2. Two different current sources are used to control the current that are used to generate the primary magnetic field and the cancelling field.

The current sources that are connected to the excitor coil and the canceling coil within the GA4 magnetic shield are phase synchronized. Moku Go, a FPGA (Field Programmable Gate Array) based device, was used to generate the required signals that serve as a current source for both the excitor coil and the cancellation coil. The phase difference between the two signals was 180°, which meant that the effect of the primary field upon the sensor was cancelled out by the constant B_z field from the cancellation coil.

The self inductance of the excitor coil is 2.1 mH, as mentioned Chapter 2. The voltage supplied to the excitor coil is 300 mV and the potential difference used to drive the current in the cancellation coil B_z is 294 mV. The total current that induces the eddy currents within

the saline solution is equal to 4.7 mA. The magnetic field at the sample due to the excitor field is computed from the COMSOL simulation to be 8.8 μT and at the sensor, it is found to be 5.6 μT. It is preferrable to use a Hall probe or a fluxgate magnetometer that is capable of measuring in the range of microteslas, as the excitor field without the cancellation field cannot be measured using an optically pumped magnetometer as it falls out of the dynamic range of the sensor.

4.5.5 Control Systems, Data Acquisition and Low Field Magnetic Measurements

The sampling frequency of the control system used to record and acquire data is 200 Hz. Hence, the frequency at which the experiment is conducted and Magnetic Induction Tomography is performed is 97 Hz. The frequency is chosen not to be exactly 100 Hz because of a potential problem where harmonics and overtones from the AC mains outlet could interfere with the induced secondary magnetic field signals.

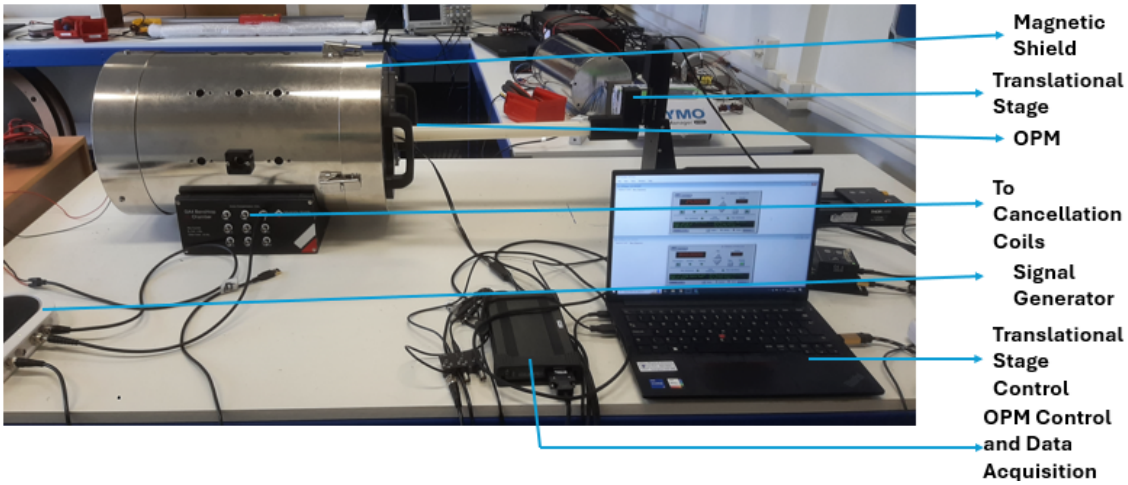

Figure 4.11: Experimental Setup with the control system

Once the experiment is set up and the sensor is positioned, it needs to go through multiple steps before it can start making sensitive measurements. The rubidium atoms are prepared using the idea of laser polarization. Once the cell temperature is locked, and it proceeds to the next step for the field to be zeroed.

Once the cell operating temperature is reached, there needs to be a laser lock. The rubidium atoms present within the vapor cell needs to be completely polarized and the detection system should be able to detect the corresponding amount of laser incident upon them. This position where the rubidium atoms are completely polarized is considered a laser lock, and it needs to be accomplished before the sensor is calibrated.

The reference for magnetic field measurements needs to be set and the remnant magnetic field at that position before the excitor and cancellation coil are supplied with current is taken to be the reference for zero. The command to execute that is provided through the LabVIEW interface from the control box.

Once the field is zeroed and the remnant field in the background is taken into account, the final calibration is done. It considers minute and sensitive variations in the magnetic field being

measured. Since it is a Gen 2 magnetometer, it measures the magnetic field along only two axes. The required control of the two translational stages along Y and Z axes is also established.

4.6 Experimental Methods and Protocols

This experiment follows the idea of differential measurements similar to Chapter 2 and Chapter 3. The idea of differential measurement is that the sensor is placed at the same point in the presence and the absence of the salt solution, and the difference measured between the two magnetic fields helps to determine the change in the electrical conductivity of the sample. The main difference between the way differential measurements were performed for metallic conductors like copper and insulators like saline solutions is the use of a similar replacement like distilled water without dissolved salt in the place of the sample to be measured. While for copper, there was no need to use a replacement given its high conductivity, it becomes essential to introduce a replacement like distilled water in the place of the saline solution in order to ensure that even tiny discrepancies don't arise because of small changes in electrical conductivity from the environment.

The experiment is performed as follows. The sample holder along with distilled water is placed at the intended location along with the excitor coil within the GA-4. The sensor is positioned at the required location using the two translational stages from Thorlabs as mentioned. The reference field of the optically pumped magnetometer is determined and the sensor is calibrated and made ready to record and acquire data. The zeroed out field is between 1300 pT to 1500 pT.

The excitor coil and the cancellation coil are both powered and supplied with current. The optically pumped magnetometer measures the data along both the axes and records it. This measurement presents the noise floor of the overall experiment. The sensor is now retracted out of the magnetic shield. The GA-4 shield is opened up and the sample holder is now taken out of the shield. It is now replaced with the sample holder solution consisting of a different concentration of salt, without disturbing the original setup. The shield is again closed up and the sensor is returned back perfectly to its original position. It is done with the help of the two translational stages that make it possible to position the sensor perfectly at the same location again.

The magnetic field is now recorded and data is acquired again. After processing the data, the difference in magnetic field measured along the axial direction is now caused by the presence of the saline solution with a concentration of total dissolved solids. This difference can be related to the electrical conductivity of the material.

The experiment is conducted for different concentrations of salt - 51 mg, 87 mg, 157 mg, 204 mg and 737 mg, and every time it is contrasted with distilled water without any salt concentration in it. Multiple trials are made for each sample. The experimental protocol is as follows. Initially, a sample with no dissolved salt is placed. Plain water is considered to be a perfect insulator with a conductivity of 0 Sm^{-1}. The excitor and cancellation fields are applied and then the magnetic field is measured. The experiment is repeated for six times to arrive at the remnant magnetic field and it is treated as the noise floor at which the remaining measurements are to be performed. The experiment is continued by placing different samples with various concentrations as mentioned above, measuring the magnetic field caused due to the difference in conductivity. The magnetic field is measured six times. It is ensured that

mechanical noise is avoided to the best possible extent by the design of the experiment and the placement of the clamped sample, as the slightest disturbance could add noise to the measurements.

4.6.1 Post Processing and Data Analysis

The obtained data is processed and analyzed in order to figure out the magnitude of the secondary magnetic fields and the difference in the magnitudes which could be correlated with the electrical conductivity of the saline solutions. The data is acquired through LabVIEW and processed in MATLAB.

Once the data is begun to be processed, the mean of the signal is subtracted from the acquired signal in order to eliminate the DC signal. It is then passed through a lowpass filter with the stopband filter as 98 Hz, with the sampling frequency being 200 Hz. This helps eliminate harmonics and enhance the signal strength of the secondary magnetic field.

After the filtering has been done, the magnitude of the secondary magnetic field is derived by using the RMS (Root Mean Square) magnitude. Statistical data like the mean of the magnitudes from multiple trials is calculated.

4.7 Results and Discussion

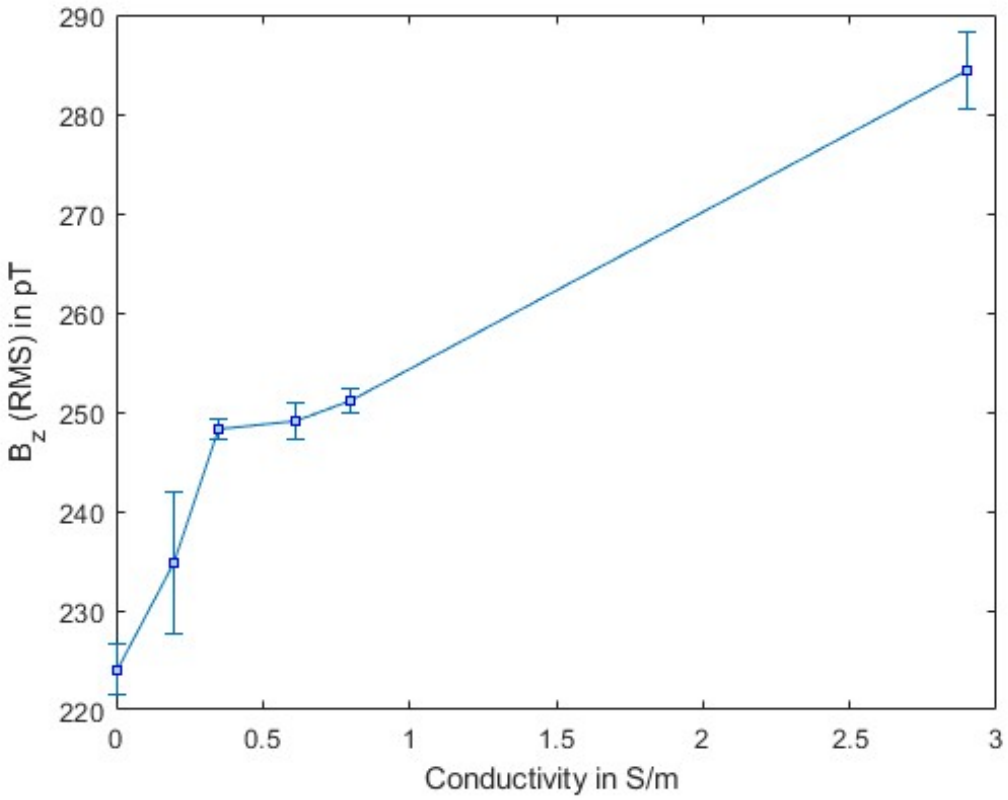

Figure 4.12: Electrical Conductivity in Sm^{-1} vs. Axial Magnetic Field (RMS) in pT (The axial magnetic field shown is the directly measured magnetic field, not the difference)

Figure 4.12 presents the experimentally measured data of six different samples with different salt concentrations corresponding to different levels of electrical conductivity. The figure does not present the difference in magnetic fields measured like in Chapter 2, but the whole measured field value. The error bar presented in the figure is a measure of the standard error collected from the dataset obtained through measurement. The distance between the sample and the sensor is 5 cm. It can be seen from the figure that the relationship follows a roughly linear trend between electrical conductivity and the magnitude of the secondary magnetic field measured by the optically pumped magnetometer. The increase in electrical conductivity due the increase in concentration of salt causes a change in magnetic field. The magnitude is presented with error bars and the varying range within which the fields lie.

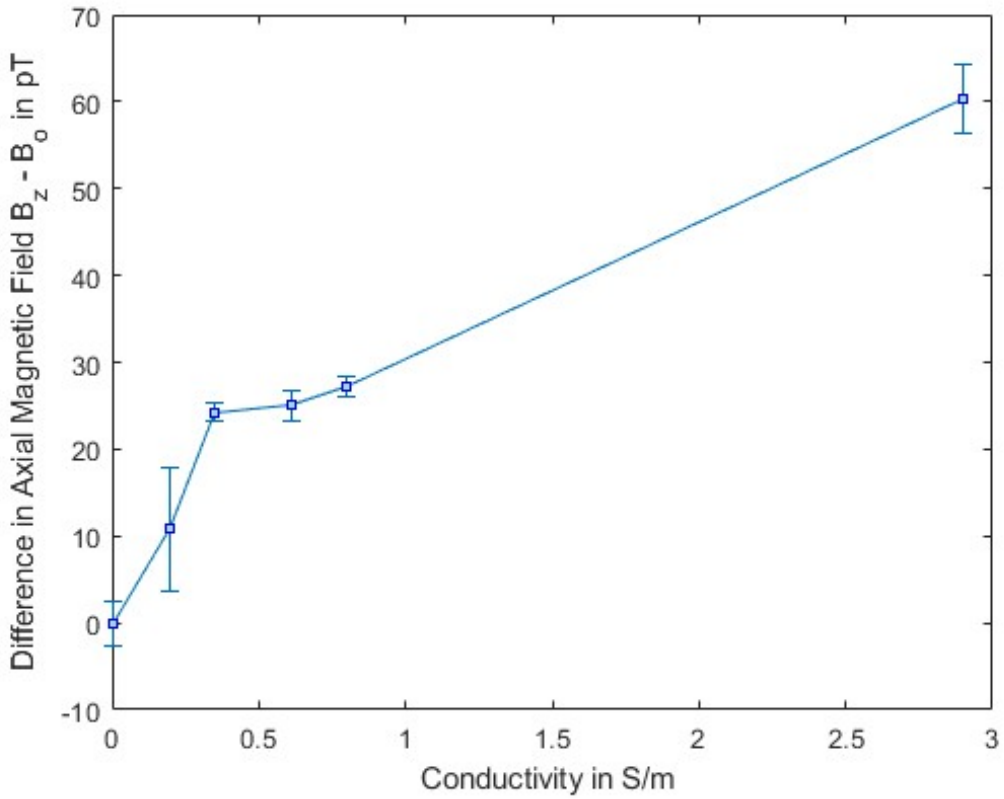

Figure 4.13: Electrical Conductivity in Sm^{-1} vs. Difference in Axial Magnetic Field $B_z - B_o$ in pT

The result assumes significance in the light of the fact that previously published literature has been able to detect and measure secondary magnetic fields from samples of electrical conductivity of 3.9 Sm^{-1}. The noise floor or the remnant magnetic field that was measured by the sensor was 224.03 pT. The noise floor, in this case, is the axial magnetic field measured by the optically pumped magnetometer when a sample containing only water without any dissolved salt is placed within the shield for it to be characterized using Magnetic Induction Tomography. The electrical conductivity of this sample is 0 Sm^{-1} and hence 224.03 pT is the least attainable remnant magnetic field using the operational frequency, the strengths of excitor and cancellation currents and the experimental setup distance. Hence it is considered the noise floor or the baseline from which other samples with different concentrations of salt are characterized. For changes in electrical conductivity, the corresponding differences indicate the change in magnitude of the secondary magnetic field. The difference in magnitude is in the range of 10 pT to 30 pT, for electrical conductivity within the range of $0 - 1$ Sm^{-1}. Figure 4.13 shows the difference

between the magnitude of magnetic field of that particular concentration and the magnitude of magnetic field measured with distilled water alone.

While Figure 4.12 doesn't directly correspond to the simulations performed whose results are shown in Figure 4.4, some broader patterns emerge. They are that 1) materials of lower conductivity on the order of 1-10 Sm^{-1} could be detected and characterized using atomic magnetometers like optically pumped magnetometers and 2) the secondary magnetic field strength created through the generated eddy currents within lower conductivity regime is in the order of 0- 60 pT for the present experimental setup and the current strengths used in the experiment, and it can be detected experimentally.

The maximum difference of 60.33 pT is observed for a corresponding electrical conductivity of 2.9 Sm^{-1}. Low conductivity material based (Sub 1 Sm^{-1}) Magnetic Induction Tomography can be accomplished using the high sensitivity of optically pumped magnetometers, accurate magnetic shielding and cancellation fields. The use of Lock In Amplifiers can also help in measuring the phase changes caused due to the presence of low conductivity materials. Better calibration can be accomplished by activating the Helmholtz coil to be able to measure more accurately in the dynamic range, which in turn help in measuring materials of even lower conductivities below 0.2 Sm^{-1}.

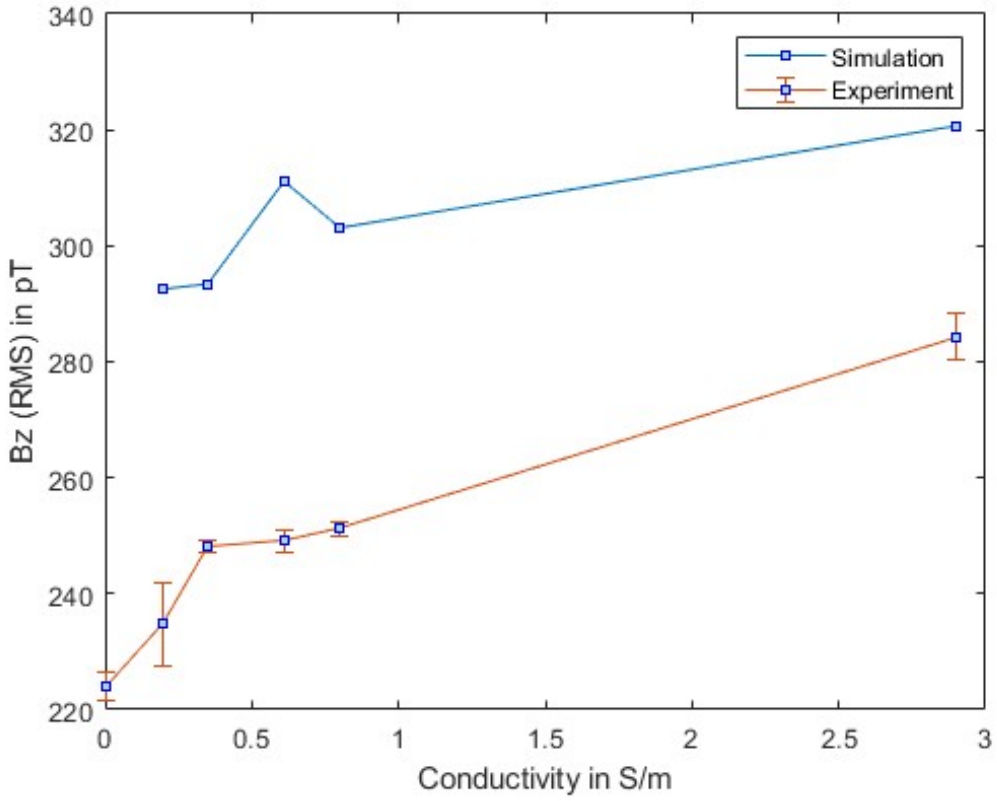

Figure 4.14: Electrical Conductivity in Sm^{-1} vs. Axial Magnetic Field (RMS) in pT (Comparison between COMSOL simulations and experimental results)

Figure 4.14 presents a comparison between numerical simulations performed using COMSOL and experimental results obtained. The COMSOL simulations have a noise floor that is 70 pT higher than the measured experimental results. This can be overcome by better numerical

modeling and finer and targeted meshing. Modeling the skin depth modeling requires better analytical solutions at the lower conductivity regime, especially at 0-1 Sm^{-1} domain. The usual inverse relation used cannot be used to directly model skin depth within these regimes. The feature that occurs within this range is possibly a resultant of such a direct modelling of skin depth. Better skin depth modelling [95], both analytically and numerically, can help avoid discrepancies in measurements and help determine if the secondary magnetic field varies linearly with change in electrical conductivity within the lower ranges.

The experiment could be expanded and probed by recording and measuring the phase variations induced due to the presence of the low conductivity sample (saline solution) using a Lock In Amplifier. The phase measurements could be helpful in characterizing the low conductivity regime better. A square shaped pickup coil is presently used to generate the excitor field. The coil can be modified to adjust the strength and the shape of the excitor field. The PCB coils present within the shielded environment that provide a uniform field could be leveraged to be used as excitor coils, in order to enhance the experiment further.

4.8 Conclusion

It is seen from the experimental results that Magnetic Induction Tomography of low conductivity materials ($0 - 3$ Sm^{-1}) is possible using optically pumped magnetometers. The idea of differential measurement is used to measure the effect of low conductivity materials upon eddy current induced secondary magnetic fields. The work was initially validated using model simulations, was performed experimentally and in future, calculations and simulations of eddy current induced secondary magnetic fields from low conductivity materials with a skin depth across the range of the object dimensions can be performed.

The experimental setup could be improved and made to sense and detect lower magnetic fields and the sensitivity could be improved by enhancing the shielding and the cancellation techniques. Integration of multiple sensors, improvement of the bandwidth of the sensors into RF (Radio Frequency) range and enhancement of excitor coil and cancellation coil techniques could result in moving Magnetic Induction Tomography to the low conductivity regime. Further work could also include the use of the magnetic shield based gradient coils to be used as excitor coils and development of sensitivity matrices that can help in inversion of low conductivity materials, to be able to accomplish Magnetic Induction Tomography within that electrical conductivity regime.

Chapter 5

Challenges and Opportunities in Magnetic Induction Tomography

5.1 Overview

The chapter present a brief overview of the thesis, its contributions to the larger literature of Magnetic Induction Tomography, the gaps in the literature that it bridges, the potential of the work and how it could be improved and made more efficient. It also presents the potential opportunities for Magnetic Induction Tomography and how these could be realized.

5.2 Introduction

This chapter highlights some of the conclusions that are drawn based upon the work done in Chapters 2,3 and 4.

In Chapter 2, the use of spherical harmonic magnetic fields as excitor fields in Magnetic Induction Tomography was established. The sensitivity matrices formulated based upon spherical harmonics were introduced and noted to be invertible, physically realizable and linearly independent. Two algorithms - Linear Backprojection and Linear regression with Tikhonov Regularization were used in order to arrive at the final image reconstruction.

In Chapter 3, the relationship between electrical conductivity and the phase of the secondary magnetic fields in Magnetic Induction Tomography was explored. A phase difference based reconstruction of the region of interest using Radon transforms was developed and demonstrated, applying the same spherical harmonic based fields.

Measurements of the secondary magnetic fields generated due to induced eddy currents from low conductivity materials were presented, using optically pumped magnetometers, in Chapter 4. The optically pumped magnetometer based Magnetic Induction Tomography (OPM-MIT) paves the way for imaging sub 1 Sm^{-1} electrical conductivity with better accuracy and resolution, then hitherto achieved.

5.3 Contributions of the work

The thesis contributes in three ways. The first is establishing the use of spherical harmonic vector fields as excitor fields in Magnetic Induction Tomography. Some of the previous literature

indicates the need for sensitivity matrices describing the system to be built so that they are linearly independent [121]. Previous tomographic reconstruction techniques used a numerical algorithm oriented software based technique. This work explores the early use of a physical hardware based, experimental technique to ensure that the sensitivity matrix is linearly independent. The use of spherical harmonics enables the creation orthogonal magnetic fields and linearly independent and orthogonal sensitivity matrices, making the process of inversion efficient and accurate.

Secondly, the thesis explores the use of Radon transform within the context of Magnetic Induction Tomography. While Radon transform is a commonly used technique in the literature and medical imaging, here it has been applied to a Magnetic Induction Tomography based system for image reconstruction. In comparison between the two methods, developing sensitivity matrices based on orthogonal excitor fields makes the task of inversion efficient and hence reconstruction using the amplitude of the secondary magnetic field is helpful when the region of interest involved is large and it needs to be imaged or characterized quickly. The phase based reconstructions using Radon transforms are much more helpful when operating within the low conductivity regime like insulators and plastics. It is useful when the region of interest is concentrated and a greater resolution is needed in terms of imaging or characterization. Even insulators with electrical conductivities on the order of 0-1 Sm^{-1} produce a small phase change in the order of millidegrees which can be measured using a Lock In Amplifier. The theory of Radon transformations is well developed and the well studied mechanism can help better in the reconstruction as opposed to the still developing theory of orthogonally constructed sensitivity matrices.

Thirdly, the work measures induced, eddy current based, secondary magnetic fields from materials of electrical conductivity in the range of $0 - 1\ Sm^{-1}$ using optically pumped magnetometers. Magnetic Induction Tomography has used coils to measure in that conductivity range before, but only at a very high frequency in the order of $5 - 10\ MHz$. While previous literature has measured induced magnetic fields from low conductivity materials, the lowest measured was 3.8 Sm^{-1} using optically pumped magnetometers. This work has measured materials of conductivity as low as 0.2 Sm^{-1}, using optically pumped magnetometers which work within the frequency range of $0 - 99\ Hz$. In this regime, the skin depth is long enough for the entire sample of interest to be probed. It should be possible to use optically pumped magnetometers to measure fields from materials of even lower conductivity as the bandwidth and the operating frequency range of the optically pumped magnetometers improve and new RF atomic magnetometers are developed.

5.4 Future Work

The work can be enhanced and improved upon in many ways - both experimentally and theoretically.

So far, the work has concentrated on lower order spherical harmonics. Higher order spherical harmonics can be implemented as excitation fields and the secondary magnetic response from the region of interest could be recorded. Excitor coil systems could be created so as to generate higher order spherical harmonic based magnetic fields. This will help improve the quality of image reconstructions and help image conductivity distributions spread across a range of metallic conductors and insulators. It also helps exploit the property of orthogonality to the fullest possible extent and perform through the barrier imaging.

Sensitivity matrices could be formulated in different ways, other than the ones proposed in the literature so far. Modifying the way sensitivity is calculated could yield better formulations of the sensitivity matrix.

This work uses only two algorithms to arrive at final reconstructions, namely Linear Back-projection and Linear Regression with Tikhonov Regularization. More methods and algorithms that could lead to better reconstructions like iterative regularizations, conjugate gradient methods and diffusion problems could potentially be tried out to solve inverse problems as part of Magnetic Induction Tomography to arrive at the final image reconstruction.

The use of optically pumped magnetometers in magnetic sensing within Magnetic Induction Tomography could be further improved by creating higher fidelity spherical harmonics within the passive shield. The excitor coils could be replaced by the inbuilt coils of the magnetic shielding system. A better cancellation system could be introduced and the use of wrapper coils and on board coils within the chip scale magnetometer could be explore further. This could lead the way towards a multichannel optically pumped magnetometer [142] [143] based Magnetic Induction Tomography system (OPM-MIT). The potential use of other quantum sensing platforms could also be explored.

5.5 Challenges and Opportunities in Magnetic Induction Tomography

The field of Magnetic Induction Tomography research presents both challenges and opportunities. Some of the challenges include finding proper current sources that can generate accurately and stably the required spherical harmonic magnetic fields, and exploring the use of higher order harmonics in inversion. Also, ways need to be found to physically implement higher order harmonic excitor coil systems. Work is needed to implement a Magnetic Induction Tomography system by using quantum sensors where the effect of the primary excitor field upon the magnetometer is nulled in the absence of a sample.

Magnetic induction tomography has a lot of potential applications that could be explored. Within Non Destructive Evaluation (NDE), it can be used to measure the amount of moisture within metallic elements that could potentially help in determining the strength of materials and stability of structures. As a defense and security application, it could be used to track the changing nature of a potential threat over a period of time. This would provide a primary screening check, before resorting to more destructive evaluation methods like X- Rays. It also has potential applications in security scanners in airports with its ability to image through barriers.

The non-ionising nature of Magnetic Induction Tomography is a great advantage with immense potential in biomedical imaging applications. It could be used in all platforms where the use of ionising radiation like X-Rays and radiation exposure is prohibited or limited, like imaging infants. It doesn't require cryogenic systems and coolants like liquid helium. Hence, it could prove to be an economic and cost effective solution to barriers to accessing medical diagnostic technologies in many parts of the world.

5.6 Conclusion

The idea of Magnetic Induction Tomography was introduced and advanced in the thesis. Its history, conceptualization, experimental methods and applications were studied. The required theoretical and experimental frameworks were drawn from previously existing literature.

The idea of using spherical harmonic magnetic vector fields in Magnetic Induction Tomography was demonstrated with effective final image reconstructions obtained in the work. The work further explored the effects on the phase of the secondary magnetic fields induced by eddy currents within the region of interest. Finally, the work demonstrated how quantum sensors like optically pumped magnetometers can be utilized to measure ultra low magnetic fields induced within Magnetic Induction Tomography of ultra low conductivity systems.

Bibliography

[1] H Griffiths. "Magnetic induction tomography". In: *Measurement science and technology* 12.8 (2001), p. 1126.

[2] S Al-Zeibak and NH Saunders. "A feasibility study of in vivo electromagnetic imaging". In: *Physics in Medicine & Biology* 38.1 (1993), p. 151.

[3] A Korjenevsky, V Cherepenin, and S Sapetsky. "Magnetic induction tomography: experimental realization". In: *Physiological measurement* 21.1 (2000), p. 89.

[4] H Griffiths, WR Stewart, and W Gough. "Magnetic induction tomography: a measuring system for biological tissues". In: *Annals of the New York Academy of Sciences* 873.1 (1999), pp. 335–345.

[5] Slawomir Tumanski. "Induction coil sensors—A review". In: *Measurement Science and Technology* 18.3 (2007), R31.

[6] Hermann Scharfetter, Helmut K Lackner, and Javier Rosell. "Magnetic induction tomography: hardware for multi-frequencymeasurements in biological tissues". In: *Physiological Measurement* 22.1 (2001), p. 131.

[7] Lu Ma and Manuchehr Soleimani. "Magnetic induction spectroscopy for permeability imaging". In: *Scientific Reports* 8.1 (2018), p. 7025.

[8] Gavin Dingley and Manuchehr Soleimani. "Multi-frequency magnetic induction tomography system and algorithm for imaging metallic objects". In: *Sensors* 21.11 (2021), p. 3671.

[9] Zulkarnay Zakaria et al. "Initial results on magnetic induction tomography hardware measurement using hall effect sensor application". In: *2010 IEEE EMBS Conference on Biomedical Engineering and Sciences (IECBES)*. IEEE. 2010, pp. 9–12.

[10] Doga Gursoy and Hermann Scharfetter. "Optimum receiver array design for magnetic induction tomography". In: *IEEE transactions on biomedical engineering* 56.5 (2009), pp. 1435–1441.

[11] Fang Li, Manuchehr Soleimani, and J Abascal. "Planar array magnetic induction tomography further improvement". In: *Sensor Review* 39.2 (2019), pp. 257–268.

[12] Yang Xuan et al. "A FEM method for magnetic induction tomography forward problem". In: *2013 IEEE International Conference on Medical Imaging Physics and Engineering*. IEEE. 2013, pp. 219–222.

[13] A Morris, H Griffiths, and W Gough. "A numerical model for magnetic induction tomographic measurements inbiological tissues". In: *Physiological measurement* 22.1 (2001), p. 113.

[14] Jiyun Jeon, Wonmo Chung, and Hungsun Son. "Magnetic induction tomography using magnetic dipole and lumped parameter model". In: *IEEE Access* 7 (2019), pp. 70287–70295.

[15] Gianpaolo Piscitelli et al. “Magnetic induction tomography via the monotonicity principle”. In: *Journal of Physics: Conference Series*. Vol. 2444. 1. IOP Publishing. 2023, p. 012005.

[16] Chan Sam Park et al. “A portable phase-domain magnetic induction tomography transceiver with phase-band auto-tracking and frequency-sweep capabilities”. In: *Sensors* 18.11 (2018), p. 3816.

[17] Tatiana Schledewitz, Martin Klein, and Dirk Rueter. “Magnetic induction tomography: Separation of the ill-posed and non-linear inverse problem into a series of isolated and less demanding subproblems”. In: *Sensors* 23.3 (2023), p. 1059.

[18] Hermann Scharfetter et al. “Single-step 3-D image reconstruction in magnetic induction tomography: Theoretical limits of spatial resolution and contrast to noise ratio”. In: *Annals of biomedical engineering* 34 (2006), pp. 1786–1798.

[19] Guoqiang Liu, Tao Wang, and Meng Meng. “Edge Element Method for Magnetic Induction Tomography”. In: *2005 IEEE Engineering in Medicine and Biology 27th Annual Conference*. IEEE. 2006, pp. 1516–1517.

[20] Ryokei Yoshimura and Naoto Oshiman. “Edge-based finite element approach to the simulation of geoelectromagnetic induction in a 3-D sphere”. In: *Geophysical Research Letters* 29.3 (2002), pp. 9–1.

[21] Hsin-Yu Wei, Lu Ma, and Manuchehr Soleimani. “Volumetric magnetic induction tomography”. In: *Measurement Science and Technology* 23.5 (2012), p. 055401.

[22] Arne Wickenbrock et al. “Magnetic induction tomography using an all-optical 87Rb atomic magnetometer”. In: *Optics letters* 39.22 (2014), pp. 6367–6370.

[23] Cameron Deans, Luca Marmugi, and Ferruccio Renzoni. “Electromagnetic induction imaging with atomic magnetometers”. In: *Imaging Systems and Applications*. Optica Publishing Group. 2017, ITu3E–5.

[24] Kasper Jensen et al. “Magnetocardiography on an isolated animal heart with a room-temperature optically pumped magnetometer”. In: *Scientific reports* 8.1 (2018), p. 16218.

[25] Patrick Bevington, Rafal Gartman, and Witold Chalupczak. “Magnetic induction tomography of structural defects with alkali–metal spin maser”. In: *Applied optics* 59.8 (2020), pp. 2276–2282.

[26] Cameron Deans, Luca Marmugi, and Ferruccio Renzoni. “Through-barrier electromagnetic imaging with an atomic magnetometer”. In: *Optics Express* 25.15 (2017), pp. 17911–17917.

[27] Lucas M Rushton et al. “Unshielded portable optically pumped magnetometer for the remote detection of conductive objects using eddy current measurements”. In: *Review of Scientific Instruments* 93.12 (2022).

[28] Wenqiang Zheng et al. “Entanglement-enhanced magnetic induction tomography”. In: *Physical Review Letters* 130.20 (2023), p. 203602.

[29] Lian Zhou et al. “Magnetoacoustic tomography with magnetic induction (MAT-MI) for breast tumor imaging: numerical modeling and simulation”. In: *Physics in Medicine & Biology* 56.7 (2011), p. 1967.

[30] Zhili Xiao, Chao Tan, and Feng Dong. “Multi-frequency difference method for intracranial hemorrhage detection by magnetic induction tomography”. In: *Physiological measurement* 39.5 (2018), p. 055006.

[31] Yinan Chen et al. “Imaging hemorrhagic stroke with magnetic induction tomography: realistic simulation and evaluation”. In: *Physiological measurement* 31.6 (2010), p. 809.

[32] M Zolgharni et al. “Imaging cerebral haemorrhage with magnetic induction tomography: numerical modelling”. In: *Physiological measurement* 30.6 (2009), S187.

[33] Yang Jiao et al. “Real-time imaging of traumatic brain injury using magnetic induction tomography”. In: *Physiological Measurement* 44.3 (2023), p. 035012.

[34] Luca Marmugi and Ferruccio Renzoni. “Optical magnetic induction tomography of the heart”. In: *Scientific reports* 6.1 (2016), p. 23962.

[35] Doga Gürsoy and Hermann Scharfetter. “Feasibility of lung imaging using magnetic induction tomography”. In: *World Congress on Medical Physics and Biomedical Engineering, September 7-12, 2009, Munich, Germany: Vol. 25/2 Diagnostic Imaging*. Springer. 2009, pp. 525–528.

[36] Lulu Wang and Ahmed M Al-Jumaily. “Imaging of lung structure using holographic electromagnetic induction”. In: *IEEE Access* 5 (2017), pp. 20313–20318.

[37] Lu Ma. “Magnetic induction tomography for non-destructive evaluation and process tomography”. PhD thesis. University of Bath, 2014.

[38] Hsin-Yu Wei and Manuchehr Soleimani. “A magnetic induction tomography system for prospective industrial processing applications”. In: *Chinese Journal of Chemical Engineering* 20.2 (2012), pp. 406–410.

[39] Fang Li et al. “Monitoring surface defects deformations and displacements in hot steel using magnetic induction tomography”. In: *Sensors* 19.13 (2019), p. 3005.

[40] Oliver Dorn and Alex Hiles. “A level set method for magnetic induction tomography of 3D boxes and containers”. In: *Electromagnetic Non-Destructive Evaluation (XXI)*. IOS press, 2018, pp. 33–40.

[41] Anders Vest Christiansen et al. “Improved geoarchaeological mapping with electromagnetic induction instruments from dedicated processing and inversion”. In: *Remote Sensing* 8.12 (2016), p. 1022.

[42] Lu Ma, Andy Hunt, and Manuchehr Soleimani. “Experimental evaluation of conductive flow imaging using magnetic induction tomography”. In: *International Journal of Multiphase Flow* 72 (2015), pp. 198–209.

[43] Max Sieger et al. “Two-field excitation for contactless inductive flow tomography”. In: *Sensors* 24.14 (2024), p. 4458.

[44] Michael D O’Toole et al. “Non-contact multi-frequency magnetic induction spectroscopy system for industrial-scale bio-impedance measurement”. In: *Measurement Science and Technology* 26.3 (2015), p. 035102.

[45] Jiawei Tang, Wuliang Yin, and Mingyang Lu. “Bio-impedance spectroscopy for frozen-thaw of bio-samples: Non-contact inductive measurement and finite element (FE) based cell modelling”. In: *Journal of Food Engineering* 272 (2020), p. 109784.

[46] Anup Barai et al. “Magnetic induction spectroscopy: non-contact measurement of the electrical conductivity spectra of biological samples”. In: *Measurement Science and Technology* 23.8 (2012), p. 085501.

[47] Natalia Ortiz Gómez and Scott JI Walker. “Eddy currents applied to de-tumbling of space debris: Analysis and validation of approximate proposed methods”. In: *Acta Astronautica* 114 (2015), pp. 34–53.

[48] Kush K Sharma et al. “Space debris reduction using eddy currents”. In: *2018 Atmospheric Flight Mechanics Conference*. 2018, p. 3161.

[49] Laurent Baratchart et al. “Unique reconstruction of simple magnetizations from their magnetic potential”. In: *Inverse Problems* 37.10 (2021), p. 105006.

[50] Maureen Clerc et al. “Inverse conductivity recovery problem in a spherical geometry from EEG data: uniqueness, reconstruction and stability results”. In: *TAMTAM 2017-8ème colloque, Tendances dans les Applications Mathématiques en Tunisie Algérie Maroc*. 2017, p. 1.

[51] Masaru Kono, Hidefumi Tanaka, and Hideo Tsunakawa. “Spherical harmonic analysis of paleomagnetic data: the case of linear mapping”. In: *Journal of Geophysical Research: Solid Earth* 105.B3 (2000), pp. 5817–5833.

[52] Malcolm G McLeod. “Orthogonality of spherical harmonic coefficients”. In: *Physics of the Earth and Planetary Interiors* 23.2 (1980), P1–P4.

[53] FJ Lowes and DE Winch. “Orthogonality of harmonic potentials and fields in spheroidal and ellipsoidal coordinates: application to geomagnetism and geodesy”. In: *Geophysical Journal International* 191.2 (2012), pp. 491–507.

[54] Maciej Długosz and Joanna Trylska. “Electrostatic similarity of proteins: Application of three dimensional spherical harmonic decomposition”. In: *The Journal of chemical physics* 129.1 (2008).

[55] Jussi Rahola, Fabio Belloni, and Andreas Richter. “Modelling of radiation patterns using scalar spherical harmonics with vector coefficients”. In: *2009 3rd European Conference on Antennas and Propagation*. IEEE. 2009, pp. 3361–3365.

[56] KA Whaler and D Gubbins. “Spherical harmonic analysis of the geomagnetic field: an example of a linear inverse problem”. In: *Geophysical Journal International* 65.3 (1981), pp. 645–693.

[57] JB Muir and Hrvoje Tkalčić. “A method of spherical harmonic analysis in the geosciences via hierarchical Bayesian inference”. In: *Geophysical Journal International* 203.2 (2015), pp. 1164–1171.

[58] Françoise Roméo and DI Hoult. “Magnet field profiling: analysis and correcting coil design”. In: *Magnetic resonance in medicine* 1.1 (1984), pp. 44–65.

[59] Joonas Iivanainen et al. “Calibration and localization of optically pumped magnetometers using electromagnetic coils”. In: *Sensors* 22.8 (2022), p. 3059.

[60] Simon Eck et al. “A spherical harmonics intensity model for 3D segmentation and 3D shape analysis of heterochromatin foci”. In: *Medical image analysis* 32 (2016), pp. 18–31.

[61] Li Shen, Hany Farid, and Mark A McPeek. “Modeling three-dimensional morphological structures using spherical harmonics”. In: *Evolution* 63.4 (2009), pp. 1003–1016.

[62] Helmut Schaeben and K Gerald van den Boogaart. “Spherical harmonics in texture analysis”. In: *Tectonophysics* 370.1-4 (2003), pp. 253–268.

[63] Caitlin R Nortje et al. “Spherical harmonics for surface parametrisation and remeshing”. In: *Mathematical Problems in Engineering* 2015.1 (2015), p. 582870.

[64] Anne Gelb. “The resolution of the Gibbs phenomenon for spherical harmonics”. In: *Mathematics of Computation* 66.218 (1997), pp. 699–717.

[65] Thomas Annen et al. “Spherical harmonic Gradients for Mid-Range Illumination.” In: *Rendering Techniques*. 2004, pp. 331–336.

[66] Ralf Habel, Bogdan Mustata, and Michael Wimmer. "Efficient spherical harmonics lighting with the preetham skylight model." In: *Eurographics (short papers)*. 2008, pp. 119–122.

[67] Olivier Génevaux, Frédéric Larue, and Jean-Michel Dischler. "Interactive refraction on complex static geometry using spherical harmonics". In: *Proceedings of the 2006 symposium on Interactive 3D graphics and games*. 2006, pp. 145–152.

[68] Jan Kautz, John Snyder, and Peter-Pike J Sloan. "Fast arbitrary brdf shading for low-frequency lighting using spherical harmonics." In: *Rendering Techniques* 2.291-296 (2002), p. 1.

[69] Kathryn P Drake and Grady B Wright. "A fast and accurate algorithm for spherical harmonic analysis on HEALPix grids with applications to the cosmic microwave background radiation". In: *Journal of Computational Physics* 416 (2020), p. 109544.

[70] N Rambaux et al. "Spherical harmonic decomposition and interpretation of the shapes of the small Saturnian inner moons". In: *Astronomy & Astrophysics* 667 (2022), A78.

[71] Richard J Morris et al. "Real spherical harmonic expansion coefficients as 3D shape descriptors for protein binding pocket and ligand comparisons". In: *Bioinformatics* 21.10 (2005), pp. 2347–2355.

[72] Didier Pinchon and Philip E Hoggan. "Rotation matrices for real spherical harmonics: general rotations of atomic orbitals in space-fixed axes". In: *Journal of Physics A: Mathematical and Theoretical* 40.7 (2007), p. 1597.

[73] Javier Rosell, Roberto Casanas, and Hermann Scharfetter. "Sensitivity maps and system requirements for magnetic inductiontomography using a planar gradiometer". In: *Physiological measurement* 22.1 (2001), p. 121.

[74] WRB Lionheart, Manuchehr Soleimani, and AJ Peyton. "Sensitivity analysis in 3D magnetic induction tomography (MIT)". In: *Proc. 3rd World Congr. Industrial Process Tomography*. Citeseer. 2003, pp. 239–244.

[75] Jinxi Xiang et al. "Design of a magnetic induction tomography system by gradiometer coils for conductive fluid imaging". In: *IEEE Access* 7 (2019), pp. 56733–56744.

[76] Tianrui Chen and Jingbo Guo. "A computationally efficient method for sensitivity matrix calculation in magnetic induction tomography". In: *Journal of Physics: Conference Series*. Vol. 1074. 1. IOP Publishing. 2018, p. 012106.

[77] Manuchehr Soleimani and Karen Jersey-Willuhn. "Sensitivity analysis for magnetic induction tomography". In: *The 26th Annual International Conference of the IEEE Engineering in Medicine and Biology Society*. Vol. 1. IEEE. 2004, pp. 1368–1371.

[78] PR McGillivray et al. "Calculation of sensitivities for the frequency-domain electromagnetic problem". In: *Geophysical Journal International* 116.1 (1994), pp. 1–4.

[79] DN Dyck, DA Lowther, and EM Freeman. "Design of electromagnetic devices using sensitivities computed with the adjoint variable method". In: *1994 Second International Conference on Computation in Electromagnetics*. IET. 1994, pp. 231–234.

[80] Karl Hollaus et al. "Fast calculation of the sensitivity matrix in magnetic induction tomography by tetrahedral edge finite elements and the reciprocity theorem". In: *Physiological measurement* 25.1 (2004), p. 159.

[81] Wuliang Yin and Anthony J Peyton. "Sensitivity formulation including velocity effects for electromagnetic induction systems". In: *IEEE Transactions on Magnetics* 46.5 (2009), pp. 1172–1176.

[82] Charles W Groetsch and CW Groetsch. *Inverse problems in the mathematical sciences*. Vol. 52. Springer, 1993.

[83] K Cao. "Inverse Problems for the Heat Equation Using Conjugate Gradient Methods". PhD thesis. University of Leeds, 2018.

[84] Shima Kamyab et al. "Deep learning methods for inverse problems". In: *PeerJ Computer Science* 8 (2022), e951.

[85] Alexis Goujon et al. "A neural-network-based convex regularizer for inverse problems". In: *IEEE Transactions on Computational Imaging* 9 (2023), pp. 781–795.

[86] Gastao Cruz et al. "MRI Reconstruction as an Inverse Problem". In: *Advances in Magnetic Resonance Technology and Applications*. Vol. 7. Elsevier, 2022, pp. 37–57.

[87] Roel Snieder. "Inverse problems in geophysics". In: *Signal recovery and synthesis*. Optica Publishing Group. 2001, SMA2.

[88] Peyman Milanfar and Mauricio Delbracio. "Denoising: A powerful building-block for imaging, inverse problems, and machine learning". In: *arXiv preprint arXiv:2409.06219* (2024).

[89] Adrien EE Dubois et al. "Untrained physically informed neural network for image reconstruction of magnetic field sources". In: *Physical review applied* 18.6 (2022), p. 064076.

[90] Monika Bahl and P Senthilkumaran. "Helmholtz Hodge decomposition of scalar optical fields". In: *Journal of the Optical Society of America A* 29.11 (2012), pp. 2421–2427.

[91] Christian L Degen, Friedemann Reinhard, and Paola Cappellaro. "Quantum sensing". In: *Reviews of modern physics* 89.3 (2017), p. 035002.

[92] Tim M Tierney et al. "Optically pumped magnetometers: From quantum origins to multi-channel magnetoencephalography". In: *NeuroImage* 199 (2019), pp. 598–608.

[93] Ben Stray et al. "Quantum sensing for gravity cartography". In: *Nature* 602.7898 (2022), pp. 590–594.

[94] George B Arfken and Hans J Weber. "Mathematical methods for physicists 6th ed." In: *Mathematical methods for physicists 6th ed. by George B. Arfken and Hans J. Weber. Published: Amsterdam; Boston: Elsevier* (2005).

[95] Logan Turton. "Improved Magnetic Induction Tomography". PhD thesis. University of Nottingham, 2022.

[96] James R Nagel. "Induced eddy currents in simple conductive geometries: mathematical formalism describes the excitation of electrical eddy currents in a time-varying magnetic field". In: *IEEE Antennas and Propagation Magazine* 60.1 (2017), pp. 81–88.

[97] CP Bidinosti, EM Chapple, and ME Hayden. "The sphere in a uniform RF field—Revisited". In: *Concepts in Magnetic Resonance Part B: Magnetic Resonance Engineering: An Educational Journal* 31.3 (2007), pp. 191–202.

[98] Lu Ma, Stefano Spagnul, and Manuchehr Soleimani. "Metal solidification imaging process by magnetic induction tomography". In: *Scientific reports* 7.1 (2017), p. 14502.

[99] COMSOL. *AC/DC Module*. URL: `https://www.comsol.com/acdc-module`.

[100] Amir Ahmad Roohi Noozadi. *Forward and Inverse Modelling of Magnetic Induction Tomography (MIT) for Biomedical Application*. Ecole Polytechnique, Montreal (Canada), 2017.

[101] Giulio Giovannetti. "Comparison between circular and square loops for low-frequency magnetic resonance applications: theoretical performance estimation". In: *Concepts in Magnetic Resonance Part B: Magnetic Resonance Engineering* 46.3 (2016), pp. 146–155.

[102] All about Circuits. *Rectangle Loop Inductance Calculator*. URL: https://www.allaboutcircuits.com/tools/rectangle-loop-inductance-calculator/.

[103] Lakeshore. *F71 and F41 Teslameter technical specifications*. URL: https://www.lakeshore.com/products/categories/overview/magnetic-products/gaussmeters-teslameters/f71-and-f41-teslameters.

[104] National Instruments. *Data Acquisition*. URL: https://www.ni.com/en/shop/data-acquisition.html.

[105] Thorlabs. *Motion Control*. URL: https://www.thorlabs.com/navigation.cfm?guideid=2081.

[106] Fatemeh Ghasemifard, M Johansson, and Martin Norgren. "Current reconstruction from magnetic field using spherical harmonic expansion to reduce impact of disturbance fields". In: *Inverse Problems in Science and Engineering* 25.6 (2017), pp. 795–809.

[107] Bo Wang et al. "Back-projection algorithm in generalized form for circular-scanning-based photoacoustic tomography with improved tangential resolution". In: *Quantitative imaging in medicine and surgery* 9.3 (2019), p. 491.

[108] Benyuan Sun et al. "A new linear back projection algorithm to electrical tomography based on measuring data decomposition". In: *Measurement Science and Technology* 26.12 (2015), p. 125402.

[109] Mingquan Wang et al. "Electrical impedance tomography based on Tikhonov regularization method improved by level set method". In: *2010 3rd International Conference on Biomedical Engineering and Informatics*. Vol. 1. IEEE. 2010, pp. 222–225.

[110] Ronald W Schafer. "What is a savitzky-golay filter?[lecture notes]". In: *IEEE Signal processing magazine* 28.4 (2011), pp. 111–117.

[111] Harrison H Barrett. "Iii the radon transform and its applications". In: *Progress in optics*. Vol. 21. Elsevier, 1984, pp. 217–286.

[112] Sigurdur Helgason and Sigurdur Helgason. "The radon transform on r n". In: *Integral Geometry and Radon Transforms* (2011), pp. 1–62.

[113] IV Anikin and L Szymanowski. "Inverse Radon transform and the transverse-momentum dependent functions". In: *Physical Review D* 100.9 (2019), p. 094034.

[114] M Buchner et al. "Tutorial: Basic principles, limits of detection, and pitfalls of highly sensitive SQUID magnetometry for nanomagnetism and spintronics". In: *Journal of Applied Physics* 124.16 (2018).

[115] Yuantian Lu et al. "Recent progress of atomic magnetometers for geomagnetic applications". In: *Sensors* 23.11 (2023), p. 5318.

[116] Kai-Mei C Fu et al. "Sensitive magnetometry in challenging environments". In: *AVS Quantum Science* 2.4 (2020).

[117] Kosuke Takada, Ryota Katsumi, and Takashi Yatsui. "Sensitivity improvement of a single-NV diamond magnetometer using a chiral waveguide". In: *Optics Express* 32.1 (2023), pp. 795–802.

[118] T Dyer, PF Griffin, and E Riis. "Single-board low-noise fluxgate magnetometer". In: *Journal of Applied Physics* 135.3 (2024).

[119] Khalil R Rostami and Ivan P Nikitin. "High-sensitivity two-stage Hall magnetometer with enhanced linearity and spatial resolution". In: *Measurement* 153 (2020), p. 107423.

[120] Zheng You. *Space microsystems and micro/nano satellites*. Butterworth-Heinemann, 2017.

[121] Xu Li, Kai Yu, and Bin He. "Magnetoacoustic tomography with magnetic induction (MAT-MI) for imaging electrical conductivity of biological tissue: a tutorial review". In: *Physics in Medicine & Biology* 61.18 (2016), R249.

[122] Peter DD Schwindt et al. "Chip-scale atomic magnetometer". In: *Applied Physics Letters* 85.26 (2004), pp. 6409–6411.

[123] John Kitching. "Chip-scale atomic devices". In: *APS Division of Atomic, Molecular and Optical Physics Meeting Abstracts*. Vol. 37. 2006, T1–004.

[124] Huiyao Yu et al. "Key Technologies in Developing Chip-Scale Hot Atomic Devices for Precision Quantum Metrology". In: *Micromachines* 15.9 (2024), p. 1095.

[125] Gabriela D Martinez et al. "A chip-scale atomic beam clock". In: *Nature Communications* 14.1 (2023), p. 3501.

[126] John Kitching. "Chip-scale atomic devices". In: *Applied Physics Reviews* 5.3 (2018).

[127] Matthew J Brookes et al. "Magnetoencephalography with optically pumped magnetometers (OPM-MEG): the next generation of functional neuroimaging". In: *Trends in Neurosciences* 45.8 (2022), pp. 621–634.

[128] Nibedita Ram, M Pattabiraman, and C Vijayan. "Low field Zeeman magnetometry using rubidium absorption spectroscopy". In: *Journal of Physics: Conference Series*. Vol. 80. 1. IOP Publishing. 2007, p. 012035.

[129] IM Savukov and MV Romalis. "Effects of spin-exchange collisions in a high-density alkali-metal vapor in low magnetic fields". In: *Physical Review A—Atomic, Molecular, and Optical Physics* 71.2 (2005), p. 023405.

[130] Yintao Ma et al. "Ultrasensitive SERF atomic magnetometer with a miniaturized hybrid vapor cell". In: *Microsystems & Nanoengineering* 10.1 (2024), p. 121.

[131] Blake Andrews et al. "High-sensitivity multichannel zero-to-ultralow field NMR with atomic magnetometer arrays". In: *arXiv preprint arXiv:2407.00929* (2024).

[132] P-H Chu et al. "Sensitivity of proposed search for axion-induced magnetic field using optically pumped magnetometers". In: *Physical Review D* 97.7 (2018), p. 072011.

[133] Kasper Jensen et al. "Detection of low-conductivity objects using eddy current measurements with an optical magnetometer". In: *Physical Review Research* 1.3 (2019), p. 033087.

[134] Anna F Rusydi. "Correlation between conductivity and total dissolved solid in various type of water: A review". In: *IOP conference series: earth and environmental science*. Vol. 118. IOP publishing. 2018, p. 012019.

[135] Masaki Hayashi. "Temperature-electrical conductivity relation of water for environmental monitoring and geophysical data inversion". In: *Environmental monitoring and assessment* 96 (2004), pp. 119–128.

[136] Peter J Hobson et al. "Benchtop magnetic shielding for benchmarking atomic magnetometers". In: *IEEE Transactions on Instrumentation and Measurement* 72 (2023), pp. 1–9.

[137] Magnetic Shields Limited. *MuMetal Shields*. URL: `https://www.magneticshields.co.uk/product-mumetal-shields`.

[138] QuSpin Inc. *QZFM Gen-2*. URL: `https://quspin.com/products-qzfm/`.

[139] Vladislav Gerginov, Marco Pomponio, and Svenja Knappe. "Scalar magnetometry below 100 fT/Hz 1/2 in a microfabricated cell". In: *IEEE sensors journal* 20.21 (2020), pp. 12684–12690.

[140] Jonathan E Dhombridge et al. “High-sensitivity rf detection using an optically pumped comagnetometer based on natural-abundance rubidium with active ambient-field cancellation”. In: *Physical Review Applied* 18.4 (2022), p. 044052.

[141] Xiyu Liu et al. “Magnetic field imaging with radio-frequency optically pumped magnetometers”. In: *Chinese Optics Letters* 22.6 (2024), p. 060006.

[142] Harry Cook et al. “An optically pumped magnetic gradiometer for the detection of human biomagnetism”. In: *Quantum Science and Technology* 9.3 (2024), p. 035016.

[143] Ryan M Hill et al. “Multi-channel whole-head OPM-MEG: Helmet design and a comparison with a conventional system”. In: *NeuroImage* 219 (2020), p. 116995.